

Ductile Fracture Modeling - Theory, Experimental Investigation and Numerical Verification

by

Liang Xue

B.S. Mechanical Engineering, Shanghai Jiao Tong University, 1994
B.S. Computer Sciences, Shanghai Jiao Tong University, 1994
M.S. Mechanical Engineering, Shanghai Jiao Tong University, 1997
M.S. Ocean Engineering, Massachusetts Institute of Technology, 2003

Submitted to the Department of Mechanical Engineering
in partial fulfillment of the requirements for the degree of

Doctor of Philosophy in Mechanical Engineering

at the

MASSACHUSETTS INSTITUTE OF TECHNOLOGY

June 2007

© Massachusetts Institute of Technology 2007. All rights reserved.

Author

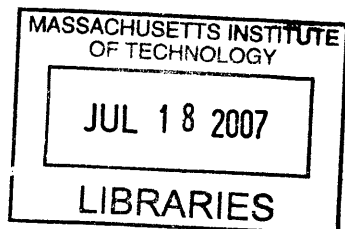
Department of Mechanical Engineering
June 1, 2007

Certified by

Tomasz Wierzbicki
Professor, Applied Mechanics
Thesis Supervisor

Accepted by

Lallit Anand
Chairman, Department Committee on Graduate Students



BARKER

Ductile Fracture Modeling - Theory, Experimental Investigation and Numerical Verification

by

Liang Xue

Submitted to the Department of Mechanical Engineering on February 15, 2007, in partial fulfillment of the requirements for the degree of Doctor of Philosophy in Mechanical Engineering

ABSTRACT

The fracture initiation in ductile materials is governed by the damaging process along the plastic loading path. A new damage plasticity model for ductile fracture is proposed. Experimental results show that fracture initiation in uncracked ductile solids is sensitive to the hydrostatic pressure and is dependent on the Lode angle. The damage plasticity model is established on a “cylindrical decomposition” system accounting for the pressure dependence, Lode angle dependence and the non-linear damage rule. Two internal variables are adopted to quantify the evolution of material properties. One is the plastic strain and the other is so-called damage variable. The joint effects of pressure and Lode angle define a fracture envelope in the principal stress space. Plastic deformation induced damage is expressed by an integral of the damage rate measured at current loading and deformation status with respect to the fracture envelope. A non-linear damage rule is proposed to characterize the damage accumulation with respect to the plastic strain. Furthermore, a damage related weakening factor is adopted to describe the material deterioration. Aluminum alloy 2024-T351 is selected and a series of experiments have been conducted to determine the necessary material parameters for the description of the mechanical and damage properties. The numerical integration procedure is presented. The proposed model is numerically implemented into an explicit code. Simulations were performed and the results show good agreement with the experimental data. Several representative load conditions are also modeled. These simulations illustrate realistic crack patterns. In addition to the damage plasticity model, the micro void shearing mechanism is also introduced into a Gurson-like material model. Improved simulation results are shown.

Keywords: Ductile fracture, Hydrostatic pressure, Lode dependence, Damage plasticity model.

Thesis Supervisor: Tomasz Wierzbicki

Title: Professor of Applied Mechanics

Thesis committee:

Tomasz Wierzbicki, MIT, Professor of Applied Mechanics

David M. Parks, MIT, Professor of Mechanical Engineering

Lallit Anand, MIT, Professor of Mechanical Engineering

John W. Hutchinson, Harvard University, Abbott and James Lawrence Professor of Engineering

Acknowledgments

I wish to express my sincere gratitude to my supervisor Professor Tomasz Wierzbicki for exposing me to fracture mechanics, for his advice, encouragement and patience in my navigation through various aspects of ductile fracture. I would like to thank Professor David M. Parks, Professor Lallit Anand and Professor John W. Hutchinson of Harvard University for their continuous and consistent guidance and insightful comments all the way along my research and the completion of thesis. Thanks are due to Professor Frank A. McClintock, Professor Jacques Besson at Ecole des Mines, France, Professor Thomas Pardoen, Université catholique de Louvain, Belgium, and Professor Jonas Faleskog, Royal Institute of Technology, Sweden, for their helpful discussion.

Assistance in the testing program of my colleagues in the lab: Steve Rudolph, Yuanli Bai, Carey Walters and Pierce Hayward are greatly appreciated. I am thankful to my former and present team members of the Impact and Crashworthiness Lab: Yingbin Bao, Dirk Mohr, Xiaoqing Teng, Young-Woong Lee, Li Zheng, Yuanli Bai, Carey Walters, Jongmin Shim, Min Huang and Allison Beese for making my stay at MIT a memorable one. Special thanks are due to Ms. Sheila McNary for taking care of many administrative details.

I am grateful to my aunt Jie Zheng and uncle Zhaolin Wang for having taken care of me over the years.

This dissertation is dedicated to my parents for their endless love, understanding and support.

Contents

1	Introduction	1
1.1	Background and motivations	1
1.2	Research objectives	2
1.3	Scope of research	4
1.4	Outline of the thesis	5
2	A Brief Review of Existing Damage and Fracture Criteria	7
2.1	Principal stress space	7
2.2	A historical note on fracture	10
2.3	Damage plasticity	13
2.4	Damage modeling approaches	15
2.4.1	Conventional continuum mechanics models	18
2.4.2	Micro mechanical models	22
2.4.3	Continuum damage mechanics	26
2.5	Comparison of damage variables and fracture criteria	27
3	A New Damage Plasticity Model	31
3.1	Methodology and hypothesis	31
3.2	Mathematical aspects	32
3.2.1	Damage accumulation	32
3.2.2	Normalization	33
3.2.3	Separation of p and θ	34
3.3	A geometrical representation of damage accumulation	35

3.3.1	History effect	36
3.4	Yield function and flow rule	37
4	Damage Rule and Material Weakening	39
4.1	On damage variables	39
4.1.1	Damage accumulation	40
4.2	Bridgman's test	41
4.3	Material weakening	44
5	Hydrostatic pressure sensitivity	49
5.1	Survey of previous experimental works	49
5.1.1	Flow and fracture	50
5.1.2	Uniaxial tension under pressure	50
5.1.3	Unidirectional tension of notched round bar	51
5.1.4	Compression under pressure	51
5.1.5	Shear under pressure	52
5.1.6	Bending under pressure	52
5.2	Hydrostatic pressure effect	52
5.2.1	Bridgman's work	52
5.2.2	Pressure dependence	53
5.2.3	Limiting pressure	58
6	Lode Angle Dependence of Ductile Fracture	61
6.1	Lode angle dependence	61
6.2	Experimental results relevant to Lode angle dependence	62
6.2.1	Comparison of simple tension and torsion/shear experiments	62
6.2.2	Comparison of simple tension and transverse plane strain tension	63
6.3	Lode angle dependence function	65
6.3.1	Wilkins, <i>et al</i>	66
6.3.2	Polygon model - the first kind of Lode dependence function	67
6.3.3	Curvilinear model - the second kind of Lode dependence function	69
6.3.4	Combination of pressure and Lode effect	69

6.4	Hardening effect on the Lode angle dependence	71
6.4.1	Experimental results	72
6.4.2	Stören and Rice's bifurcation condition	74
7	Summary on Damage Plasticity Model and Plane Stress Condition	79
7.1	Summary on damage plasticity model	79
7.2	Fracture under plane stress condition	82
8	Elasto-Plastic Constitutive Equations and Numerical Aspects	89
8.1	Damage plasticity theory	89
8.1.1	Kinematics	89
8.1.2	Power	90
8.1.3	Constitutive equations	90
8.2	Time integration procedure	94
8.2.1	Elastic update	95
8.2.2	Elastic-plastic update	95
8.2.3	Summary of integration procedure	99
9	Experimental Program	101
9.1	Pressure dependence calibration	103
9.1.1	Un-notched and notched round bar tensile tests	103
9.1.2	Cylinder compression tests	105
9.1.3	Discussion on anisotropy	113
9.2	Plane strain test	115
10	Determination of the Fracture Envelope	119
10.1	Determination of the stress-strain curve	120
10.2	Determining the weakening function	123
10.3	Determination of the fracture envelope	125
11	Prediction with Damage Plasticity Model	137
11.1	Notched round bars	137
11.1.1	Notch radius 18mm	138

11.1.2	Notch radius 4.5mm	139
11.2	Upsetting tests	140
11.2.1	Crack initiation and propagation in compressed cylinders	140
11.2.2	Friction effect	141
11.2.3	Effect of length of cylinder	144
11.3	Three point bending of a rectangular bar	145
11.3.1	Wide rectangular bar	146
11.3.2	Narrow rectangular beam (three-dimensional)	150
11.4	Compact tension test	152
11.4.1	Slant/flat crack and mode transition	153
11.4.2	Mahmoud and Lease's experiment	160
11.5	Cup-cone fracture of a round bar	166
11.6	Doubly grooved flat plate (transverse plane strain)	168
11.7	Dog-bone flat tensile specimen	169
11.8	Four-point-bending of a pre-cracked pipe	170
11.9	Fragmentation of a thick ring	173
11.10	Uniaxial tension of a hollow round bar	175
12	Microscopic Approach to Fracture - A Modified Gurson Model	177
12.1	Introduction	177
12.2	Yield function	179
12.3	Void coalescence	180
12.4	Void shearing mechanism	182
12.5	Lode angle dependent GTN model	185
12.6	Fracture criterion	188
12.7	Numerical implementation	191
12.8	Numerical simulation	193
12.8.1	Unit cell	194
12.8.2	Uniaxial tension of a round bar	198
12.8.3	Transverse plane strain tension	200
12.9	Conclusions	201

13 Conclusions and Future Research	207
13.1 Conclusions on the damage plasticity theory	207
13.2 Future research	208
13.2.1 Lode angle dependence function	208
13.2.2 Damage accumulation	209
13.2.3 Damage coupling in the material strength	209
A Appendix	211
A: Bridgman Test Results	211
References	215

List of Figures

1.1	A hypothetical load displacement curve in tension.	2
1.2	The triangle to understand the physical world.	4
2.1	A representative sketch of the principal stress vector in the Cartesian system.	8
2.2	The von Mises stress and the deviatoric stresses on the octahedral plane.	9
2.3	A history of strength of ductile materials.	13
2.4	The Lode angle dependence of the existing fracture models.	29
3.1	An arbitrary increment \overrightarrow{AB} in the principal stresses.	35
4.1	An illustrative sketch of a stepwise loading path in the $\varepsilon_p - \sigma_m$ plane.	43
4.2	Evolution of the damage on the material stiffness of 99.99% copper.	44
4.3	A schematic drawing of the damage containing solid and the matrix material.	45
4.4	An illustrative sketch of damage rule and weakening function.	47
5.1	The average hydrostatic pressure experienced in pulling under pressure.	55
5.2	Curve fitting process for material 9-2.	55
5.3	The complete fitting results of Bridgman's tests for various steels.	56
6.1	The stress states of forward and backward simple tension.	65
6.2	The Lode angle dependence of the effective fracture strain.	67
6.3	The normalized effective failure strain versus the ratio of the stress deviators.	68
6.4	A fracture surface in the mean stress and plastic strain space.	70
6.5	A three-dimensional sketch of the fracture surface in the principal stress space.	71
6.6	The ductility ratio vs. the strain hardening.	73

6.7	The normalized effective failure strain versus the ratio of the stress deviators.	76
6.8	The normalized effective failure strain versus the deviatoric state.	76
7.1	The comparison of yielding and plasticity to fracture and damage evolution.	81
7.2	The α , χ and $\frac{\sigma_m}{\sigma_{eq}}$ in the plane stress condition.	83
7.3	The fracture strain versus the stress triaxiality for the plane stress condition.	83
7.4	Notched tube specimen used by Barsoum and Faleskog. After [1]	85
7.5	Fracture strain vs. stress triaxiality and fractures train vs. Lode parameter.	85
7.6	Fracture envelope in stress triaxiality and deviatoric state space.	86
8.1	A schematic drawing illustrates the evolution of the deviatoric stress tensor.	96
9.1	The direction convention for the block of aluminum alloy.	103
9.2	The un-notched and notched round bar specimen.	103
9.3	The post mortem specimens of un-notched and notched round bars.	104
9.4	Different fracture modes were found for un-notched round tensile bars.	104
9.5	Load-displacement curves for un-notched and notched round bar tensile tests.	105
9.6	A schematic sketch of upsetting tests.	106
9.7	A polished and etched cross-section of compressed cylinder.	106
9.8	Upsetting test setups with dry and Teflon friction conditions.	107
9.9	Upsetting test specimens of three heights.	108
9.10	Post mortem upsetting specimens of the first batch.	108
9.11	A sketch shows an annulus type of the crack for compressed cylinder.	109
9.12	Cut out upsetting specimens show the direction and length of the crack.	110
9.13	The load displacement curves of the dry friction condition.	111
9.14	Post mortem upsetting specimens of the second batch.	112
9.15	Experimental load displacement curves of cylinders in the longitudinal direction.	112
9.16	Post mortem small scale tensile specimens in all three principal directions.	113
9.17	Tension and compression curves in all three directions.	114
9.18	The fracture surface of the tensile specimen in the transverse direction (H).	115
9.19	The geometry and dimension of the doubly-grooved plate.	116
9.20	The post mortem plane strain specimen.	116

9.21	The load displacement curves for the transverse plane strain specimens.	117
10.1	Experimental load-displacement curve of upsetting test (specimen A-11-1).	121
10.2	The direction convention for the block of aluminum alloy.	122
10.3	Tensile stress strain curve fitting.	123
10.4	The intrinsic relationship of the stress strain curve of the material.	124
10.5	The four models used in the calibration of the fracture envelope.	126
10.6	The deformation sequences of the upsetting test.	128
10.7	A cut-out damage contour plot for a quarter of the model.	129
10.8	A comparison of the load-deflection curves for compressed cylinder.	130
10.9	The deformation sequences of the upsetting test.	131
10.10	A comparison of the load-deflection curves of un-notched round bar.	132
10.11	The deformation sequences of the tensile 9mm notched round bar.	133
10.12	A comparison of the load-deflection curves of 9mm notched round bar.	133
10.13	The deformation sequences of the transverse plane strain tensile specimen.	134
10.14	The damage rate and the plastic strain contours of plane strain specimen.	135
10.15	A comparison of the load-displacement curves of notched round bar.	136
11.1	The deformation sequences of the notched specimen with $R=18\text{mm}$	138
11.2	A comparison of the load-displacement curve of $R=18\text{mm}$ notched bar.	139
11.3	The deformation sequences of the notched specimen with $R=4.5\text{mm}$	139
11.4	A comparison of the load-displacement curve of $R=4.5\text{mm}$ notched bar.	140
11.5	The crack initiation and propagation in a compressed cylinder.	141
11.6	A deformation sequence of the compressed cylinder in dry friction condition.	142
11.7	A comparison of the simulation load displacement curve with the experimental one.	142
11.8	Deformation sequences of an upsetting test with an intermediate friction coefficient.	143
11.9	A comparison of the load displacement curve for 11.25mm long cylinder.	143
11.10	The deformation sequences of the 6mm long cylinder.	144
11.11	The deformation sequences of the 8mm long cylinder.	144
11.12	The comparison of the load displacement curves for 6mm and 8mm long cylinder.	145
11.13	Test setup of a three-point bending test.	146

11.14	The load displacement curves for the rectangular beams with three different width.	146
11.15	Fracture surface of a wide rectangular beam showing three sections.	147
11.16	Fracture pattern of a wide rectangular beam.	149
11.17	The predicted load displacement curves for the four cases.	150
11.18	Fracture surface of a narrow beam under three point bending test.	151
11.19	Fracture surface of a narrow beam predicted by using present model.	151
11.20	A comparison of the load displacement curve for narrow beam.	152
11.21	The geometry configuration of the compact tension specimen.	154
11.22	The fracture modes of a compact tension specimen for the four cases.	155
11.23	Fracture mode found in the simulation for various n and γ combinations.	156
11.24	The time sequence of the three stages of crack propagation.	158
11.25	Initial skewed mesh for compact tension specimen.	159
11.26	Comparison of normal load vs. load-line displacement for CT test.	160
11.27	The fracture surface of a CT specimen with slant crack.	161
11.28	Comparison of the normal load versus load-line displacement curves.	162
11.29	The crack front of a CT specimen showing the extent of tunneling.	163
11.30	The difference in the tunneling of the flat crack and slant crack propagation.	164
11.31	Simulation results show the tunneling difference	165
11.32	A cup-cone fracture mode is observed in the un-notched round bar.	167
11.33	The formation of shear lips.	168
11.34	A 45° slant crack is observed in the flat grooved plate.	169
11.35	A slant crack is observed for thin-walled flat dog-bone tensile specimen.	170
11.36	The skew mesh ahead of the pre-crack tip.	171
11.37	The overall bending of a circumferentially pre-cracked pipe.	171
11.38	The central portion of the crack of the steel pipe	172
11.39	A slant crack found in a thick ring when applied inner pressure.	173
11.40	The deformation sequence of fragmentation of a thick ring.	174
11.41	A hollow round bar fails in a shear mode.	175
11.42	The the damage accumulation process in a hollow bar.	176
12.1	The competition of three fracture mechanisms.	181

12.2	A schematic drawing illustrates the void shear mechanism.	182
12.3	Two different failure mechanism: internal void necking and void shearing.	183
12.4	The approximate treatment of the nucleation and growth of voids.	186
12.5	The damage evolution in the GTN model and in the present model.	188
12.6	The Gurson yield surface depends on the mean stress and the damage.	190
12.7	A three-element unit cell used to illustrate the modified GTN model.	194
12.8	Comparison of load-displacement and internal variables in simple tension.	195
12.9	Comparison of load-displacement curves for the three models in simple shear.	196
12.10	Internal variables for GTN model.	196
12.11	Internal variables for the damage counter GTN model.	197
12.12	Internal variables for the damage yielding GTN model.	197
12.13	Comparison of the damage evolution in the three models.	198
12.14	Tensile crack of a round bar predicted by three material models.	199
12.15	The contours of χ at the mode transition of the crack from tensile to shear.	199
12.16	Transverse plane strain cracks predicted by three material models.	200
12.17	The line contours of the damage in gaged section of the doubly groove plate.	200
12.18	The line contours of the damage in gaged section of the doubly groove plate.	201

List of Tables

2.1	Material constants for 2024-T351 aluminum alloy	20
2.2	Various cumulative-strain-damage fracture models.	28
4.1	Bridgman’s experimental results. From [2].	42
5.1	Test results of material 9-2, after Bridgman [2].	53
5.2	Material parameters of pressure sensitivity from Bridgman’s tests.	57
6.1	Comparison of the fracture strain in simple tension and torsion.	63
6.2	The difference in ductility of axisymmetric and plane strain tension.	64
6.3	The difference in ductility of axisymmetric and plain strain uniaxial tension.	72
6.4	The material parameters and fracture strain. After [3] and [4].	73
6.5	The strain hardening exponents n versus strain ratio γ_b or γ	77
9.1	The chemical composition of aluminum alloy 2024.	101
10.1	A list of material parameters used as a starting point.	125
10.2	A list of calibrated material parameters	127
11.1	Fixed material parameters in study of n and γ relationship.	156
11.2	A set of material parameters used in the simulations.	166
11.3	Material constants for fracture characterization of the pipe material.	171
12.1	Material parameters for the modified GTN model.	195
A.1	Collected results of the Bridgman’s Tests (after [2], p.50-59.)	211

Nomenclature

A	stress asymmetry in Wilkins model
A_0	original cross-sectional area
A_f	cross-sectional area at fracture
C_0	elasticity stiffness tensor for undamaged material
D	ductile damage
$D_{1..5}$	material parameters in Johnson-Cook model
D_s	reduction of material stiffness
E	Young's modulus
f	void volume fraction
F_N	total void volume fraction that can be nucleated
G	shear modulus
k	exponent in curvilinear Lode angle dependence function
m	damage exponent
n	strain hardening exponent
\mathbf{n}	directional tensor of deviatoric stress
p	pressure

– continued on next page

– continued from previous page

p_{atm}	atmospheric pressure
p_{avg}	average pressure
p_{conf}	confining pressure
$p_{\text{cut-off}}$	cut-off pressure above which fracture occurs in hydrostatic tension
p_{lim}	limiting pressure below which no damage occurs
q	exponent in pressure dependence function
$s_{1,2,3}$	deviatoric principal stress components
s_N	standard deviation of the plastic strain of void nucleation
T	$= \sigma_m / \sigma_{\text{eq}}$, stress triaxiality
T	temperature
T_0	reference temperature
T_{melt}	melt temperature
w	weakening factor
Y	strain energy release rate in Lemaitre model
α	principal stress ratio in plane stress condition
β	exponent in weakening function
β_w	exponent in the Lode angle dependence function of Wilkins model
χ	relative ratio of the principal stress deviators
ϵ_c	critical strain to failure (up limit of integral)
ϵ^e	elastic strain
ϵ_f	equivalent fracture strain
ϵ_{f0}	reference equivalent fracture strain
ϵ_N	mean plastic strain of the distribution of void nucleation
ϵ_p or ϵ^p	equivalent plastic strain
ϵ_{ps}	a equivalent fracture strain at transverse plane strain tension
ϵ_{st}	a equivalent fracture strain at simple tension
ϵ_{tor}	a equivalent fracture strain at simple torsion
ϕ	elevation angle in the cylindrical coordinate system

– continued on next page

– concluded from previous page

Φ	yield function
γ	ratio of fracture strains at $\chi = 0.5$ and at $\chi = 0$
θ	azimuth angle
θ_L	Lode angle
μ_p	pressure dependence function
μ_θ	Lode angle dependence function
ν	Poisson's ratio
σ	stress tensor
$\sigma_{1,2,3}$	maximum, intermediate and minimum principal stress components
σ_{flow}	flow stress
σ_m	mean stress
σ_M	matrix strength
σ_{uts}	ultimate tensile strength
$\sigma_{x,y,z}$	principal stress components
σ_{eq}	equivalent stress
μ	Lode parameter
$ \cdot $	norm of a vector
$(\dot{})$	time derivative

Chapter 1

Introduction

1.1 Background and motivations

The phenomenon of fracture occurs almost everywhere in our daily lives. Our China dishes break into pieces when accidentally dropped on the floor. The pre-notched lid of a food can tears on opening. Some of these instances are spontaneous and some others are controlled by us.

We, human beings, never stop to investigate the nature. Instinctively, we are curious about the formation of cracks and its propagation. The problem of the strength of materials has been one of the most active scientific fields since the *Industrial Revolution*. However, the exploration of fracture starts much earlier than the eighteenth century. Our ancestors, since Neolithic times, have exploited fracture of stones to make sophisticated tools to serve their various needs. It is doubtful, though, that they understood the mechanics and physics of fracture.

The Industrial Revolution promoted the research of strength of materials. Bulks of new materials were produced and used in various new applications. Among various materials, metals were widely used to build bridges, ships, land vehicles, railways, air planes, buildings, artilleries and various appliances. The strength and ductility of metals are greatly appreciated by the modern civilization. However, it is also known that the strength of materials is not unlimited. When exceeding the load carrying capacity, materials fail by fracture. The exact failure modes may differ, but the sequence of such devastating failures can often be illustratively sketched in Fig. 1.1.

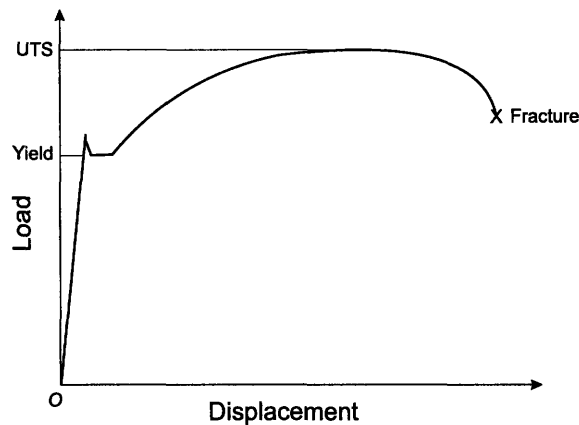


Figure 1.1: A hypothetical load displacement curve in tension.

Usually, the material displays some elasticity which is fully recoverable when the load is removed. However, beyond a certain limit, often called the elastic limit, a part of deformation is unrecoverable. This is called plasticity. Due to strain hardening, the plastic deformation is still stable until the ultimate tensile strength (UTS) is hit. Beyond this peak loading, the deformation is unstable and soon leads to fracture.

Fracture prediction in large-scaled structures that are subjected to extreme loading conditions has been of utmost interest in the scientific and engineering community over the past century. Theoreticians want to understand how the fracture phenomenon fits into the general theory of continuum mechanics. Practitioners on the other hand want to solve industrial problems, such as the sheet metal forming, the automotive crashworthiness, the ship grounding, etc. Both of the theoreticians and practitioners have been the most active sources in the understanding related to ductile fracture.

1.2 Research objectives

The term “*ductile fracture*” in literature is somewhat ambiguous and has roughly two meanings. “Ductile fracture” is often referred to the void nucleation-growth-coalescence (VNGC) type of fracture observed as opposite to the cleavage type of fracture. The fracture surface of this type of failure is usually macroscopically rough; on the contrary, the fracture surface in a cleavage fracture is relatively smooth and flat. In a more general sense, “ductile fracture” relates the scale of plasticity

with respect to the scale of the structure and is not related to a specific type of fracture. “Ductile fracture” refers to fractures where materials experience large plastic deformation and exhibit high ductility in the concerned region where structural failure occurs. In the present research, the broader sense of “ductile fracture” is used.

Various approaches have been proposed to describe the phenomenon of fracture. Such approaches include the concepts of the stress intensity factor, energy release rate, J-integral, meso-scale void-nucleation-growth-coalescence models and continuum damage mechanics models etc. In the present research, a macroscopic descriptive damage plasticity model is proposed. This model is based on the cumulative-strain-damage method, which describes local damage accumulation rather than using far-field stress and strain variables.

Typically, the problem of fracture initiation in large structures involves both material and geometrical non-linearities. Therefore, little can be done analytically and a numerical approach is taken in most engineering applications. On the other hand, with the help of increasing computational power of modern computers, the nonlinear finite element codes are challenged to cope with more complicated problems, such as fracture and fragmentation. A robust fracture prediction model that is suitable for numerical implementation is *de facto* the strongest driving force in the area of the fracture research. The challenges are three-fold: (1) the physical phenomenon of the onset of fracture and crack propagation are not yet fully understood; (2) the fracture model must be suitable for numerical implementation and (3) the model parameters should be convenient for calibration.

The objective of the present thesis work is to develop a robust predictive method for crack initiation and propagation in ductile solids. For that purpose, efforts are made to better understand the fracture initiation on a theoretical basis. A new damage plasticity theory is proposed. This theory explains well many existing experimental results and is further validated by a series of tests. The numerical implementation has been performed and a series of numerical studies were conducted to verify the proposed fracture model. In addition to the damage plasticity model, a parametric study is carried out using a modified micro-mechanism based model, which will be shown later in this thesis to possess some qualitatively improved feature compared to the existing damage models and captures realistic modes of fracture.

A successful model depends on an understanding of the physical world upon which an idealized

theory can be proposed. On the other end, the computer simulation is a powerful tool to verify the model and to predict the real world in return. A sketch of this three-pole learning structure is illustrated in Fig. 1.2. In the present study, an equal emphasis is given to three poles of the learning triangle.

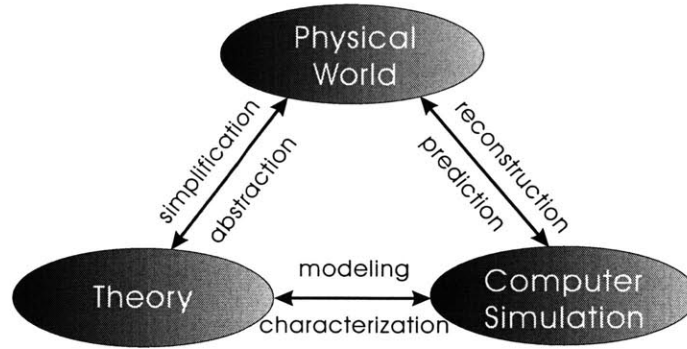


Figure 1.2: The roles of physical world, abstract theory and computer simulation in understanding the mechanism of fracture.

1.3 Scope of research

A damage plasticity model using local field variables such as the stress and strain is proposed. Specifically, this theory is based on a structure of the so-called “*cylindrical decomposition*”. The functional forms of the constitutive equations are given. This new model is applied to predict the entire range of elastic-plastic deformation up to fracture point. The damage plasticity algorithm has been implemented into a commercial code - LS-DYNA, as a user-defined material subroutine. The stress integration scheme is also presented.

Following the theoretical part, a combined experimental and numerical program is carried out to verify and validate the proposed model. A material calibration procedure is shown and the calibrated material constants are used in further calculations. A series of numerical simulations illustrate the predictive capability of the present model. The predicted fracture patterns and load-displacement characteristics are compared with experimental observations. Good agreement is achieved.

In addition to the proposed macroscopic model, a modification to the microscopic Gurson model is also made to include the damaging mechanism of void shearing. A parametric study is carried

out to show qualitatively that this modification removes the shortcoming in predicting a simple shear fracture when using a Gurson-based model. Moreover, the introduction of the void shearing effect to the modified model shows more realistic fracture behavior of ductile metals due to the incorporation of the Lode angle.

1.4 Outline of the thesis

The present thesis consists of thirteen chapters, an appendix and a bibliography of cited references. The thesis is arranged mainly into two parts. The first part provides the theoretical background and extends from Chapter 2 to Chapter 8. A new damage plasticity model is proposed. The second part of the thesis from Chapter 9 to 12 details an experimental program and a numerical verification. In conjunction to the macroscopic development, Chapter 12 describes a modified micro mechanical model including void shearing. Below is a list of contents in each chapter.

Chapter 1 gives motivation, defines objectives and presents an outline of the thesis.

Chapter 2 provides a short history of strength of materials and an overview of the existing fracture models.

Starting from Chapter 3, a new generic macroscopic model is presented based on the pressure sensitivity, the Lode angle dependence, the damage evolution law and material weakening.

The concept of the damage evolution and associated material weakening is further extended in Chapter 4.

Chapter 5 describes the pressure sensitivity of ductile fracture using existing experimental results.

Chapter 6 provides a phenomenological way to characterize the Lode angle dependence of ductile fracture.

Chapter 7 gives the summary of the proposed damage plasticity model and a special case of plane stress is analyzed.

Chapter 8 describes the elasto-plastic constitutive equations and the numerical integration procedure.

Chapter 9 describes the experimental program that is used to determine the material properties for aluminum alloy 2024-T351.

Chapter 10 shows the calibration procedure for the material constants for aluminum alloy 2024-T351.

Chapter 11 presents a series of numerical simulations showing the predictive capability of the proposed model. Several representative simulations show realistic results.

Chapter 12 describes a modification to the meso scale void nucleation growth and coalescence model by introducing void shearing mechanism.

Chapter 13 concludes the present thesis, summarizes major results and suggests future research topics.

Chapter 2

A Brief Review of Existing Damage and Fracture Criteria

Large amount of theoretical work in mechanics are based on the principal stress space. To facilitate discussion on the damage and plasticity modeling technique, we start by a short description of the principal stress space and the connection between the principal stress components and the stress invariants.

2.1 Principal stress space

The state of the principal stresses can be geometrically represented by a vector in the three-dimensional space where the principal stresses are taken as the Cartesian coordinates, as shown in Fig. 2.1. The Cartesian principal space is reinterpreted identically in a cylindrical coordinate system aligned with the hydrostatic axis on the same origin. The azimuth angle θ in cylindrical system is defined on the octahedral plane starting from a deviatoric axis. The z axis in the cylindrical system is the triad axis, where the three principal stresses are equal.

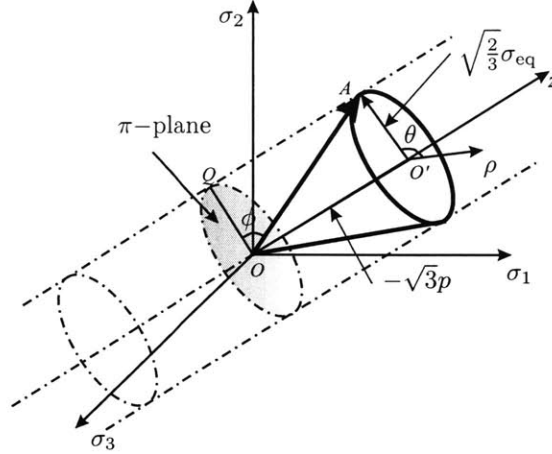


Figure 2.1: A representative sketch of the principal stress vector \overrightarrow{OA} in the three-dimensional Cartesian system. The Cartesian description $(\sigma_1, \sigma_2, \sigma_3)$ can be transferred to the cylindrical coordinate system $(p, \theta, \sigma_{\text{eq}})$.

The principal stress vector which represents the stress state $(\sigma_1, \sigma_2, \sigma_3)$ is shown in Fig. 2.1 as \overrightarrow{OA} . It can be readily decomposed into two component vectors, which are perpendicular to the octahedral plane, i.e. $\overrightarrow{OO'}$, and in the octahedral plane, i.e. $\overrightarrow{O'A}$. The vector $\overrightarrow{OO'}$ represents the hydrostatic pressure and the vector $\overrightarrow{O'A}$ represents the deviatoric term. The magnitude of these two vector components is linearly related to the hydrostatic pressure and the von Mises equivalent stress, respectively, i.e.

$$|\overrightarrow{OO'}| = -\sqrt{3}p, \quad \text{and} \quad |\overrightarrow{O'A}| = \sqrt{\frac{2}{3}}\sigma_{\text{eq}}, \quad (2.1)$$

where $|\cdot|$ denotes the norm of the vector, $p = -\frac{1}{3}(\sigma_1 + \sigma_2 + \sigma_3)$ is the hydrostatic pressure, and $\sigma_{\text{eq}} = \frac{1}{\sqrt{2}}\sqrt{(\sigma_1 - \sigma_2)^2 + (\sigma_2 - \sigma_3)^2 + (\sigma_3 - \sigma_1)^2}$ is the von Mises equivalent stress.

The deviatoric stresses can be shown as the projection of the deviatoric principal stress on the octahedral plane, as shown in Fig. 2.2.

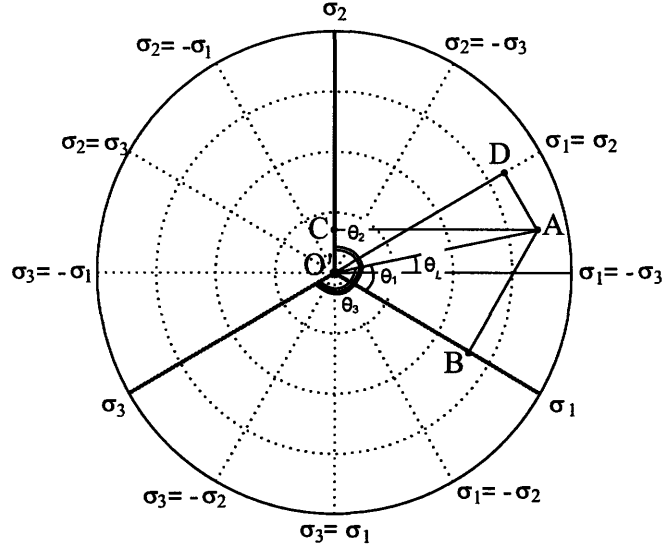


Figure 2.2: The von Mises stress and the deviatoric stresses on the octahedral plane.

The elevation angle ϕ , i.e. the angle to the π -plane, is related to the stress triaxiality. The azimuth angle can be characterized by the Lode angle [5], as shown in Fig. 2.2, which is defined as

$$\theta_L = \tan^{-1} \left\{ \frac{1}{\sqrt{3}} \left[2 \left(\frac{s_2 - s_3}{s_1 - s_3} \right) - 1 \right] \right\}. \quad (2.2)$$

The Lode angle is not defined on hydrostatic axis where $s_1 = s_3$. It is widely used in the granular material community and the influence of the Lode angle is often referred as the “Lode angle dependence” [6]. In the present paper, the relative ratio of the deviatoric principal stress is used to represent the azimuth angle θ , which is defined as the angle to the positive direction of the s_1 axis, i.e. θ_1 in Fig. 2.2. The relative ratio of the principal deviatoric stress is defined as

$$\chi = \frac{s_2 - s_3}{s_1 - s_3}, \quad (2.3)$$

where s_1 , s_2 and s_3 are the maximum, intermediate and minimum principal stresses respectively. The azimuth angle θ can be uniquely expressed in terms of the relative ratio of the principal deviatoric stress, i.e.

$$\theta = \cot^{-1} \left[\frac{2}{\sqrt{3}} \left(\frac{1}{\chi} - \frac{1}{2} \right) \right] \quad \text{or} \quad \chi = \frac{2}{\sqrt{3} \cot \theta + 1}. \quad (2.4)$$

Let the second and third invariants for the deviatoric stress to be signified by

$$\left. \begin{aligned} J_2 &= \frac{1}{2} (s_1^2 + s_2^2 + s_3^2); \\ J_3 &= s_1 s_2 s_3. \end{aligned} \right\} \quad (2.5)$$

which can be co-related with the azimuth angle by

$$\cos(3\theta) = \frac{3\sqrt{3}}{2} \frac{J_3}{J_2^{3/2}} = \frac{27}{2} \frac{J_3}{\sigma_{\text{eq}}^3}. \quad (2.6)$$

For each sextant of the octahedral plane, the azimuth angle θ and the value $\frac{27}{2} \frac{J_3}{\sigma_{\text{eq}}^3}$ can be one-to-one mapped. It is also noted that

$$\theta = \theta_L - \frac{\pi}{6}. \quad (2.7)$$

2.2 A historical note on fracture

To gain perspective, we begin by reviewing the development of the theory of material strength in some generality. In particular, we are interested in ductile materials, such as polycrystalline metals and alloys. It is the purpose of this chapter to provide an overview of fracture models and related issues. The review is brief and makes no attempt to be exhaustive.

People learned about fracture long before it became an active branch in the scientific field of the strength of materials. It may be argued that the publishing of the Galileo's famous book "*Two New Sciences*" marked the starting of the science of **strength of materials**, though our ancestors have undoubtedly shown some sort of knowledge in earlier ages in their practice of tool-making and tool-using [7]. It is worthwhile to list the early understandings in this area before we explore the more advance later developments.

The first historically recorded study of fracture strength was made by Leonardo da Vinci (1452-1519) on the tensile strength of short iron wire. One of the most important early works was carried out by E. Mariotte (1620-1684) who was a court engineer for Louis XIV of France. He noted that the pressurized vessels burst at a certain value of the circumferential stretch. He related the

circumferential stretch to the increase of pressure. This observation led to the maximum strain and maximum stress criterion, which are still in practice [8].

The real world is much more complicated than what a critical strain or stress criterion can predict. The well-known maximum shear stress criterion, as known as Tresca's criterion was actually introduced by Coulomb. Coulomb (1736-1806) showed the applicability of the maximum shear stress as a failure criterion. He (1776) also noted that the strength in compression would be enhanced due to internal friction along the shear plane. Mohr (1836-1918) provided a graphical representation of the Coulomb theory [8]. The octahedral shear stress was also used as a failure condition. This criterion was first introduced by Maxwell and later Huber (1904) [9], von Mises (1913) and Hencky developed it independently. Beyond yielding point, the permanent plastic deformation suggests some sort of damage have taken place in the micro structure of the material.

From von Mises or Tresca yield condition, yielding does not occur under pure hydrostatic tension because the shape of the von Mises or Tresca yield surface does not touch the hydrostatic axis. At a sufficiently high hydrostatic tension, the material may rupture before yielding occurs. The Coulomb-Mohr yield criterion acknowledges the pressure dependence by using σ_t and σ_c to denote the yield stress at simple tension and simple compression. The pressure effect on yielding for ductile metals is often considered to be low and often neglected.

In the classical continuum mechanics, the material is considered homogeneous at a length scale of structure level. This assumption breaks down at the micro scale where the size of grains and particles become nonelible. In reality, second phase particles and inclusions are constantly found in commercially available alloys, such as in carbon steel. The second phase particles are normally harder than the base metal. Even under hydrostatic tension, higher microscopic stresses exist around these particles. Therefore, micro plastic flow occurs and inhomogeneities arise.

In one way, the yielding to plasticity is the fracture to damage in the sense that the former is often thought to be an abrupt event and the later to be progressive process. The yielding is the beginning of the plastic flow and the fracture is the ultimate event for ductile damage accumulation. An increasing effort has been devoted since 1960's to a more comprehensive understanding of damage and fracture initiation. Ductile fracture criteria are proposed from different perspectives. Among all the developments, the most influential factors introduced to the damage characterization are the pressure dependence, the non-linear damage evolution and the damage induced weakening.

In another word, the damage process is considered to be dependent on the first and second stress invariants. Although pioneer study has shown some significance, an important factor which is often missing is the dependence on the third stress invariant, i.e. the azimuth angle on an octahedral plane. It will be demonstrate the ductile fracture is strongly influenced by the third stress invariant.

It is interesting to compare the developments in the yielding/plasticity and the fracture/damage in the past 400 years. A sketch of historical developments and their time is shown in Fig. 2.3. The development in different aspects of solid mechanics in understanding material strength is categorized into nine columns. Constant values were first adopted for yielding and fracture. It followed by the advances in the pressure dependence of yielding and fracture. Another important aspect is the dependence of azimuth angle of the principal stresses. The azimuth angle is defined as the angle of the projection of the principal stress vector on the π -plane. The evolution laws of plasticity and damage have been attracted much attention in the past century. Finally, the coupling of the damage with yield condition completes the damage plasticity constitutive equations. In the present thesis, we focus in the discussion of the damage evolution under arbitrary loading path and the coupling of damage and yield condition. In view of the advances shown in Fig. 2.3, it is clear that the azimuthal dependence of ductile fracture is the least studied topic in the history of mechanics.

A history of strength of ductile materials

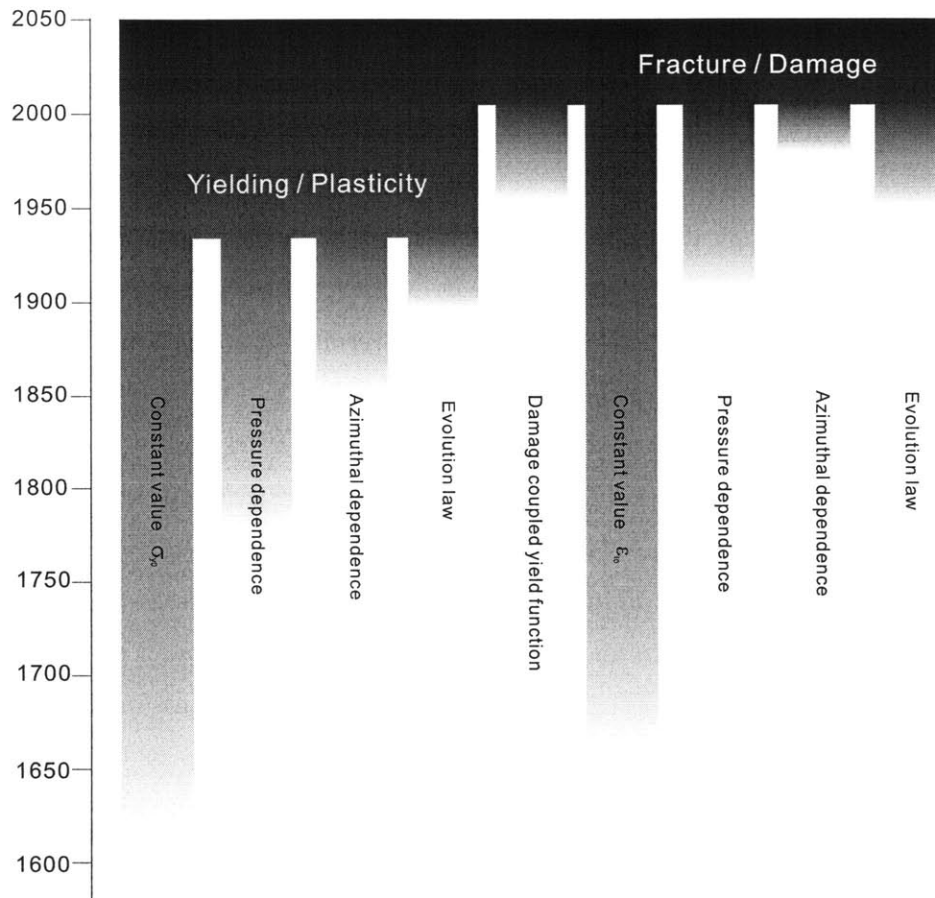


Figure 2.3: A history of strength of ductile materials.

2.3 Damage plasticity

What happens beyond moderate plasticity?

Considering the solid material as a continuum, up to moderate plastic deformation, the microstructure of materials can be thought to be unchanged. By moderate plastic deformation, we refer to a deformation state that the plastic strain is significantly greater than the elastic strain, but much less than the fracture strain at the current pressure and the azimuth angle. For practical purpose, classical plasticity theory is sufficient in dealing with many engineering applications. However, when deformation is beyond moderate plasticity, the changes in microstructure are no longer

insignificant and should not be ignored. Indeed, such change plays an important role predicting the ultimate fracture.

From experimental observations, the ductile failure of structures usually consists of three phases: (a) accumulation of damage; (b) initiation of fracture; and (c) crack propagation. One way to think of fracture initiation is to consider it as the result of the accumulation of the ductile plastic damage [10; 11]. Microscopically, such damage associates with the void nucleation, growth and coalescence, shear band movement and propagation of micro-cracks. Macroscopically, the degradation of the material exhibits a decrease of the material stiffness, strength and a reduction of the remaining ductility. These physical changes are often used as an indicator to predict the onset of fracture, either based on the current value or in a cumulative fashion. In continuum damage mechanics, the material deterioration is described by an internal variable - the so-called “damage”. It is argued that the damage is anisotropic and has to be modeled by a tensorial quantity in general [12]. However, in many industrial applications, the damage is assumed as an isotropic entity and is treated as a scalar. In many applications, the consideration of the isotropic damage has often led to good predictions [11; 13]. Therefore, the damage is assumed in this thesis to be a scalar quantity. Damage should be distinguished from the ductility or the fracture strain in that damage is an internal quantity, which usually can not be measured directly. To utilize the cumulative damage as a criterion to predict the onset of fracture, the relationship of damage with respect to some measurable quantities has to be established. Damage models are proposed to link the measurable field variables to the evolution of the damage process toward the fracture. Some of these damage models can be found in [14]. For instance, [15] proposed the concept of effective load carrying area to quantify the damage.

Two approaches are often used in the study of the nature and mechanical behavior of engineering materials. One is the macroscopic approach in which the material is represented by its aggregate response. The other approach is a microscopic approach in which the evolution of microscopic structure of the material is used to model the global behavior of structures.

For small and moderate plasticity, the damage effect to the matrix strength curve is often negligible and, therefore, the material strength curve is assumed to be equal to the matrix strength curve. The classic continuum mechanics assumes that there exists a one-to-one mapping from the history of plastic strain to the yield strength. This type of plasticity has been practiced in many en-

gineering applications. However, it is often not sufficient in dealing with large deflection problems in many cases involving ductile fracture. When the plastic deformation is beyond moderate plasticity, the damage effect on the material strength is profound. Such deterioration is often exaggerated by the material weakening induced localization. Therefore, the damage and the plasticity are coupled in the plastic loading paths and their joint effects have to be described in the constitutive model in order to predict ductile fracture of metals.

2.4 Damage modeling approaches

Macroscopic models are constructed based on the macroscopic field variables. Such field variables are components of the stress and strain tensors, their increments and sometimes temperature and strain rate. It has been shown by various experiments that the damaging process that eventually leads to fracture of material exhibits strong dependence on the loading history. Therefore, some sort of damage variable has to be used to take into account the history effect.

Let us begin with some general comments on the methodologies of developing a macroscopic fracture model. Various fracture models have been proposed to quantify the damage associated with material deformation and are used to predict the fracture initiation, e.g. [3; 16–27].

Historically, many models consider the damaging process as being independent of the material plasticity behavior. In other words, plasticity properties of the material do not change, as the damage accumulates in the material volume. In these models, a separate damage variable is used to count toward the initiation of fracture. Johnson-Cook model [3; 28] and Wilkins model [22] are examples of such conventional continuum mechanical models. The advantage of these models is that the damage evolution and the plasticity evolution are uncoupled in the stress integration procedure. The disadvantage is that the fracture is modeled as a sudden drop of stress-strain curve, where the mechanical response of the material is over simplified. As far as fracture mode is concerned, these models often incorrectly predict the fracture modes due to the lack of damage induced weakening and the unrealistic strengthening in the later stage of deformation.

On the other hand, the continuum damage mechanics considers the damage process is inherited to the material strength. In continuum damage mechanics, the macroscopic behavior of solids is separated from its matrix material. The fracture is modeled as a continuous degradation of the matrix material. In this way, the material deterioration is modeled explicitly and the complete loss

of the load carrying capacity occurs at the onset of fracture. More computational efforts are needed in this regard and will be discussed later.

Experimental results show that the fracture initiation of uncracked solids is sensitive to hydrostatic pressure and is dependent on the Lode angle. The hydrostatic tension speeds up both the void nucleation-growth-coalescence process and the shear band slip movement; while the compressive pressure slows down such actions. The Lode angle characterizes the deviatoric loading on a hydrostatic plane in the principal stress space.

As the conventional J_2 plasticity does not include damage and fracture, some sort of threshold criteria may be used to describe the onset of fracture. In a more realistic fashion, an additional damage variable is used to count toward fracture. In particular, this damage is directly linked to the unrecoverable plastic strain (or in its rate form). This line of modeling approach is often called the cumulative strain damage method. The material is considered to be homogenous and the plastic deformation is incompressible. Acknowledging that the damage is associated with the plastic deformation, damage plasticity models assess the damage using an integral of a weighting function with respect to the equivalent plastic strain and further incorporate the damage into the yield condition. A weighting function describes how fast the damage accumulates at the current combination of material damage and the loading condition. When the accumulated damage exceeds a threshold value, the material is considered to fail.

Experimental work shows that the compressive pressure increases the ductility in many ductile and brittle materials, such as metals [2; 29–36] and rocks [37–39]. Empirical equations have also been proposed by many researchers.

Experimental results also show a strong dependence of fracture initiation on this azimuth angle for some materials [2; 22; 26; 40–44]. Clausen[40] pointed out the distinct difference in the equivalent fracture strain between the round bar (axial symmetry) and the flat grooved plates (plane strain) from tests of several metals. Wilkins, *et al.*[22] proposed an empirical model based on the stress asymmetry parameter.

The cumulative strain damage models assume that the damage toward eventual fracture is due to the plastic deformation history of the material. For a given material, when the accumulated damage exceeds a critical value, D_c , i.e.

$$D \geq D_c, \quad (2.8)$$

the material is considered to be failed. The threshold of damage at which fracture occurs depends for each material on the weighting function. Equation (2.8) can be normalized with respect to the critical value D_c such that the critical value of the damage is unity. The fracture criterion of the normalized cumulative strain damage model becomes

$$D = \int_0^{\varepsilon_c} f(\text{field variables}) d\varepsilon_p = 1. \quad (2.9)$$

where ε_c is the critical value of equivalent plastic strain at fracture for the given loading path and ε_p is the plastic strain. The integrand, the so-called weighting function of damage, is considered as a function of the stress state, temperature, the strain rate, etc. In other words, the cumulative strain damage model can be formally written as

$$D = \int_0^{\varepsilon_c} f(\boldsymbol{\sigma}, \boldsymbol{\varepsilon}, T, \dot{\boldsymbol{\varepsilon}}) d\varepsilon_p. \quad (2.10)$$

where $\boldsymbol{\sigma}$ and $\boldsymbol{\varepsilon}$ are stress and strain tensor and T is the temperature. This line of research has been pursued by many researchers. In the present paper, the discussion is focused on the effect of the stress state on fracture. For thermal effects and strain rate effects, the readers are referred to references cover the related topics, such as Johnson and Cook [3; 45]. Hence, the weighting function reduces to the form of $f(\boldsymbol{\sigma}, \boldsymbol{\varepsilon})$ from now on.

Let us consider a given triaxial stress state in the principal stress space. There is exactly one deviatorically proportional loading path at the pressure and the azimuth angle of the given stress state. The loci of ultimate fracture points from the exhaustive set of such deviatorically proportional loading paths uniquely define a *fracture envelope* in the three-dimensional principal stress space.

The exact configuration of the *fracture envelope* is defined by the combined effect of the hydrostatic pressure and the deviatoric state. It is postulated that their effects can be uncoupled. A “*six point star*” is proposed to represent the Lode angle dependence on the strain plane with its vertices pointing to the positive and negative directions of the three principal strain axes. The three-dimensional representation of this fracture surface is a “*blossom*” aligned with the hydrostatic

axis, where the three principal stresses are equal. The hydrostatic pressure governs the size of this “*six point star*”. The deviatoric state determines the exact fracture point on the “*six point star*”. The ratio of the minimum and the maximum radius on the “*six point star*” reflects the difference in the fracture strain from generalized shear, generalized tension and generalized compression loading, which is considered as a material property and is determined through experiments.

At an incremental level, the incremental stresses and the change of the configuration is governed by the flow rule. The damage along the deviatorically proportional loading path is described by the damage rule. One of the simplest form of the damage rule is assuming the incremental damage is proportional to the incremental strain, as is used in [3] and [22] etc. Experimental work shows the accumulation of damage along the plastic strain path is not necessarily linear with the equivalent plastic strain.

The nonlinearity of the damage with respect to the plastic strain is described by the *damage rule*. A simple power law is proposed. With the fracture envelope and the damage rule, a fully three-dimensional fracture prediction model is established.

The fracture is a sudden change in the configuration, but the damage is a cumulative process. Two concepts are used in the present model. One is the “*fracture envelope*”, which is defined on a class of deviatorically proportional loading path in the principal stress space. The other is the “*damage rule*”, which provides a tool to quantify the amount of damage resulting from the plastic deformation. In this sense, the deviatorically proportional loading path serves as a reference loading condition from which the incremental damage can be calculated for arbitrary loading cases.

2.4.1 Conventional continuum mechanics models

Although very complex when examined on the microscale, at the macroscale, many ductile materials such as metals may be idealized as continua. Conventional continuum mechanics ductile fracture models falls in the category of class plasticity theory. In these models, the damage is treated as a separate variable that is independent of the material strength. Some of these models are described below.

Johnson-Cook

A widely used representative material constitutive model is the Johnson-Cook model. Accompany with its strength function, Johnson and Cook also present the associated failure function,

which takes the form of a product of three affecting factors, namely stress triaxiality, strain rate and the temperature.

The Johnson-Cook strength model is an empirical equation and is also widely used in practical simulation for its broad consideration of plastic hardening, strain rate sensitivity and temperature weakening. In the Johnson-Cook model, the equivalent stress, σ_{eq} , is expressed as the following function of the equivalent plastic strain, ε_p , the temperature, T , and the plastic strain rate, $\dot{\varepsilon}_p$ [3]:

$$\sigma_{\text{eq}} = [A + B\varepsilon_p^n] \left[1 + C \ln \left(\frac{\dot{\varepsilon}_p}{\dot{\varepsilon}_0} \right) \right] \left[1 - \left(\frac{T - T_0}{T_{\text{melt}} - T_0} \right)^q \right], \quad (2.11)$$

where $\dot{\varepsilon}_0$ is the plastic strain rate, T_0 and T_{melt} are the room temperature and the material melting temperature, respectively, A , B , n , C , and q are five material constants. The Johnson-Cook model accounts for isotropic strain hardening, strain rate hardening, and temperature softening in the uncoupled form. The first term of the right hand side in Eq. (2.11) represents the quasi-static stress-strain relation at room temperature; the second term signifies the strain-rate hardening; the third term means the temperature dependence of the stress-strain relation.

The fracture criterion used in the Johnson-Cook model is a weighted integral with respect to the effective strain [46], see Eq. (2.12).

$$D = \int_0^{\varepsilon_c} \frac{d\varepsilon_p}{\varepsilon_f \left(\frac{\sigma_m}{\sigma_{\text{eq}}}, \dot{\varepsilon}_p, T \right)}, \quad (2.12)$$

where $\frac{\sigma_m}{\sigma_{\text{eq}}}$ - the so-called the stress triaxiality - is used to represent the pressure dependence. The general form of the weighting function is the reciprocal of the effective failure strain which is treated as a function of the stress triaxiality status, the strain rate and the temperature, as shown in Eq. (2.13).

$$\varepsilon_f = \left[D_1 + D_2 \exp \left(D_3 \frac{\sigma_m}{\sigma_{\text{eq}}} \right) \right] \left[1 + D_4 \log \frac{\dot{\varepsilon}_p}{\dot{\varepsilon}_0} \right] \left[1 + D_5 \frac{T - T_0}{T_{\text{melt}} - T_0} \right], \quad (2.13)$$

where D_1, D_2, D_3, D_4 and D_5 are material constants. For aluminum alloy 2024-T351, these constants are listed in Table 2.1 [47].

Table 2.1: Material constants for 2024-T351 aluminum alloy

A (MPa)	B (MPa)	n	$\dot{\epsilon}_0$ (s ⁻¹)	C
352	440	0.42	3.33×10^{-4}	0.0083
T_{melt} (K)	T_0 (K)			
775	293			
D_1	D_2	D_3	D_4	D_5
0.13	0.13	-1.5	0.011	0.0

In Eq. (2.13), the effect of pressure, strain rate and temperature is expressed as the product of the three independent factors. Neglecting the strain rate effect and the thermal effect and knowing the mean stress σ_m is the negative value of the pressure p , Eq. (2.13) can be expressed in a Taylor series expansion around zero stress triaxiality and the leading terms are

$$\epsilon_f = D_1 + D_2 + D_2 D_3 \frac{\sigma_m}{\sigma_{\text{eq}}} = (D_1 + D_2) - D_2 D_3 \frac{p}{\sigma_{\text{eq}}}. \quad (2.14)$$

For many metals, the coefficients D_2 is positive and D_3 is negative [3]. Thus, an increase in the compression hydrostatic pressure will result in an increase in the fracture strain of the material. Furthermore, from Eq. (2.14), the fracture strain is linearly related to pressure for non-hardening materials. The slope at zero pressure can be used to compare material parameters for different material models.

Wilkins, et al.

Wilkins et al [22] proposed the failure strain envelope as a product of two parts: the hydrostatic tension and stress asymmetry. The Wilkins criterion states

$$D = \int_0^{\epsilon_c} w_1 w_2 d\epsilon_p \geq D_c, \quad (2.15)$$

where

$$w_1 = \frac{1}{(1 + ap)^\alpha} \quad (2.16)$$

and

$$w_2 = (2 - A)^{\beta w} \quad (2.17)$$

where a , α and β_w are material constants and

$$A = \max\left\{\frac{s_2}{s_1}, \frac{s_2}{s_3}\right\} \quad (2.18)$$

where s_1, s_2 and s_3 are the ordered principal stress deviators. Considering the stress deviators subject to the constraint that their sum equals zero, “the stress eccentricity” A could also be expressed as

$$A = \max\left\{-\frac{s_3}{s_1}, -\frac{s_1}{s_3}\right\} - 1 \quad (2.19)$$

The material fails when the damage exceeds a certain threshold D_c . This criterion can be normalized as

$$D = \int_0^{\varepsilon_c} \frac{(3 - \max\{-\frac{s_1}{s_3}, -\frac{s_3}{s_1}\})^{\beta_w}}{D_c(1 + ap)^\alpha} d\varepsilon_p \quad (2.20)$$

where fracture occurs when $D \geq 1$.

From Eq. (2.20), the failure strain function could be written as

$$\varepsilon_f = D_c \frac{(1 + ap)^\alpha}{(3 - \max\{-\frac{s_1}{s_3}, -\frac{s_3}{s_1}\})^{\beta_w}} \approx D_0 \frac{(1 + a\alpha p)}{(3 - \max\{-\frac{s_1}{s_3}, -\frac{s_3}{s_1}\})^{\beta_w}} \quad (2.21)$$

While w_2 accounts for the Lode angle dependence, the pressure effect enters through the power function, which can be expressed in a first order approximation

$$\mu_p = (1 + ap)^\alpha \approx 1 + a\alpha p. \quad (2.22)$$

The linear approximation in Eq. (2.21) is accurate to the first order when the hydrostatic pressure is small compared to $\frac{1}{a}$, which has a unit of pressure.

By considering a uniaxial tension case, we can compare the coefficients in Eq. (2.14) and (2.22). We establish an approximate relationship for the parameters used in Johnson-Cook and Wilkins models:

$$a\alpha = \frac{D_2 D_3}{(D_1 + D_2) \sigma_y} \quad (2.23)$$

for non-hardening materials of yield stress σ_y .

2.4.2 Micro mechanical models

The microstructure of metals is complex and contains multiphase materials, such as grains, second phase particles, precipitates and voids. Unlike macroscopic homogeneous assumptions, the micro mechanical models treat the materials as a cluster of inhomogeneous cells.

The damage accumulation process that leads to ductile fracture is a very complex phenomenon. The metallurgical observation reveals that the fracture of ductile solids often starts with nucleation, growth and coalescence of micro voids under nominally uniform tensile stress field or ahead of a crack tip. Therefore, the material is considered as a porous media.

One particular type of fracture prediction models are based on the microscopic mechanism of void nucleation, growth and coalescence (VNGC). A great deal of research was focused on the evolution of voids subjected to various types of remote stressing or straining. In these microscopic models, the void is modeled by a hole surrounded by undamaged material (the matrix) which obeys conventional continuum mechanics. The global response of the void containing material (often as in a representative volume element (RVE)) is then used to model the macroscopic behavior of the macroscopic material. Due to the enormous combination of the possible size, shape, orientation and spacing of the voids and the remote deformation pattern, simplifications and assumptions have to be made to make the mathematical problem of void evolution tractable. The pioneering work is due to McClintock [17] and Rice and Tracey [19] who analyzed an isolated cylindrical or spherical shaped void that is subjected to uniform remote stressing. In the VNGC models, the material is often considered as a porous media and the fracture occurs when the void volume fraction reaches a critical value. Gurson[16] introduced the influence of micro-voids to the plastic flow into the constitutive framework. Tvergaard[48] and Tvergaard and Needleman [49] extended it to describe the acceleration of void growth.

McClintock

McClintock analyzed a long cylindrical cavity in a non-hardening material pulled in the axis direction while subjected to transverse tensile stresses [17]. The growth of the cylindrical hole is governed by

$$d \log \frac{b}{b_0} = \sqrt{3} \sinh \left(\frac{\sqrt{3} \sigma_{r \text{ inf}}}{\sigma_{r \text{ inf}} - \sigma_{z \text{ inf}}} \right) d\varepsilon_{r \text{ inf}} + d\varepsilon_{r \text{ inf}} \quad (2.24)$$

where Δ indicates an incremental value, z denotes axial direction, r denotes radial direction, subscript inf denotes remote values, b_0 is the original radius of the hole and b is the instant value.

McClintock [17] also extrapolated Berg's viscous solution [50] for elliptical voids to plastic materials with strain hardening. The damage model can be expressed as

$$dD = \frac{1}{\log F_{zb}^f} \left[\frac{\sqrt{3}}{2(1-n)} \sinh \left(\frac{\sqrt{3}(1-n)(\sigma_a - \sigma_b)}{2\sigma_{eq}} \right) + \frac{3}{4} \frac{\sigma_a - \sigma_b}{\sigma_{eq}} \right] d\varepsilon_p \quad (2.25)$$

where $\log F_{zb}^f$ denotes the maximum sustainable deformation of the representative cell, σ_a and σ_b are the transverse stresses, σ_{eq} is the equivalent stress, ε_p is the equivalent plastic strain, n is the strain hardening exponent and D denotes the damage. The fracture occurs when D reaches unity.

Two of the most important results from McClintock's result are: (1) the very strong inverse dependence of fracture strain on tensile stress transverse to the holes; (2) the relatively strong dependence of fracture strain on the transverse (intermediate) principal stress, rather than solely on the mean normal stress or the maximum principal stress [17].

Rice-Tracey

Rice and Tracey considered the growth of a spherical void in non-hardening material. A spherical void subjected to remote uniaxial tension strain rate field not only grows in radial direction, but also the shape changes. Rice and Tracey showed that for large stress triaxiality, the volume change of the voids far overwhelm the shape changing. They obtained the growth rate of the radius of voids is

$$\frac{\dot{R}}{R_0} = 0.283 \exp \left(\frac{3\sigma_m}{2\sigma_y} \right) \dot{\varepsilon} \quad (2.26)$$

where R_0 is the original void radius, R is the current value, σ_m is the remote mean stress and σ_y is the yield stress. For a hardening material under proportional stressing, the fracture strain can be expressed by

$$\varepsilon_f = a \exp \left(-b \frac{\sigma_m}{\sigma_{eq}} \right) \quad (2.27)$$

where a and b are two model parameters. Rice and Tracey treated the void as an isolated sphere and their derivation does not include interaction between adjacent voids. Chae and Koss [51] compared they fractographic data with Rice and Tracey's model and found that the coefficient of $b = 1.5$ in

Eq. (2.27) is better replaced by 2.5, taking into account the void interaction.

Gurson-like model

The success of the Gurson like model is largely due to the introduction of the new yield function, which links the plasticity with the damage accumulation. This aspect will be further explored in Chapter 12.

Gurson obtained the pressure dependent yield function from an isolated cylindrical or spherical void in a continuum [16]. The void-containing solid is considered as a dilatant, pressure-sensitive elasto-plastic continuum. The yield function for spherical void in rigid-perfectly plastic body is

$$\Phi = \frac{\sigma_{\text{eq}}^2}{\sigma_M^2} + 2f \cosh \left\{ \frac{3\sigma_m}{2\sigma_M} \right\} - (1 + f^2) = 0, \quad (2.28)$$

where f is the void volume fraction, σ_M is the yield stress of the undamaged material (matrix), σ_{eq} and σ_m are the macroscopic von Mises equivalent stress and the mean stress, respectively. The matrix yield stress σ_M is a function of the equivalent plastic strain ε_p of the matrix material, which represents the strain hardening. By assuming associative flow rule, the plastic flow function is the same as the yield function. The macroscopic plastic strain ε_p is found through the normality rule

$$\dot{\varepsilon}_p = \dot{\lambda} \frac{\partial \Phi}{\partial \sigma} \quad (2.29)$$

where ε_p ¹ and σ are the macroscopic strain and stress tensor respectively and $(\dot{})$ denotes the time derivative. The matrix plastic strain is linked to the macroscopic strain by the equivalence of the rate the plastic work, i.e.

$$\dot{\varepsilon}_{pl} : \sigma = (1 - f) \sigma_M \dot{\varepsilon}_p \quad (2.30)$$

From Gurson's yield function, the complete loss of load carrying capacity occurs at $f = 1$, which is unrealistically larger than experimental observations. Tvergaard [48] introduced two more parameters q_1 and q_2 to resolve this situation. Moreover, Tvergaard [52] discussed some sort of quantification of the coalescence effect. Tvergaard and Needleman [49] introduced a void volume fraction function f^* to model the complete loss of load carrying capacity at a realistic level of the void volume fraction.

¹A boldfaced letter denotes a tensor and a normal letter denotes a scalar quantity.

At an early stage of deformation, the evolution of the void volume fraction is characterized by the nucleation of new voids and growth of existing voids, which can be characterized by

$$\dot{f} = (\dot{f})_{growth} + (\dot{f})_{nucleation} \quad (2.31)$$

where $(\dot{f})_{growth}$ and $(\dot{f})_{nucleation}$ represent the growth and nucleation of the voids. After the void volume fraction reaches a critical value f_c , the voids begin to coalesce, which accelerates the increase of void volume fraction. The void coalescence results in an additional term $(\dot{f})_{coalescence}$ in Eq. (2.31), which is quantified by a multiplication factor in the GTN model.

The void nucleation and coalescence are different from the void growth in that they are highly metallurgically dependent. Most commercial materials contains second phase particles and precipitates, for instance, MnS in HY-100 steel and sulphite in HSLA-100 steel [51].

An empirical approach to quantify the void nucleation and coalescence is to use the metallurgical graph to track the emergence of new voids and the merge of existing large voids.

At low temperature, the nucleation of voids is dominated by the plastic deformation [53]. In ductile metals, the void nucleation often occurs at non-deformable second-phase particles, such as oxides and carbides. The nucleation of voids can be considered in a strain based or a stress based fashion [53–56]. In homogenously voided solids, the void nucleation takes place over a narrow range of deformation. An analysis by Needleman and Rice [57] suggests the localization will occur at very early stages of deformation. However, due to the physical complexity of the microstructure and the inclusion, the void nucleation particles are not homogenous within the solids. Chu and Needleman consider strain controlled void nucleation in a statistical way [58]. A normal distribution of the nucleation with respect to the plastic strain of the matrix material is proposed as

$$(\dot{f})_{nucleation} = A_N \dot{\varepsilon}_p \quad (2.32)$$

where ε_p is the matrix plastic strain and

$$A_N = \frac{F_N}{s_N \sqrt{2\pi}} \exp \left\{ -\frac{1}{2} \left(\frac{\varepsilon_p - \varepsilon_N}{s_N} \right)^2 \right\} \quad (2.33)$$

where s_N and ε_N are the standard deviation and the mean value of the distribution of the plastic strain, F_N is the total void volume fraction that can be nucleated.

The matrix material is assumed to be plastically incompressible. The void growth rate is thus

$$(\dot{f})_{growth} = (1 - f)\dot{\varepsilon}_{kk}, \quad (2.34)$$

where ε_{kk} represents the plastic rate of volume change.

Despite of the success of the void-nucleation-growth-coalescence models in the prediction of fracture in some application, there are inherent drawbacks with this type of model:

(1) No void shearing mechanism is considered. The Gurson model failed to predict a simple shear test when $f_N < f_f$. The Gurson-like material model original was conceived and applied with high stress triaxiality, where pressure sensitivity dominates in the fracture phenomenon. The application of Gurson-like of model to low stress should be used with cautious.

(2) In the Gurson-like model, the mechanical damage is limited to void volume fraction. However, the damage accumulation is a more complicated process than the evolution of void volume fraction. For instance, a volumeless micro crack inherently creates damage to the body of solids by introducing loss of load carrying area.

(3) The material parameters are related to microscopic values. The actual distribution of void nucleation particles varies and is hard to measure. As a microscopic approach, the void size, shape, orientation and spacing have to be treated in a stochastic way. However, the distributions of such governing parameters are often unknown.

2.4.3 Continuum damage mechanics

The concept of continuum damage mechanics was firstly proposed by Kachanov [15] in the context of ductile creep. It was further developed by Rabotnov [59] and Lemaitre [10] etc. This line of research differs from the micro mechanical models in that the micro-mechanism of the growth of individual void and their interactions are “smeared” and depicted in a phenomenologically aggregative way. Macroscopic parameters and equations are used to describe the aggregative responses of the body of solids. Therefore, the constitutive and damage model of the material is based on the externally observed behavior of the material.

The continuum damage mechanics considers the material property is the combined results of the matrix material and the damage to take into account the micro defects. The damage can be quantified in many different ways. For instance, Kachanov defines the damage variables as a surface

density of intersections of micro cracks and cavities [60]. Lemaitre and Chaboche determined experimentally such damage for a light alloy [61]. Their results show an increasing tendency of damage accumulation.

The law of elasticity coupled with damage is

$$\boldsymbol{\sigma} = \mathbf{C}_0 \boldsymbol{\varepsilon}^e (1 - D), \quad (2.35)$$

where \mathbf{C}_0 is the undamaged, i.e. initial fourth order elasticity stiffness tensor.

Lemaitre uses the strain energy release rate [10]

$$-Y = \frac{\sigma_{\text{eq}}^2}{2E(1-D)^2} \left[\frac{2}{3}(1+\nu) + 3(1-2\nu) \left(\frac{\sigma_m}{\sigma_{\text{eq}}} \right)^2 \right], \quad (2.36)$$

The damage evolution law is defined by

$$\dot{D} = \frac{1}{1-D} \left(\frac{-Y}{r_l} \right)^{s_l} \dot{\varepsilon}_p, \quad \text{if } \varepsilon_p > \varepsilon_c \quad (2.37)$$

where r_l and s_l are material constants and ε_c is a strain threshold for damage accumulation.

The weakening is also introduced to conventional plasticity. For instance, Borvik *et al* [4] introduced a weakening factor to the strength equation of Johnson-Cook model.

$$\sigma_{\text{eq}} = (1 - \beta_b D) [A + B \varepsilon_p^n] \left[1 + C \ln \left(\frac{\dot{\varepsilon}_p}{\dot{\varepsilon}_0} \right) \right] \left[1 - \left(\frac{T - T_0}{T_{\text{melt}} - T_0} \right)^q \right], \quad (2.38)$$

where D is the same as the original Johnson-Cook damage model and β_b is a material constant.

2.5 Comparison of damage variables and fracture criteria

The objective of this thesis is to find a generic model for the damage evolution and the fracture prediction. Therefore, it is desired to survey the existing models on fracture prediction.

Besides the above mentioned damage models, other material fracture models are proposed that take accounts of the stress state effect. A few these failure criteria are listed in Table 2.2.

Table 2.2: Various cumulative-strain-damage fracture models.

No.	Criterion/model	Formula
(1)	Constant strain	$D = \frac{1}{\varepsilon_0} \int d\varepsilon_p$
(2)	McClintock, [17]	$D = \frac{1}{\varepsilon_0} \int \eta d\varepsilon_p$
(3)	Rice and Tracy, [19]	$D = \frac{1}{1.65 \varepsilon_0} \int \exp(1.5\eta) d\varepsilon_p$
(4)	Johnson and Cook, [3] ¹	$D = \int \frac{1}{D_1 + D_2 \exp(D_3 \eta)} d\varepsilon_p$
(5)	Chaouadi et al., [25]	$D = \int [1 + 3\alpha_c \eta \exp(1.5\eta)] d\varepsilon_p$
(6)	LeRoy et al., [23]	$D = \frac{1}{W_0} \int (\sigma_1 - \sigma_m) d\varepsilon_p$
(7)	Brozzo et al., [20]	$D = \frac{1}{\varepsilon_0} \int \frac{2\sigma_1}{3(\sigma_1 - \sigma_m)} d\varepsilon_p$
(8)	Cockcroft and Latham, [18]	$D = \frac{1}{\varepsilon_0} \int \frac{\sigma_1}{\sigma_{eq}} d\varepsilon_p$
(9)	Norris et al., [21]	$D = \frac{1}{\varepsilon_0} \int \frac{1}{1 + c_N P} d\varepsilon_p$
(10)	Wilkins et al., [22]	$D = \int \frac{[2 - \max(\frac{s_2}{s_1}, \frac{s_2}{s_3})]^\beta}{(1 + \alpha p)^\alpha} d\varepsilon_p$

In Table 2.2, ε_p is the equivalent plastic strain, σ_1 is the maximum principal stress, ε_f is the failure strain envelop and ε_0 is a constant reference value of the fracture strain. The readers are referred to the original work of various authors for definition of other parameters shown in Table 2.2.

The fracture criteria in Table 2.2 can be classified into five categories: (a) constant strain, which is a first order approximation; (b) stress triaxiality models, which are models (2)-(6); (c) maximum stress models, which are models (7)-(8); (d) pressure models, which is model (9); (e) pressure and Lode dependent model, which is model (10).

In general, the effective failure strain function ε_f is not azimuthally symmetric about the hydrostatic axis. In Table 2.2, none of the four stress triaxiality based models considers the azimuth angle in the octahedral plane. The joint effects of the hydrostatic pressure and the effective stress are not adequate to quantify the equivalent fracture strain. The deviatoric state has to be considered as will be shown more clearly in Chapter 6. LeRoy et al's model uses the maximum stress deviator as a weighting function. Therefore, the fracture loci on an octahedral plane are hexagonal and the effect of hydrostatic pressure is neglected. Brozzo's model and Cockcroft and Latham's model uses the ratio of the maximum stress to the maximum deviatoric stress or the effective stress, which yields a hexagonal cross-section on octahedral planes as well, but the effect of hydrostatic pressure is coupled in their models. Norris, et al. also neglect the effect of deviatoric state because only

¹The complete Johnson-Cook failure envelope includes also the strain rate and thermal effects, i.e. $\varepsilon_f = [D_1 + D_2 \exp(D_3 \zeta)] \left[1 + \left(\frac{\dot{\varepsilon}}{\dot{\varepsilon}_0}\right)^{D_4}\right] [1 + D_5 T^*]$. Only the stress state part is discussed herein.

the hydrostatic pressure is considered in the weighting function. The Wilkins model is different from the rest in that a so-called stress asymmetry parameter is used to characterize the Lode angle dependence.

The models listed in Table 2.2 show different Lode angle dependence. The fracture locus on an octahedral plane can be divided into three groups. For the stress triaxiality models and Norris's pressure model, the fracture loci are circles, which are the same shape as the von Mises yield locus. For the maximum stress models, the fracture loci are hexagon, which are the same shape as the Tresca locus. Wilkins *et al* [22] use a separate parameter, i.e. the stress asymmetry A , to quantify the Lode angle dependence. The fracture loci on an octahedral plane looks like a petal. These three types of Lode angle dependence are shown in Fig. 2.4.

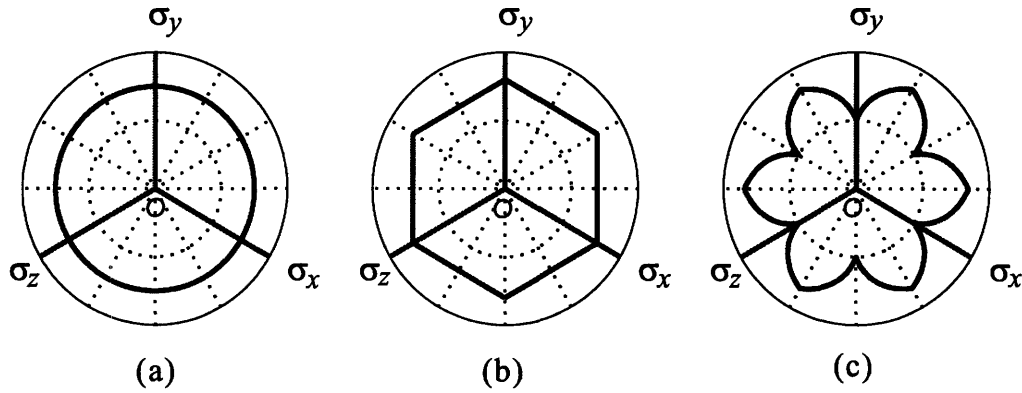


Figure 2.4: The Lode angle dependence of the existing cumulative-strain-damage fracture prediction models. (a) stress triaxiality models and Norris's model; (b) maximum stress models; (c) Wilkins model.

Experiments shows materials exhibit distinct differences in ductility under tensile and torsion/shear loading [2; 22; 26; 41–44]. These experiments suggest a strong Lode angle dependence of fracture strain for many materials. Therefore, the Lode angle dependence could be a major issue in developing a valid model for fracture prediction.

Material strength is another important issue. In many models, the material strength is considered independent of the damage accumulation. The fracture is simplified by a sudden loss of strength. This can be formally written as a jump function in the material strength function, i.e.

$$\sigma_{\text{eq}} = [1 - J(D)] \sigma_M, \quad (2.39)$$

where $J(D)$ is a jump function

$$J(D) = \begin{cases} 0, & 0 \leq D < 1; \\ 1, & 1 \leq D. \end{cases} \quad (2.40)$$

and σ_M is the matrix strength. In this case, the matrix strength is the same as the material strength in the classic plasticity theory.

Taking the derivative of Eq. (2.40) with respect to D , the deterioration rate is a Dirac delta function $\delta(D - 1)$. From Eq. (2.40), the material softening process is idealized to be a single spike at $D = 1$. This idealization is often too crude and leads to inaccurate fracture modes. The fractographic observation of the damage evolution shows the material deterioration is a much more complicated progressive process. A continuous weakening model is therefore desired.

Chapter 3

A New Damage Plasticity Model

3.1 Methodology and hypothesis

Material fracture is characterized by a complete loss of its load carrying capacity and deformability. At an intermediate damaged state, the remaining ductility of a deformed body can be described by the applied load and its loading history up to the present time. This remaining ductility should remain invariant when one changes his reference frame from one coordinate system to another.

The conventional continuum mechanics assumes the microstructure of the solid to be unchanged for moderate plasticity. The strength of material is often simplified as a one dimensional problem, in which the resistance is characterized as a function of the plastic strain. Undoubtedly, this simplification works well for many practical problems, especially for the design purpose of many structures carrying static load. However, for the extreme loading applications, the mechanical response of the material in the full range of its deformability is desired. In such conditions, the ignorance of the change of microstructure is an over-simplification. Some sort of damage has to be used to characterize the material deterioration.

Secondly, the damage accumulation along the loading path is a three-dimensional problem in that the pressure, the Lode angle and the equivalent stress level influence the damage rate in different ways. These effects will be discussed in this chapter and the next three chapters.

Hypothesis: *At a fixed pressure, for each proportional deviatoric loadings, the ductile damage processes are self-similar with respect to the ratio of the plastic strain and the fracture strain.*

From microscopic point of view, the existing defects may accelerate the damage process. For

many materials, such as poly-crystalline metals, in the moderate range of pressure and temperature, the damage is a monotonically increasing function if no recrystallization occurs. For ductile materials that are subjected to large scale plastic deformation, a robust fracture criterion has been a central point to predict the initiation of failure in crack-free bodies.

3.2 Mathematical aspects

3.2.1 Damage accumulation

Let us start to build a damage model from “*ground zero*”. A local approach is adopted - therefore, we are considering the stress and strain at a local material point. For generality, the damage can be describe as a second order tensor.

Assuming the damage to be *isotropic*, the damage can be quantified by a scalar D . We assume the damage rate can be described by

$$\dot{D} = \mathbf{A} : \dot{\boldsymbol{\sigma}}, \quad (3.1)$$

where \mathbf{A} is a second-order tensor, $\dot{\boldsymbol{\sigma}}$ denotes the objective rate of the Cauchy stress and “:” denotes the tensor operation of double contraction.

Furthermore, the damage should be *independent of observation frame*. Therefore, the stress state can be described by its principal vector $\underline{\sigma} = (\sigma_1, \sigma_2, \sigma_3)$ and the second-order tensor \mathbf{A} becomes a vector \underline{A} as well

$$\dot{D} = \underline{A} \cdot \underline{\dot{\sigma}}. \quad (3.2)$$

An identical representation of the vector $\underline{\sigma} = (\sigma_1, \sigma_2, \sigma_3)$ in the Cartesian principal stress space is $\underline{\sigma}^* = (p, \theta, \sigma_{\text{eq}})$ in the cylindrical coordinate system of the same 3-D space, where $p = -\frac{1}{3}\text{tr}(\boldsymbol{\sigma})$, θ is the azimuth angle on the octahedral plane and σ_{eq} is the equivalent stress. Without losing generality, Eq. (3.2) can be re-written as

$$\dot{D} = \underline{A}^* \cdot \underline{\dot{\sigma}}^*. \quad (3.3)$$

Let $\underline{A}^* = (a_1, a_2, a_3)$, where a_1, a_2 , and a_3 are scalars depending on the current stress and strain

states. Expanding Eq. (3.3), we have

$$\dot{D} = a_1\dot{p} + a_2\dot{\theta} + a_3\dot{\sigma}_{\text{eq}}. \quad (3.4)$$

From classic *J₂ flow theory*, we introduce von Mises type of yield surface and associated flow rule. Therefore, the plastic deformation does not depend on either p or θ . Assuming the *ductile damage rate is induced solely by plastic deformation rate*, one obtains $a_1 = a_2 = 0$ and

$$\dot{D} = a_3\dot{\sigma}_{\text{eq}}. \quad (3.5)$$

Given a hardening rule, Eq. (3.5) can be transformed into

$$\dot{D} = f\dot{\varepsilon}_{\text{p}}, \quad (3.6)$$

where $f = a_3h$ and h is the plastic hardening modulus.

Now, the task of quantifying the “damage” reduces to find a functional form of f in Eq. (3.6).

3.2.2 Normalization

We restrict ourselves to the *mechanical damage* and no *thermal, strain rate, chemical, radiational etc. effects* are considered. Hence, we assume *the function f is defined on the 3-D base of $(p, \theta, \sigma_{\text{eq}})$* .

Let us consider a special case of *fixed p and θ* and therefore σ_{eq} and ε_{p} can be one-to-one mapped. The evolution of damage becomes

$$\dot{D} = f(\varepsilon_{\text{p}})\dot{\varepsilon}_{\text{p}}, \quad (3.7)$$

and fracture occurs at $\varepsilon_{\text{p}} = \varepsilon_{\text{f}}$. The equivalent fracture strain ε_{f} depends on the *arbitrarily fixed p and θ* but it is independent of ε_{p} . Therefore, we can *normalize ε_{p} with respect to ε_{f}*

$$\dot{D} = f^* \left(\frac{\varepsilon_{\text{p}}}{\varepsilon_{\text{f}}} \right) \frac{\dot{\varepsilon}_{\text{p}}}{\varepsilon_{\text{f}}} \quad (3.8)$$

We assume $D = 0$ for undamaged material and the *fracture criterion is given by $D \geq D_{\text{cr}}$* , where D_{cr} is a material constant,

$$D_{\text{cr}} = \int_0^1 f^* \left(\frac{\varepsilon_{\text{p}}}{\varepsilon_{\text{f}}} \right) d \left(\frac{\varepsilon_{\text{p}}}{\varepsilon_{\text{f}}} \right), \quad (3.9)$$

However, there is still arbitrariness in Eq. (3.9), because the functional f^* is *scalable*, which means f^* and D_{cr} can be multiplied by any positive number and Eq. (3.9) remains satisfied. This arbitrariness is removed by *normalizing f^* with respect to D_{cr}* . The evolution law of damage is then

$$\dot{D} = g \left(\frac{\varepsilon_{\text{p}}}{\varepsilon_{\text{f}}} \right) \frac{\dot{\varepsilon}_{\text{p}}}{\varepsilon_{\text{f}}}, \quad (3.10)$$

where $g \left(\frac{\varepsilon_{\text{p}}}{\varepsilon_{\text{f}}} \right) = \frac{f^* \left(\frac{\varepsilon_{\text{p}}}{\varepsilon_{\text{f}}} \right)}{D_{\text{cr}}}$ and the *fracture criterion becomes $D \geq 1$* .

Equation (3.10) is referred as the damage evolution law and ε_{f} is a function of p and θ .

3.2.3 Separation of p and θ

It should be emphasized that ε_{f} is defined on p and θ and the functional of $\varepsilon_{\text{f}}(p, \theta)$ is yet to be determined. Since p and θ are orthogonal to each other, it may be wise to choose a *separable form* of these two variables, i.e.

$$\varepsilon_{\text{f}} = \varepsilon_{\text{f}0} \mu_p(p) \mu_\theta(\theta), \quad (3.11)$$

where $\varepsilon_{\text{f}0}$ is a reference value and the two functions μ_p and μ_θ characterize the effect of hydrostatic pressure and the azimuth angle. Equation (3.11) effectively defines the *fracture envelope* in a three dimensional space.

The separation of these two variables makes the calibration process tractable, i.e., you fix p or θ and obtain the dependence of the other, *independently and respectively*.

For constant failure strain criterion, both μ_p and μ_θ degenerate to unity.

The fracture surface shows the relevant extent of ductility for the deviatorically proportional loading path. However, the actual damage is an accrued effect of the loading history, which has to be described by a history variable. The evolution law of the damage can be summarized as

$$\dot{D} = g \left(\frac{\varepsilon_{\text{p}}}{\varepsilon_{\text{f}}} \right) \frac{\dot{\varepsilon}_{\text{p}}}{\varepsilon_{\text{f}}}, \quad (3.12)$$

where $\varepsilon_f = \varepsilon_{f0} \mu_p(p) \mu_\theta(\theta)$.

The above separation is referred to as the “cylindrical decomposition” hereafter.

3.3 A geometrical representation of damage accumulation

Let us recall the discussion of the principal stress space. Given an initial load condition, say represented by \vec{OA} in the principal stress space, and an arbitrary increment, \vec{AB} , from the initial state, the loading path is shown in the 3-D principal stress space. See Fig. 3.1.

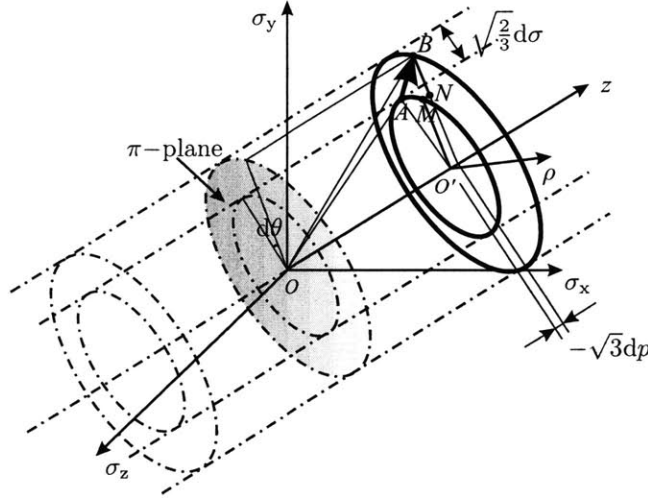


Figure 3.1: An arbitrary increment \vec{AB} in the principal stresses from an initial stress state represented by vector \vec{OA} .

Experiments also show that the damage is a cumulative process of the deformation. The fracture of material is loading path dependant. We assume the damage rate depends on the current stress and strain state of the material. Therefore, at an arbitrary stress state, the incremental damage can be written as

$$dD = f(\chi_0, \sigma_0, p_0) d\varepsilon_p \quad (3.13)$$

where χ_0 , σ_0 and p_0 are field variables of the current stress state. Equation (3.13) is referred to as the “damage rule” hereafter.

In general, the material damage is a function of the loading history. To make this problem

tractable, let us assume a limited class of the deviatorically proportional loading paths such that (1) the hydrostatic pressure goes to the level of the final value and followed by (2) the deviatoric stresses increase proportionally until fracture occurs. In the three dimensional principal stress space, this loading path can be visually represented by the vectors $\overrightarrow{OO'}$ and $\overrightarrow{O'A}$ in Fig. 2.1. Since any vector in the principal stress space can be uniquely decomposed into a combination of $\overrightarrow{OO'}$ and $\overrightarrow{O'A}$, the loading path is uniquely defined by the given stress state. Thus, a damage field could be defined in the three-dimensional principal stress space by using an evaluation function.

The fracture surface shows the relevant extent of ductility for the deviatorically proportional loading path. However, the actual loading path is not necessarily confined to the set of deviatorically proportional loading paths. The damage is an accrued effect of the loading history, which has to be described by a history variable.

3.3.1 History effect

There are infinitely many loading paths to a given stress state in the principal stress space. For example, let us consider three particular paths.

(a) A hydrostatic loading followed by a change in stress deviators. A hydrostatic pressure is superimposed first while the effective stress remains zero and then the principal stresses changes in a way that the deviatoric state remains the same. This loading path can be illustrated as vectors $\overrightarrow{OO'}$ plus $\overrightarrow{O'A}$ in Fig. 2.1.

(b) Proportional loading path. This is a straight line that the ratio of principal stresses is constant while the effective stress increases. This loading path can be illustrated as vector \overrightarrow{OA} .

(c) An increase in stress deviators followed by a hydrostatic loading. The principal stresses change in the constant pressure plane first and then a hydrostatic pressure is superimposed. This can be illustrated as vectors \overrightarrow{OQ} plus \overrightarrow{QA} in Fig 2.1.

As can be seen from the subsection 2.1, the damage associated with path (a) is only on \overrightarrow{OQ} , and the damage on path (c) is on $\overrightarrow{O'A}$. For path (b), the damage is cumulative all the way to the final state \overrightarrow{OA} . There is no change in the deviatoric state in all these three paths. Thus, the effective failure strain is defined by the hydrostatic pressure only. Since the mean stress level in path \overrightarrow{OQ} is less than in the path $\overrightarrow{O'A}$, the predicted damage is less with the loading path (a) than with the loading path (c). The loading path (b) results in an intermediate damage compared with

the other two paths. It should be noted that in the present model, the damage is assumed to be due to the plastic deformation alone. Under classical J_2 plasticity theory, the plastic deformation does not result from a hydrostatic increment.

3.4 Yield function and flow rule

It is generally accepted that the yielding is relatively independent of the superimposed hydrostatic pressure. For Mises type of material, the yielding locus resembles a cylindrical tube in the principal stress space. The Mises yield condition does not depend on the Lode parameter or the pressure.

With strain hardening, the size of the cylindrical tube expands to the current yield stress. In the classic plasticity theory, the yielding is simplified to be dependent only on the plastic strain and is independent of the loading path.

In the continuum damage mechanics, the yielding is a function of the current state of damage in addition to the plastic strain. In the present model, the concept of continuum damage mechanics is adopted. The yield function and the associated flow rule are coupled with the damage. The material deterioration is considered at a material volume level. Following the continuum damage mechanics, the constitutive equation of the damaged material can be derived from the modified yield potential function

$$\Phi = \sigma_{\text{eq}} - w(D)\sigma_M, \quad (3.14)$$

where w is a weakening function what characterizes the material deterioration, σ_M is the resistance of the matrix material and σ_{eq} is the applied stress on the damage material.

There are restrictions on the weakening function. Firstly, the initial yielding should not be changed since there is no damage up to the yield point. Secondly, the yield strength at full damage state is zero, which means the material can no longer carry any load further. Let D_s represent the fractional stiffness reduction of the material. The weakening function can be written as

$$w(D) = 1 - D_s. \quad (3.15)$$

Following the hypothesis of strain equivalence [61], the strain for a damaged material is represented by constitutive equations of the undamaged material in the potential of which the stress

is simply replaced by the effective stress. The material hardening is described by the hardening behavior of the matrix material, which is represented by the σ_M in Eq. (3.14); while the material weakening is represented by the multiplication factor of $(1 - D_s)$.

In general, the damage associated with the reduction of the effective load carrying area may not necessary the same as the damage that addresses the reduction of the ductility, i.e. $D_s \neq D$.

Chapter 4

Damage Rule and Material Weakening

4.1 On damage variables

We start by clarifying the definition of damage. Along the damaging process towards the ultimate fracture of the solids, the physical properties of the partially damaged material changes with the accumulation of the damage. Such physical properties include the elastic modulus, the remaining ductility, the local mass density, etc.

The word “damage” carries a meaning of *relativity*. We say something is damaged, when we mean that the current state of that something is inferior *compared* to its previous state. In this sense, the relative loss of deformability is obtained by comparing the deformability of the current state with the initial undamaged state. In the present study, the following definition is used.

Definition: *Damage is defined as the relative loss of ductility of the material.*

One way to think of the relative loss of ductility is considered the ductility decreases in a linear way along the plastic deformation path. Bridgman is probably the first to propose an incremental linear damage rule [2]. Johnson further extended this linear relationship to incremental plastic strain [46]. This linear damage rule has been used quite often in solving practical problems. However, the linear relationship of damage with respect to the plastic strain is questionable.

Using void volume fraction as a damage variable, Tvergaard and Needleman propose a bilinear relationship on the damage with the second phase to be faster than the first phase to incorporate

the phase of void coalescence [49].

4.1.1 Damage accumulation

The simplest form of damage potential is a linear function, i.e.

$$D = \frac{\varepsilon_p}{\varepsilon_f} \quad (4.1)$$

and, correspondingly, for the given ε_f the incremental damage is

$$dD = \frac{1}{\varepsilon_f} d\varepsilon_p \quad (4.2)$$

which is used by many researchers, e.g. [3]. However, the damage is not necessarily linear with respect to the equivalent plastic strain. For instance, Børvik, *et al.* [4] considered that there exists a threshold of plastic strain below which no damage is accumulated. There are other nonlinear forms of the damage potential such as in [62].

In the present theory, we adopted a deviatorically proportional loading path. Because the stress deviator increases proportionally, the Lode angle or the relative ratio of the principal deviatoric stress and the hydrostatic pressure remain constants. The fracture initiation problem is then reduced to determine when the integral of the incremental damage exceeds unity. The proposed deviatorically proportional loading path is a particular solution which has to be satisfied for the damage rule. This particular solution imposes to the problem in its integral form as

$$D = \int_0^{\varepsilon_c} f(\varepsilon_p, \varepsilon_f) d\varepsilon_p = 1, \quad (4.3)$$

where ε_c is the equivalent strain at fracture.

For virgin materials, it is intuitive to consider the damage at the initial state is “ $D = 0$ ”. The damage “ $D = 1$ ” indicates the material is fully damaged and the fracture initiates. The choice of the damage value at these initial and end conditions are somewhat arbitrary, but does not lose generality. The damage remains zero before yielding occurs, because the elastic deformation is considered fully recoverable.

For the deviatorically proportional loading path, the end condition is $D = 1$ at $\varepsilon_p = \varepsilon_f$, which denotes the fracture surface. There are infinitely many functions that satisfy the initial and end

condition of the damage potential, i.e. $D(0) = 0$ at $\varepsilon_p = 0$ and $D(1) = 0$ at $\varepsilon_p = \varepsilon_f$. A family of solutions can be represented by

$$D = \left(\frac{\varepsilon_p}{\varepsilon_f} \right)^m. \quad (4.4)$$

where m is the damage exponent. With $m = 1$, the damage rule degenerates to a linear damage function.

The macroscopic damage links to the microscopic defects, such as micro voids and micro cracks. Upon continuous plastic flow, the micro voids expands and the micro cracks propagates. When adjacent defects come closer enough, they interacts with each other. Such interaction is detrimental and exaggerates the damage rate. Therefore, the damage accumulation rate increases along the purely deviatoric proportional loading path. By assuming a linear damage rule, i.e. $m = 1$, the damage accumulation rate is constant. Thus, the interaction of micro defects are ignored.

To further explore the nonlinear damage rule, let us use Bridgman's test as an example.

4.2 Bridgman's test

One way to obtain material constant m is by changing the loading path. In the present section, this method is illustrated by using one of Bridgman's experiments.

Bridgman reported a stepwise experiment on a ductile steel [2, page 79]. He wrote

"The specimen was fractured in tension in the normal way at atmospheric pressure, ... it fractured with a cup-cone break with the same value for the ratio of the areas, 0.43. ... In the second experiment a specimen was pulled to a strain of 1.69 under 227,000 psi pressure. It was then removed from the pressure apparatus, machined in such a way as to reduce the value of a/R to nearly zero, and then reintroduced in the pressure apparatus and re-pulled to fracture at a pressure of 267,000 psi. The additional strain to fracture on the second pulling was 2.74, making the total strain at fracture 4.43."

Bridgman did not state explicitly which material he used for this experiment. However, a complete search from his list of experiment results shows that there is only one material has a ratio of the cross-sectional area at fracture of 0.43 at atmospheric pressure. This material is numbered 1-0 in his book. The experimental results for this material are reprinted in Table 4.1.

Table 4.1: Bridgman's experimental results. From [2].

Specimen	Confining pressure (psi)	Fracture strain ($\ln \frac{A_0}{A}$)	Fracture or not
1-0-1	176,000	2.71	not fracture
1-0-2	344,000	0.43	not fracture
1-0-3	40,000	1.35	fracture
1-0-4	298,000	4.33	fracture
1-0-5	Atmos.	0.91	fracture
1-0-6	404,000	2.04	not fracture
1-0-7	207,000	3.93	fracture
1-0-8	398,000	4.53	fracture
1-0-9	227,000	0.82	not fracture
1-0-10	140,000	3.01	fracture

From Table 4.1, the failure strains at higher confining pressures of 227,000 psi and 267,000 psi are estimated to be $\varepsilon_{f1} = 4.0$ and $\varepsilon_{f2} = 4.5$, respectively. The deviatoric state χ is constant 0 at the center of the round bar throughout the test.

Assuming a power law damage rule, the damage resulted from the first pulling step at a confining pressure of 227,000 psi is

$$D_1 = \int_0^{1.69} m \left(\frac{\varepsilon_p}{\varepsilon_{f1}} \right)^{m-1} \frac{d\varepsilon_p}{\varepsilon_{f1}} = \left(\frac{1.69}{4.0} \right)^m \quad (4.5)$$

and the damage from the second step at a confining pressure of 267,000 psi is

$$D_2 = \int_{1.69}^{1.69+2.74} m \left(\frac{\varepsilon_p}{\varepsilon_{f2}} \right)^{m-1} \frac{d\varepsilon_p}{\varepsilon_{f2}} = \left(\frac{1.69 + 2.74}{4.5} \right)^m - \left(\frac{1.69}{4.5} \right)^m \quad (4.6)$$

Knowing $D_1 + D_2 = 1$, the damage exponent m is solved to be 2.21 numerically.

It is found that m is greater than unity, which means the damage curve is concave toward the ordinate. Hence, the closer the deformation to the onset of fracture, the larger the weighting function is, which means more damage for the same amount of the equivalent plastic strain increment.

However, at the time Bridgman did this test, his thought the damage rule was linear as he suggested in [63] that “*for example, that the specimen is on which under normal atmospheric pressure would fracture at a natural strain of 1, and that we pull it to a strain of 2 under a pressure sufficiently high to raise the strain required to fracture at that pressure to 4. We now release pressure and tensile load and continue pulling at atmospheric pressure will now tolerate further strain before*

fracture, which will occur at a strain of perhaps 2.5.”

The above calculation is just an example. It is noted that the hydrostatic pressure is not constant throughout the experiment, therefore, the fracture strain $\varepsilon_f(p, \theta)$ is not constant on either of the loading steps. A stepwise loading path at constant hydrostatic pressures is illustrated in Fig. 4.1.

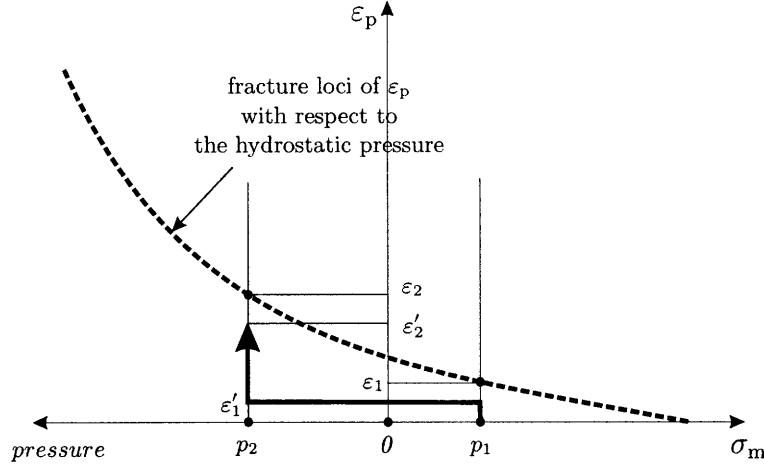


Figure 4.1: An illustrative sketch of a stepwise loading path in the $\varepsilon_p - \sigma_m$ plane.

Assuming the test is performed at constant χ , the material fractures at equivalent plastic strains of ε_1 and ε_2 at constant pressures p_1 and p_2 , respectively. A stepwise loading path is based on these two pressures, which is illustrated by a thick solid line in Fig. 4.1. The material is first loaded to an intermediate state of the equivalent plastic strain ε'_1 (which is less than ε_1 of course) at constant pressure p_1 and then changes the pressure to p_2 and continue to increase the loading until the material fractures. The total equivalent plastic strain is ε'_2 . Note, ε'_2 is not necessarily the same as ε_2 . Following the same procedure as shown in the Bridgman's example, the material constant m can be obtained. The pressure effect on this loading path is eliminated by presuming two constant pressure loading paths.

Due to the lack of experimental data, we assume the damage rate is proportional to the plastic strain, i.e. $m = 2.0$, or

$$\dot{D} = 2 \frac{\varepsilon^p \dot{\varepsilon}^p}{\varepsilon_f \dot{\varepsilon}_f}. \quad (4.7)$$

Further research in this regard should be desired to put the proposed theory in a more sound basis.

4.3 Material weakening

In continuum damage mechanics, the damage is one of the constitutive variables that takes into account the degradation and loss of load carrying capacity of materials. The material exhibits a weakening on the stiffness. For instance, the damage on the stiffness of 99.99% copper is measured, as shown in Fig. 4.2.

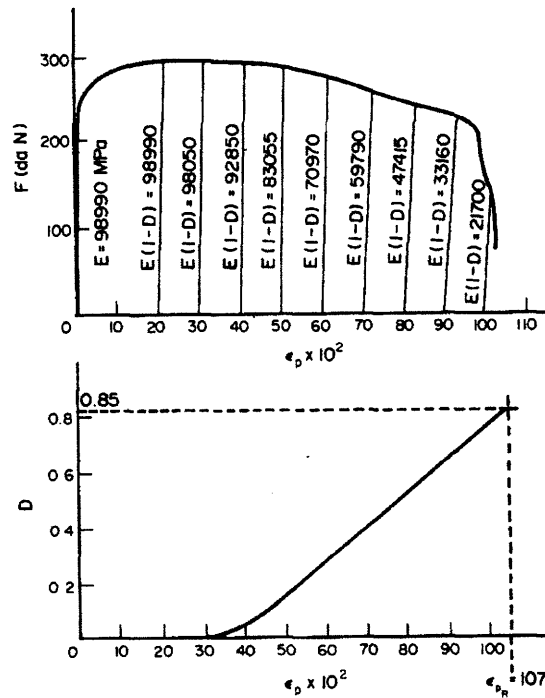


Figure 4.2: Evolution of the damage on the material stiffness of 99.99% copper. After Ref. [64].

Considering a unitary reference volume element, micro defects increase along with the plastic deformation within the body, as shown in Fig. 4.3. The effective load carrying area decrease as damage accumulates.

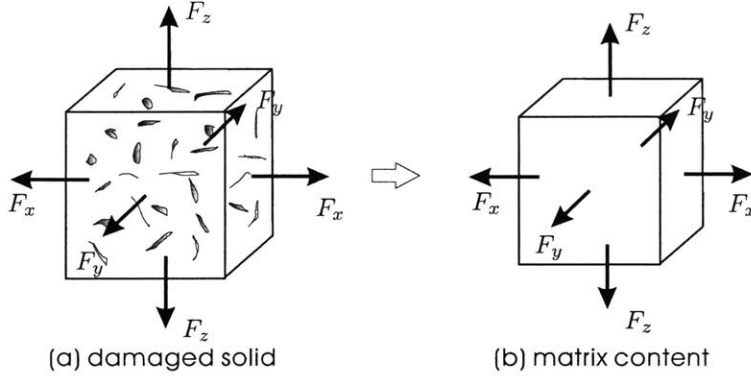


Figure 4.3: A schematic drawing of the damage containing solid and the matrix material.

The loss of the effective resisting area is used in continuum damage mechanics to describe the material deterioration. We define the loss of effective resisting area as

$$D_s = 1 - \frac{A_{\text{eff}}}{A_0}, \quad (4.8)$$

where A_0 is the nominal sectional area of the reference element and A_{eff} is the effective resisting area. The concept of A_{eff} is useful when considering the microstructural change of the solid in consideration, but it is difficult to measure from an experiment.

For a virgin material, we assume no defect exists and, therefore, $D_s = 0$. At a fully damage state, there is no resistance area, i.e. $A_{\text{eff}} = 0$ or $D_s = 1$. From the unrecoverable of plastic damage, the loss of effective resisting area is a monotonic function with respect to plastic deformation. Following the strain equivalence hypothesis [61], the material stiffness decrease at the same rate as the effective loading carrying area reduces.

Considering a plastically deformed unit cell, the macroscopic behavior of the solid is thus calculated from the matrix strength from the force balance of the unitary element, i.e.

$$\sigma_{\text{eq}} = \frac{A_{\text{eff}}}{A_0} \sigma_M, \quad (4.9)$$

where σ_M is the matrix property of the strength and σ_{eq} is the yield value of stress. Applying Eq. (4.8) into Eq. (4.9), the equivalent stress of the macroscopic solid is

$$\sigma_{\text{eq}} = (1 - D_s) \sigma_M. \quad (4.10)$$

One might consider the loss of resisting area follows the same law of the relative loss of deformability, i.e. $D_s = D$. However, the companion numerical simulation shows that a matrix stress is higher than commonly observed in order to show a realistic load displacement curve. This indicates the accumulation of stiffness damage lags the accumulation of ductile damage, i.e.

$$D_s \leq D. \quad (4.11)$$

To satisfy this requirement, an *ad hoc* parameter - the weakening exponent β is adopted. The stiffness damage is assumed to be a power law function of the ductile damage

$$D_s = D^\beta, \quad (4.12)$$

where β is a material constant. From Eq. (4.11), we find $\beta \geq 1$. The weakening function is then

$$w(D) = 1 - D^\beta. \quad (4.13)$$

It can be verified that Eq. (4.13) satisfies the two restriction conditions (1) $w(D) = 1$ when $D = 0$; and (2) $w(D) = 0$ when $D = 1$.

When $D \in [0, 1]$ and $\beta \geq 1$,

$$D_s \in [0, 1] \quad \text{and} \quad D_s \leq D. \quad (4.14)$$

Figure 4.4 illustrates a given damage function with $m = 2$ and three weakening functions with $\beta = 1$, $\beta = 2$ and $\beta = \infty$, respectively.

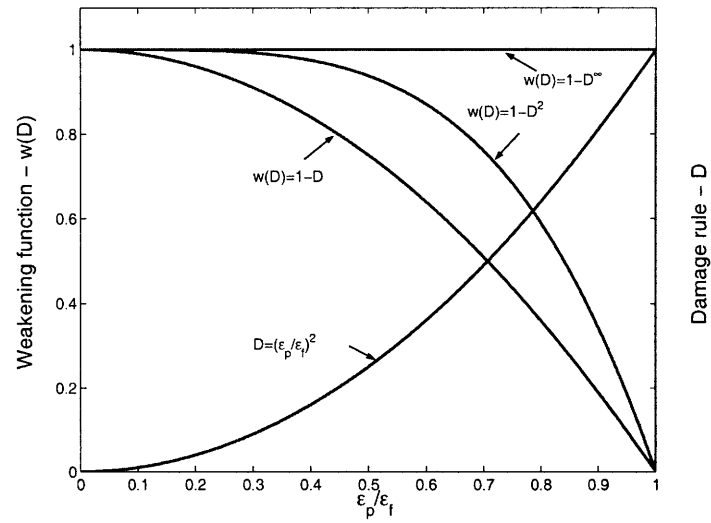


Figure 4.4: An illustrative sketch of a damage rule and three weakening function with different β .

Chapter 5

Hydrostatic pressure sensitivity

In Chapter 3, it is shown that the fracture envelope can be determined by the hydrostatic pressure p and the relative ratio of the principal deviatoric stresses χ . The fracture envelope is an idealized concept. A practical way of constructing the fracture envelope is to make use of existing knowledge on the pressure and the Lode angle effects. From the orthogonality of p and χ , it is conjectured that the effects of p and χ are independent of each other. Thus, the effects of p and χ are uncoupled and can be quantified separately.

Hypothesis: *The effects of the pressure and the Lode angle on the fracture envelope are independent of each other.*

5.1 Survey of previous experimental works

The ideal experimental condition is that the pressure and the Lode angle can be adjusted separately, such that two series of tests can be conducted at constant p and constant χ , respectively. Unfortunately, such test condition has not been achieved to date, except for several special cases, and is likely to be a future topic for experimentalists. So far, many of the modern experimental work on the pressure effect were conducted in a high pressure vessel, e.g. [2; 35; 65], due to the incompressibility and transmissibility of pressure of liquids. Other apparatus to achieve high pressure include die channel and opposing anvils.

The liquid pressure vessel can be used to obtain a constant ambient pressure, however, the pressure the fracture point (for instance, the center of the neck in a tensile round bar) varies along

the loading path in most cases. Although a constant pressure test is still in need, there are certain general points of view and expectations that are obtained from existing experimental work.

5.1.1 Flow and fracture

Materials become more ductile as they experience high compressive pressures. For some metals, the ductility can be an order of magnitude higher under high compressive pressure than its ductility at atmospheric pressure. For instance, zinc exhibits a sudden transition from brittle to ductile at a critical pressure about 70 MPa [66]. It is also observed that the flow strength increases slowly (2 percent per kilobar) in tension with increase pressure [2]. The same trend of strength increase with increase pressure is found for shear deformation as well [67]. Compared with the ductility increase, the increase of strength of metals appears to be insignificant. In the present thesis, the flow strength of material is considered to be independent of the hydrostatic pressure experienced.

5.1.2 Uniaxial tension under pressure

Perhaps the simplest test condition under high pressure is the uniaxial tension. One of the most comprehensive studies was carried out during the World War II by Bridgman [2] who tested the effect of hydrostatic pressure on the material fracture strain for several types of armor steels. Bridgman used round bars as specimen and pulled them in a pressure chamber. The round bar specimens are in a uniaxial tension condition superimposed by a hydrostatic pressure up to a compressive pressure of 30kbar. Because the two lateral principal stress components remain identical for the axisymmetric specimen, the ratio of the stress deviators remains zero at the center of the neck throughout his experiments. The ratio of the cross-sectional area at the neck at fracture to the initial cross-sectional area was found to decrease with respect to the lateral confining pressure. This increase in fracture strain was found for a number of armor steels. By using a sheath, Bridgman was also able to fracture commonly brittle materials, such as cast iron, NaCl, in a ductile way. For instance, cast iron was fractured at a strain of 1.77 at high confining pressure.

The same trend of monotonic increase in the failure strain with increasing hydrostatic pressure is confirmed by other researchers for several types of material, including carbon steel, aluminum, magnesium, zinc, cast iron, copper and rocks [29; 37–39; 68], etc.

Bridgman also pulled tensile specimens to a fixed strain at a variety of hydrostatic pressures and

determined the effect on the residual ductility from a further tensile test at atmospheric pressure. He found that the residual ductility increases with increasing hydrostatic pressure at the first place. This result indicates that higher hydrostatic pressure helps to reduce the damage associated with same amount of straining.

5.1.3 Unidirectional tension of notched round bar

Besides above mentioned experiments, superimposed hydrostatic tension reduces the ductility of the material. Similar to adding confining pressure on a round bar, the lateral tension can be added by create a circumferential notch around the circular bar. This is often seen in notched tensile specimens or pre-cracked specimens, e.g. [26; 69; 70] among many others.

5.1.4 Compression under pressure

Pugh investigated the effect of compressive pre-strain under pressure on the residual atmospheric compressive ductility of an 11% silicon aluminum alloy [71]. The material, which had a fracture compressive strain of 0.62 at atmospheric pressure can undergo a total compressive strain of 2.28 without fracture under 160,000 psi high pressure. Same material pre-strained to 0.62 in compression under high pressure still possessed a residual strain of 0.35.

One relevant situation of compression under pressure is the extrusion process under a back pressure [29; 65; 72; 73]. Pugh and his co-worker had shown that the material exhibits an enhanced ductility with the superimposed hydrostatic pressure. Improved quality products under hydrostatic extrusion were obtained for materials such as bismuth, magnesium and 60/40 brass that would otherwise have cracked or fragmented under atmospheric pressure extrusion, by inhibiting micro crack initiation and propagation. This property is used in many applications to form an enhanced quality products by carrying out the process in the presence of a high hydrostatic pressure. For instance, beryllium is brittle (1% elongation) in tension under atmospheric pressure at room temperature. At 704°C – 1120°C, beryllium cylinders, which become fully cracked at 50% of height reduction, can be upset-forged to a reduction of 85% height under press forging using a steel jacket without visible cracks [74]. Similar results was obtained by Cogan in upsetting tests [75].

5.1.5 Shear under pressure

Compared with tension, there are relatively less experiments were carried out in the shear/torsion loading condition. The main difficulties in a torsion test is the sealing problems. In fact, Bridgman conducted a double torsion test under combined axial compression rather than put the torsion specimen in the pressure chamber. Similar to the tension under pressure tests, Bridgman also found that fracture strain in torsion under axial compression increases with higher compressive stress [2]. However, because the combination of an axial compression and a torsion does not have a constant relative ratio of deviatoric stress, Bridgman's result is not conclusive.

5.1.6 Bending under pressure

Bobrowski et al [76] investigated the bending of tungsten and beryllium sheet at various hydrostatic pressures. They found that at about 3 GPa, these sheets do not display any cracking when the bending radius is the same as sheet thickness. This founding confirms the advantage in sheet metal forming under hydrostatic pressure.

5.2 Hydrostatic pressure effect

In this section, the relationship of the effective failure strain at fracture with respect to the hydrostatic pressure is determined from a particular load condition - the uniaxial tension under confined pressure.

5.2.1 Bridgman's work

Bridgman used 20 groups of steel of different chemical composition in his tensile tests under high compressive pressures. Each group may consist several different heat-treatment, which is identified by a second digit. Due to the nature of changing in the strength and ductility after heat-treatment, these material are considered to have different fracture behavior and their fracture parameters are calculated separately. Bridgman's results consists of tests of different number of fractured specimens for each material. The most detailed experiment was reported on material 9-2. Eleven specimens made of this material were pulled all the way until fracture. Material 9-2 is an SAE steel 1045 quenched into water from $1575^{\circ}F$ and drawn to $800^{\circ}F$. Its Rockwell C hardness is 40.3. The

complete experiments results are listed in Table 5.1.

Table 5.1: Test results of material 9-2, after Bridgman [2].

Material	Confining Pressure p_{conf} (MPa)	Final Flow Stress σ_{flow} (MPa)	Strain at Fracture ε_f	Remarks
9-2	0.100	1820.28	0.88	
	0.100	1778.91	0.89	
	772.240	2096.08	1.63	
	1434.160	2971.74	2.57	
	2640.785	3840.51	3.73	x ¹
	0.100	2027.13	0.85	
	896.350	2309.82	1.54	
	1192.835	3033.8	2.11	
	413.700	2185.72	1.28	
	1854.755	4054.26	2.98	
	1882.335	3495.76	2.76	

5.2.2 Pressure dependence

During the uniaxial tension under pressure tests, the hydrostatic pressure at the center of the neck does not maintain constant. In addition to the confining pressure, a tensile force is applied on the longitudinal direction. Bridgman defines the flow stress σ_{flow} as the difference between the stress in the longitudinal direction and the confining pressure [2], i.e.

$$\sigma_{\text{flow}} = \sigma_{\text{long}} - p_{\text{conf}}, \quad (5.1)$$

where σ_{long} is the true stress in the pulling direction and σ_{conf} is the confining pressure.

Bridgman showed that the ratio of the area of tensile fracture to initial area decrease with respect to the confining pressure, for instance, for a type of armor steel C14 [2] (p.79). By observation of the test results, the relationship of the fracture strain and the confining pressure can be expressed as

$$\frac{A_f}{A_0} = \frac{A_{f0}}{A_0} \cdot \left(1 - \frac{p_{\text{conf}}}{p_{\text{lim}}}\right)^{\bar{q}}, \quad (5.2)$$

where \bar{q} is a material constant that fits the experimental data best, A_0 is the original cross-sectional area, A_f is the cross-sectional area after fracture at the neck, A_{f0} is the cross-sectional area after

¹The 'x' mark indicates the data is not used in the curve fitting either because the strain is too high to measure the reduced cross-sectional area at the neck accurately or it is irregular, which suggest some sort of initial imperfections.

fracture at the neck at atmospheric pressure, and p_{lim} is a limiting pressure beyond which the material will not fail in the uniaxial tensile condition. Bridgman estimated this limiting pressure is between 1GPa to 2GPa for most of the steels (p.78 in Bridgman [2]).

Taking logarithm on both sides of Eq. (5.2), one gets

$$\varepsilon_f = \varepsilon_{f0} \left[1 - q \log \left(1 - \frac{p}{p_{\text{lim}}} \right) \right], \quad (5.3)$$

where ε_f is the fracture strain at the confining pressure p , $\varepsilon_{f0} = \log \frac{A_0}{A_{f0}}$ is the uniaxial tensile failure strain without confining pressure, and $q = \frac{\bar{q}}{\varepsilon_{f0}}$. Therefore, the pressure dependence function $\mu_p(p)$ becomes

$$\mu_p(p) = 1 - q \log \left(1 - \frac{p}{p_{\text{lim}}} \right). \quad (5.4)$$

There are yet two concerns about Eq. (5.4). Firstly, the confining pressure is not well defined in arbitrary triaxial loading condition. For numerical implementation, it is not feasible to use the confining pressure for triaxial loading cases. Therefore, the confining pressure is replaced by the hydrostatic pressure and the form of Eq. (5.4) is retained, except that the material constants are re-calibrated for the hydrostatic pressure.

The second concern is the hydrostatic pressure is not constant in the course of the Bridgman tests. Thus, an approximation method of averaging the hydrostatic pressure experienced at the center of the cross-section of the tensile specimen is used to calibrate the material parameters.

The average hydrostatic pressure experienced in the course of pulling is illustrated in Fig. 5.1. The equivalent stress path on the $\sigma_{\text{eq}}-p$ plane is shown as the thick solid line. The mean hydrostatic pressure along the entire loading path is estimated to be

$$p_{\text{ave}} = p_{\text{conf}} - \frac{\sigma_{\text{flow}}}{6}. \quad (5.5)$$

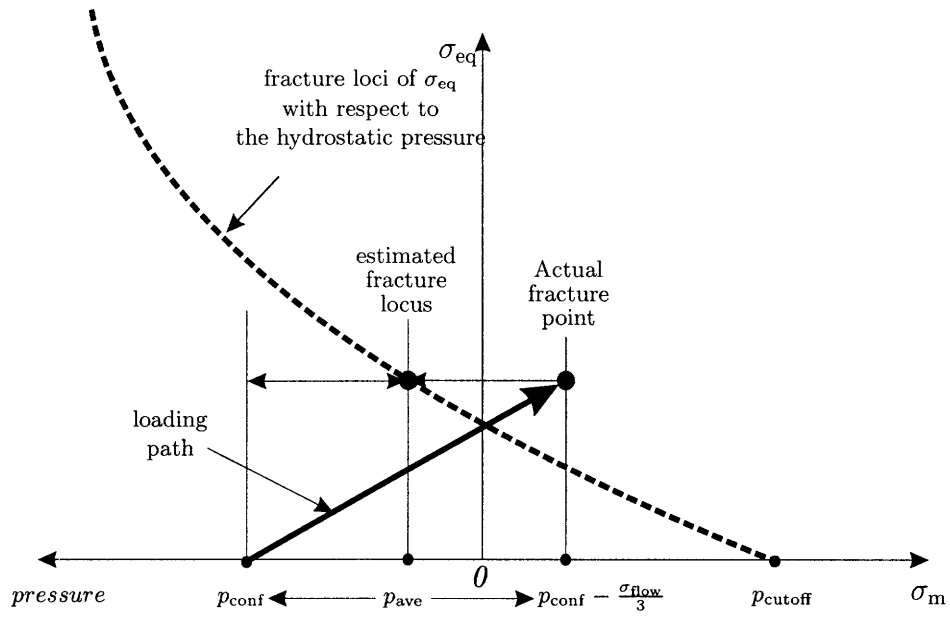


Figure 5.1: An illustrative sketch of the average hydrostatic pressure experienced in the course of uniaxial pulling under a confining pressure.

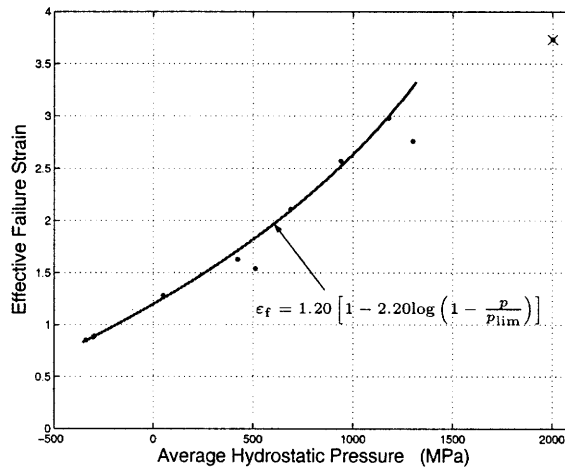


Figure 5.2: Curve fitting process for material 9-2.

From the curve fitting, the pressure dependence of material 9-2 can be obtained, i.e.

$$\epsilon_f = 1.20 \left[1 - 2.20 \log \left(1 - \frac{p}{p_{lim}} \right) \right]. \quad (5.6)$$

Because the limiting pressure of steel was not shown before, it is desired to analyze existing data

to gain ground. The complete list of Bridgman's more than 200 tests is analyzed using Eq. (5.4). The fitting results of the Bridgman's tests are plotted in Fig. 5.3.

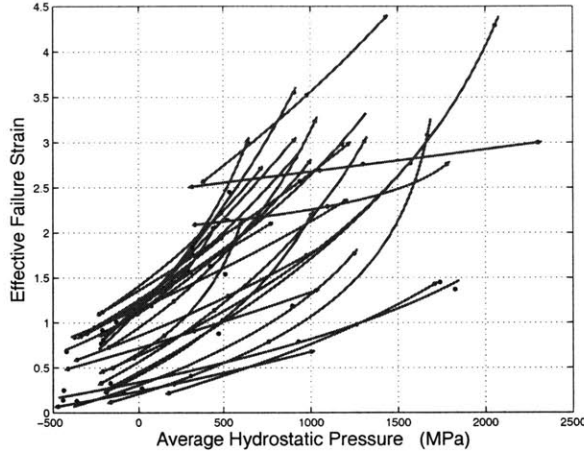


Figure 5.3: The complete fitting results of Bridgman's tests for various steels.

Several materials has only one or two specimens that actually failed, which is not adequate to determine the relationship of the effective failure strain with the hydrostatic pressure that has three unknowns. Such materials are eliminated from the list. Some materials Bridgman used only has three specimen that actually failed. Considering the experimental error, an accurate calibration of the parameters will be very difficult from these tests.

The nonlinearity becomes more significant for higher compressive pressure, meanwhile, the effective strain at failure is difficult to measure, since the cross-sectional area becomes too small. The limiting pressure is so high that under such pressure, an existing crack can actually heal. Ideally, the strain at failure goes to infinity as the hydrostatic pressure approaches p_{lim} . The hydrostatic pressure in Bridgman's experiments does not close to that end for steel yet. However, Pugh [29] showed that the limiting confining pressure is relatively low and approximately 100 MPa for zinc. On the other hand, except some extreme cases, practical applications seldom reaches such high a compressive pressure. In the moderate hydrostatic pressure range, the obtained logarithmic relation is sufficient.

The first order linear approximation of Eq. (5.3) around zero mean stress is

$$\varepsilon_f = \varepsilon_{f0} \left(1 - q \frac{p}{p_{lim}} \right). \quad (5.7)$$

Table 5.2: Material parameters to account for the effect of the hydrostatic pressure from Bridgman's tests, after Bridgman [2].

Material	ε_{f0}	p_{lim} (MPa)	q	p_{lim}/q (MPa)
1-0	1.187	997.034	1.500	664.651
2-0	1.142	1956.888	3.413	573.301
2-1	1.181	4623.534	7.172	644.703
2-2	0.947	1511.169	2.124	711.359
2-3	0.664	748.626	1.338	559.314
2-5	1.157	3958.698	2.868	1380.444
2-6	1.120	667.403	0.757	881.603
2-7	1.254	2250.069	2.240	1004.455
3-0	0.636	2576.346	3.589	717.750
4-0	0.417	1400.046	3.382	413.995
4-1	0.566	1963.306	3.936	498.862
4-2	0.451	2862.819	6.508	439.887
4-3	0.210	1782.756	4.967	358.910
4-5	0.308	1809.073	4.062	445.318
5-0-longitudinal	1.359	4686.106	3.978	1177.912
7-0-rolling	1.407	1763.820	1.782	989.781
9-2	1.198	2380.165	2.202	1080.896
9-3	1.107	1974.230	2.166	911.661
9-4	1.163	2935.974	3.874	757.924
9-6	1.224	13315.884	12.013	1108.425
10-1	0.125	3152.511	13.419	234.923
16-0	2.036	3935.411	2.548	1544.592
17-0	2.031	1985.858	0.159	12499.934
18-0	2.434	47705.864	4.702	10144.983
19-1	0.854	3326.874	3.014	1103.667
19-2	0.718	6214.388	4.926	1261.623
19-3	0.340	3017.921	3.500	862.304
19-4	0.240	3970.663	6.312	629.029

Admittedly, both q and p_{lim} are sensitive to the experimental error from limited data. However, from this linearized relationship of the effective failure strain and the hydrostatic pressure, it is understood that the value of $\frac{p_{\text{lim}}}{q}$ can be estimated with confidence even with three experimental data for the pressure level of many industrial applications. A precise measurement of the fracture strain at high compressive pressure has to be ensured, if the nonlinearity under high pressure is of interest.

From Eq. (5.3), a cut-off value of tensile pressure emerges. The failure strain is a monotonic decaying function with respect to increasing hydrostatic tension. It could be shown from Eq. (5.3) that the failure strain becomes negative when the hydrostatic pressure falls below

$$p_{\text{cutoff}} = p_{\text{lim}} \left[1 - e^{(1/q)} \right]. \quad (5.8)$$

At this cut-off pressure, the fracture strain ε_f is zero, which means effectively the material could not take any plastic strain further. This implies the volumetric deformation becomes dominant. On an octahedral plane of cut-off pressure, the fracture locus shrinks to a single point at the triad axis.

In reality, it is difficult to design a constant pressure test for calibration purpose. For instance, the torsion tests in a pressure chamber is a constant pressure test, but there are difficulties to construct such apparatus [2]. Using averaging method, the loading paths with different hydrostatic pressures can be estimated from tensile tests in a pressure chamber or from the notched round bar test etc.

5.2.3 Limiting pressure

Because of the limited range of pressure available in the compression chamber, accurate data relating to the limiting pressure of materials have not been measured, although there are some information from extrapolating existing data. It must be understood that, in the majority of cases, the pressure dependence parameters calibrated from laboratory tests are fairly good to describe phenomena in a similar pressure situation in a field test.

There are some experimental evidences that no damage occurs when the hydrostatic pressure is sufficiently high. In fact, when the hydrostatic pressure is above this critical value, new bond can actually be created at room temperature. For instance, it was discovered very early that soft

metals, such as gold, could be joined together by hammering at room temperature.

Unlike the fusion welding, the working temperature of the widely used solid phase welding is below the melting point. In this case, pressure is applied such that the materials can be welded.

One type of solid phase welding is the so-called “cold press welding”. Joints can be created from chemically identical materials or different metals that are otherwise hard to joint [77]. Similar technique is the “explosion welding”, where high pressure is produced by explosives [78]. Another application is the so-called “cold isostatic pressing” (or “hydrostatic pressing”) to consolidate metal powders [79]. For many years, powder metallurgists have been placing metal powders in a flexible container, and then immerse the container in a fluid and apply high pressure to create sound parts of various geometries. For instance, with standard grades of beryllium powder, with pressings at 60,000 psi or above, sufficient strength to allow detailed machining before further densification is obtained [80].

Chapter 6

Lode Angle Dependence of Ductile Fracture

6.1 Lode angle dependence

A Lode angle dependence function characterizes the azimuthal variation of the fracture locus on the strain plane. According to the hypothesis of damage accumulation and the hypothesis of independence of pressure and Lode angle on the damage potential function, the effect of the hydrostatic pressure and the deviatoric state on the fracture strain can be uncoupled and determined from separate series of experiments. Therefore, the Lode angle dependence function can be expressed as a function of the Lode angle (or other parameters of the same meaning). For isotropic materials, the components of principal stress are interchangeable to reflect the independence of damage to the observation frame. The weighting function for damage evolution should have symmetry in all three principal planes. This yields that on an octahedral plane, the azimuth angle can be divided into six part that have the same weighting function. Each sextant covers the complete range of the relative ratio of the stress deviators from zero to unity, i.e. $0 \leq \chi \leq 1$.

In many applications, the mean stress on the loading path is not constant. To eliminate the pressure effect, it is ideal to conduct a series of experiments that covers one sixth of the octahedral plane at a constant pressure. For instance, at the absence of hydrostatic pressure, all experiments are carried out on the π -plane with different Lode angle. Then, the Lode angle dependence can be obtained precisely.

Unfortunately, purely deviatoric experiments are not so easy to design even for a uniaxial tension of a round bar. Nevertheless, in the absence of precise knowledge of the relationship between the fracture strain and the Lode angle, we still can obtain some useful approximation from existing experimental evidence.

6.2 Experimental results relevant to Lode angle dependence

Because of the difficulty of designing a constant pressure experiment, we do not have a direct means to measure the Lode angle dependence using existing apparatus and methods. However, we are able to elucidate the existence and the general trend of fracture strain on the Lode angle from the experimental work in the literature.

In Chapter 5, we show that the fracture strain monotonically increases with respect to increasing hydrostatic pressure. The stress triaxiality ($\mathcal{T} = \sigma_m/\sigma_{eq}$) offers a convenient means to describe the pressure effect for proportional loadings, where the stress triaxiality keeps constant. For instance, for ideal uniaxial axisymmetric tension, $\mathcal{T} = 1/3$; for plane strain tension, $\mathcal{T} = 1/\sqrt{3}$ and for equi-biaxial tension, $\mathcal{T} = 2/3$.

The Lode angle characterizes the type of the loading condition. Many experimental investigation are carried out in proportional loading conditions or close to proportional loading. In these cases, the Lode angle keeps constant, but the pressure changes.

6.2.1 Comparison of simple tension and torsion/shear experiments

First, let us consider the simple tension and simple shear. Experiments shows materials exhibits different ductility under tensile and torsion/shear loading. McClintock [41] (page 97) collected a table of such data, which were expanded and listed in Table 6.1.

Table 6.1: Comparison of the fracture strain in simple tension and torsion.

No.	Material	References	Equivalent plastic strain	
			tension	torsion/shear
(1)	60-40 brass as-rolled	Halford and Morrow (1962) [42]	0.68	0.879
(2)	1100-0 aluminum annealed 660° F	Halford and Morrow (1962) [42]	2.62	12.6
(3)	2024-T351 aluminum alloy	Bao and Wierzbicki (2004) [26]	0.45	0.21
(4)	6061-T6 aluminum alloy	Wilkins et al. (1980) [22]	0.55-0.60	0.60
(5)	7075-T6 aluminum alloy	Halford and Morrow (1962) [42]	0.37	0.583
(6)	7075-T6 aluminum alloy	Neimark (1968) [43]	0.44	0.48
(7)	1045 steel 1575° F water Q temp. 800° F	Bridgman (1952, pp.260-262) [2]	0.88	0.39
(8)	1045 steel 1575° F salt Q temp. 800° F	Bridgman (1952, pp.260-262) [2]	0.93	0.38
(9)	1045 steel 1575° F salt Q temp. 1100° F	Bridgman (1952, pp.260-262) [2]	0.89	0.43
(10)	4340 steel 1575° F oil Q temp. 400° F	Halford and Morrow (1962) [42]	0.52	0.29
(11)	Weldox 460	Børvik et al (2001) [45]	1.6	1.8
(12)	A359 Al alloy	Li et al (2004) [44]	0.106	0.184
(13)	A359/SiC composite	Li et al (2004) [44]	0.035	0.061

Assuming these materials are isotropic, the difference between simple tension and torsion is that (1) in simple tension, a tensile hydrostatic pressure is superimposed and $\chi = 0$; (2) in torsion, the hydrostatic pressure disappears and $\chi = 0.5$. It follows from Table 6.1 that these two driving forces are entangled with each other and their joint effects show mixed result of the magnitude between the fracture strains of the two stress states.

6.2.2 Comparison of simple tension and transverse plane strain tension

Clausing published an experimental investigation of the difference of ductility in axisymmetric and plane strain tension [40]. He tested seven metals of different hardening properties. The

main finding is the significant decrease in tensile ductility of plane strain tension (grooved plate specimen) from the axisymmetric tension (round bar) for seven structural steels. Compared with pure shear or torsion, the uniaxial plane strain tension has an additional hydrostatic tensile pressure, which facilitate the void nucleation and growth and slip band movement. The difference of such hydrostatic pressure in axisymmetric and plain strain tension is far less significant than in the torsion and axisymmetric tension. Therefore, the difference in ductility between the plain strain tension and the axisymmetric tension is mainly due to the change in the relative ratio of the stress deviators, which is from $\chi = 0.5$ to $\chi = 0$. The plane strain tension test shows unanimous ductility decrease compared with the axisymmetric tensile tests, see Table 6.2.

Table 6.2: The difference in ductility of axisymmetric uniaxial tension and plain strain uniaxial tension. Experimental data from [40].

Steel	Yield Strength σ_y (MPa)	Tensile Strength σ_{uts} (MPa)	Fracture Strain ϵ_a (Axisymmetric)	Fracture Strain ϵ_{ps} (Plane Strain)
ABS-C	262.7	428.9	1.04	0.75
A302-B	371.0	590.2	0.98	0.72
HY-80	586.1	689.5	1.22	0.73
HY-130(T)	937.7	986.0	1.06	0.39
18Ni(180)	1227.3	1289.4	1.00	0.42
10Ni-Cr-Mo-Co	1254.9	1413.5	1.16	0.36
18Ni(250)	1710.0	1772.0	0.89	0.15

Hancock and Brown [81] repeated Clausen's experiment, but found less significant differences between the fracture strains in simple tension and a flat grooved plate tension. The length to height ratio of the groove used by Hancock and Brown was 1.0. In Clausen's experiments, the length to height ratio was 4.0. Adams conducted a series of tests on doubly grooved plates and suggested the length to height ratio need to be great than 10.0 to ensure a plane strain condition for grooved plate [82]. It is clear that Hancock and Brown's groove was too high and lost the plane strain constraint.

6.3 Lode angle dependence function

Due to the fact that the Lode angle dependence of ductile fracture is relatively unexplored, the exact shape of Lode angle dependence function is difficult to be calibrated. Without attempting to obtain a quantitatively accurate model, we emphasize the qualitative nature of this study. However, with appropriate hypotheses, reasonably good quality can be achieved from simple analysis of the experiment results. First, we make the following symmetric assumption to reduce the work load by half.

Hypothesis: *On an octahedral plane, the backward deformation of a material point creates the same amount of damage as the forward deformation does.*

From the deformation point of view, a backward deformation returns the shape of a solid body to its original shape at the same hydrostatic pressure it experiences in the forward deformation. For instance, the backward deformation of a simple tension is a compression state with lateral tension, as shown in Fig. 6.1. This is because the hydrostatic pressure during a simple tension is not the same as a simple compression. The backward deformation of a simple shear is a reversed simple shear. On an incremental basis, a deformed body under arbitrary forward loading path can be returned to the same shape of its original shape under the backward deformation of the forward deformation.

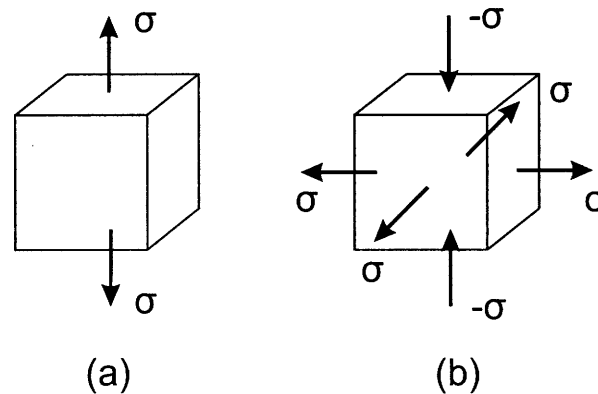


Figure 6.1: The stress state of a simple tension and the stress state of the backward deformation of simple tension.

The consequence of this hypothesis is that the fracture surface is symmetric with respect to the plane strain axes, where $\chi = 0.5$. In addition to the rotational symmetry with respect to the

principal stress axes, the Lode angle dependence function are identical for each of the twelve pie slices on the octahedral plane, which are identified by either $0 \leq \chi \leq 0.5$ or $0.5 < \chi \leq 1$.

Corollary: *The Lode angle dependence function is symmetric with respect to the plane strain axes ($\chi = 0.5$) and the principal stress axes ($\chi = 0$ or $\chi = 1$).*

Wilkins *et al* [22] proposed a functional for the Lode angle dependence function. Two new families of the Lode angle dependence function are proposed in the present thesis. One family is polygon that reduces to right hexagon for a given material constant. The other is a closed curved lines which reduces to a circle in the triaxial plastic strain plane for one particular set of parameters(the Lode angle dependence diminishes in this case). Only one additional parameter is needed for the first family and two parameters are required for the second family.

6.3.1 Wilkins, *et al*

Wilkins, *et al* [22] proposed a Lode angle dependent function

$$\mu_\theta = (2 - A)_{\beta_w}^\beta, \quad (6.1)$$

where β_w is a material constant and A is the stress state (“*stress asymmetry*”), i.e. $A = \max \left\{ \frac{s_2}{s_1}, \frac{s_2}{s_3} \right\}$.

It can be shown that the stress asymmetry and the ratio of the principal deviatoric stresses are related by

$$\chi = \begin{cases} 2 - \frac{3(A+1)}{A+2}, & s_2 \leq 0; \\ 2 - \frac{3}{2+A}, & s_2 > 0. \end{cases} \quad \text{or} \quad A = \begin{cases} \frac{1-2\chi}{1+\chi}, & 0 \leq \chi \leq \frac{1}{2}; \\ \frac{2\chi-1}{2-\chi}, & \frac{1}{2} \leq \chi \leq 1. \end{cases} \quad (6.2)$$

The Wilkins model predicts the ratio γ of the fracture strain at the plane strain condition to that at the generalized tension (or generalized compression) condition at the same constant hydrostatic pressure to be

$$\gamma = 2^{-\beta_w}. \quad (6.3)$$

The Lode angle dependence function Eq. (6.1) is plotted in Figs. 6.3 and 6.2 in a polar and a Cartesian coordinate system as dash-dot lines, respectively.

For a special case of $\gamma = 1$, the Wilkins parameter $\beta_w = 0$. In this case, the Lode angle

dependence of Wilkins model vanishes.

6.3.2 Polygon model - the first kind of Lode dependence function

Probably, the simplest Lode angle dependence model is to acknowledge the difference of the fracture strain between the generalized tension and plane strain on the triaxial strain plane. A first order linear relationship in the plane of strain components is proposed, as shown in Fig. 6.2. It is represented by a simplified shape of a “six point star” on the strain plane. The fracture point representing the fracture strain at the generalized tension or generalized compression is connected to that of the plane strain condition by a straight line and, thus, forms a polygon on the strain plane as shown in Fig. 6.2 (a solid line).

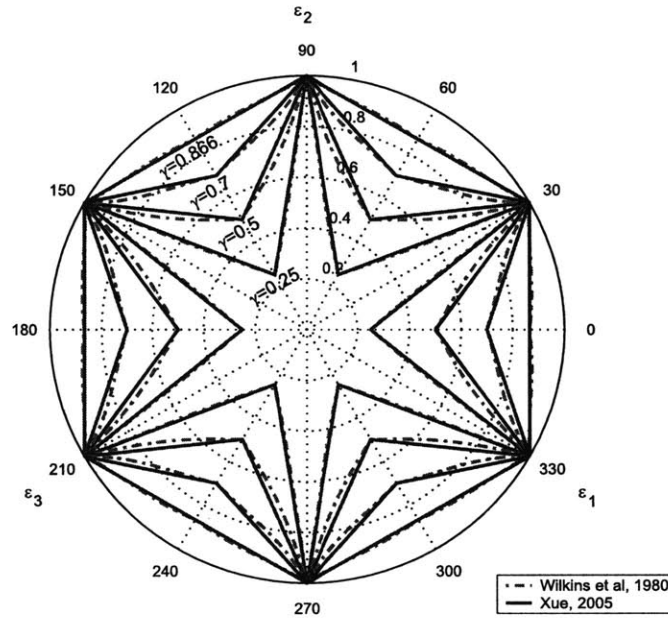


Figure 6.2: The Lode angle dependence of the effective fracture strain.

The polar equation for a straight line is

$$\mu_{\theta} = \frac{r_0}{\cos(\theta - \theta_0)}, \quad (6.4)$$

where r_0 represents the minimum distance between the origin and the straight line and θ_0 is the polar angle of the line perpendicular to the straight line. For the proposed “six-point star” polygon,

it can be shown that this straight line passes two points $(1, 0)$ and $(\gamma, \frac{\pi}{6})$ in the polar coordinate system. Substituting this two points in Eq. (6.4) to solve the two unknowns r_0 and θ_0 , we obtain

$$r_0 = \frac{\gamma}{2\sqrt{\gamma^2 - \sqrt{3}\gamma + 1}} \quad (6.5)$$

and

$$\theta_0 = \cos^{-1} \frac{\gamma}{2\sqrt{\gamma^2 - \sqrt{3}\gamma + 1}}. \quad (6.6)$$

Using the relative ratio of the stress deviators, the “six point star” can be represented by the function

$$\mu_\theta = \begin{cases} \frac{\sqrt{\chi^2 - \chi + 1}}{1 + \left(\frac{\sqrt{3}-2}{\gamma}\right)\chi}, & 0 \leq \chi \leq 0.5; \\ \frac{\sqrt{\chi^2 - \chi + 1}}{1 + \left(\frac{\sqrt{3}-2}{\gamma}\right)(1-\chi)}, & 0.5 < \chi \leq 1, \end{cases} \quad (6.7)$$

which is symmetric with respect to $\chi = 0.5$ as shown in Fig. 6.3.

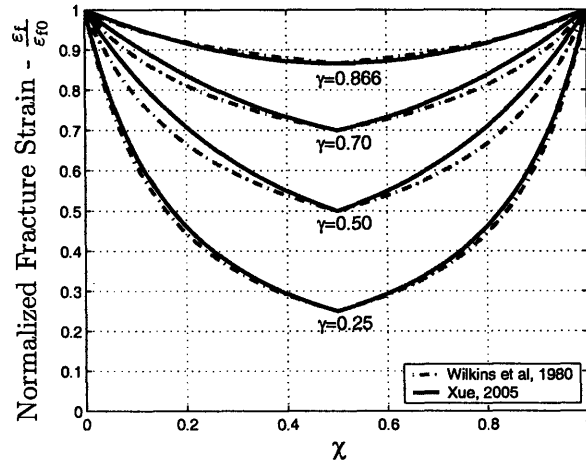


Figure 6.3: The normalized effective failure strain versus the ratio of the stress deviators.

It was found for many metals, the material parameter γ which characterizes the difference in ductility between generalized shear and generalized tension is less than unity. Consequently, fracture favors the shear mode. This partially answers the question of why shear lip forms at the edge of an otherwise tensile specimen. This will be further discussed in Chapter 11. Of course,

other reasons include the lack of stressing in the direction perpendicular to the surface and the geometrical change after deflection.

When $\gamma = \sqrt{3}/2$, the right “six-point star” degenerates to a right hexagon. It should be noted that the axes of the right hexagon is a measurement of strain. Although the shape of the right hexagon is the same as the maximum shear stress yield loci, the measurement is different.

6.3.3 Curvilinear model - the second kind of Lode dependence function

In a similar fashion of obtaining the linear Lode angle dependence function, we can also construct a curvilinear model that degenerates to a perfect circle which means the fracture strain does not dependent on the the Lode angle. For this second family of Lode dependence curves, the proposed curvilinear functionals are

$$\mu_{\theta} = \begin{cases} 1 - (1 - \gamma) \left(\frac{|\theta|}{\pi/6} \right)^k, & 0 \leq \theta < \pi/6; \\ 1 - (1 - \gamma) \left(\frac{|\pi/3 - \theta|}{\pi/6} \right)^k, & \pi/6 \leq \theta < \pi/3; \end{cases} \quad \text{or} \quad \mu_{\theta} = \gamma + (1 - \gamma) \left(\frac{|\theta_L|}{\pi/6} \right)^k; \quad (6.8)$$

where θ is the azimuth angle, θ_L is the Lode angle, $\gamma = \frac{\varepsilon_f(\theta=\pi/6)}{\varepsilon_f(\theta=0)}$ is the same material constant as in the polygon model and k is the Lode angle dependence exponent.

It can be verify that the boundary conditions of $(1, 0)$ and $(\gamma, \frac{\pi}{6})$ for ε_f, θ are satisfied. This is a family of Archimedean spiral. When $k = 1$ in Eq. (6.8), the curvilinear Lode angle dependence function is an Archimedes’ spiral in the polar coordinate system, which is linear with respect to the azimuth angle on the triaxial plastic strain plane. When $\gamma = 1$, the curvilinear function degenerates to a perfect circle.

Other nonlinear form may be obtained by fitting the experimental data. However, at the current stage, we will use the above proposed forms to calibrated our experimental data.

6.3.4 Combination of pressure and Lode effect

Let us consider the polygonal model for the purpose of consider the fracture surface in the 3D space.

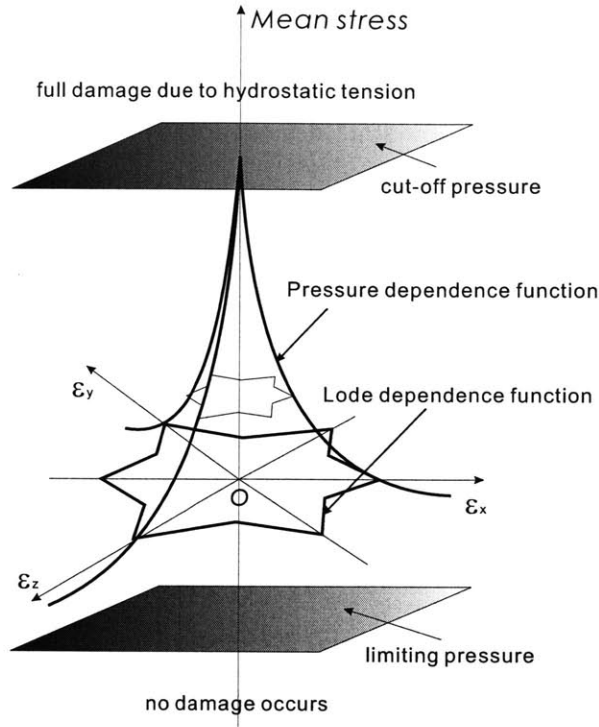


Figure 6.4: A three-dimensional fracture surface in the mean stress and plastic strain space.

Combining Eqs. (5.4) and (6.7), the fracture surface can be expressed by

$$\varepsilon_f = \begin{cases} \varepsilon_{f0} \left[1 - q \log \left(1 - \frac{p}{p_{lim}} \right) \right] \frac{\sqrt{\chi^2 - \chi + 1}}{1 + \left(\frac{\sqrt{3} - 2}{\gamma} \right) \chi}, & 0 \leq \chi \leq 0.5; \\ \varepsilon_{f0} \left[1 - q \log \left(1 - \frac{p}{p_{lim}} \right) \right] \frac{\sqrt{\chi^2 - \chi + 1}}{1 + \left(\frac{\sqrt{3} - 2}{\gamma} \right) (1 - \chi)}, & 0.5 < \chi \leq 1, \end{cases} \quad (6.9)$$

in which the fracture surface is characterized by four material constants ε_{f0} , γ , q and p_{lim} and two stress state parameters p and χ .

Expressing the fracture envelope in the principal stress space, the combined effects of the hydrostatic pressure and the deviatoric state is shown in Fig. 6.5, which appears to be a “*blossom*”.

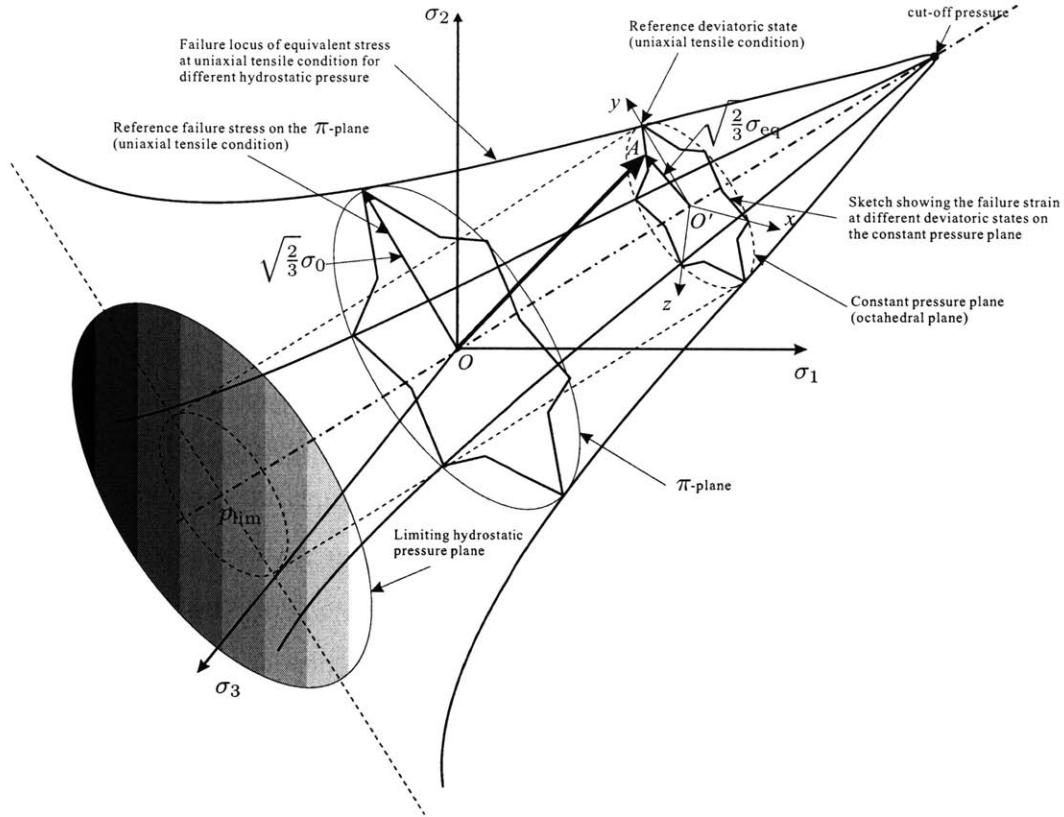


Figure 6.5: A three-dimensional sketch of the fracture surface in the principal stress space.

6.4 Hardening effect on the Lode angle dependence

It is interesting to explore what parameters influence the Lode dependence function, especially the strain ratio γ . One of such influencing factor is the strain hardening parameter. Such knowledge not only extends our physical understanding, but also is very helpful in designing a safe structure. For instance, knowing that a material has a possibly having low values of γ may prevent the engineers to use it in a shear condition, since it is more like to fail in shear.

A literature survey reveals that the experimental research in this area is scarce. More detailed research is in need in this regard. At this point, no quantitative conclusion is possible. However, it is still useful to extract some qualitative results from existing theoretical and experimental work.

6.4.1 Experimental results

(a) *Clausing's experiment [40]*

Clausing lists the yield stresses and the ultimate tensile strength for the seven materials he tested [40]. One measurement of the strain hardening is the ratio of the average hardening modulus to the yield stress. Low ratio means low strain hardening capacity and high ratio means higher strain hardening capability. The analyzed data are listed in Table 6.3. Without the exact knowledge of γ , we use the ratio of ε_{ps} (fracture strain at plane strain tension) and ε_{st} (fracture strain at simple tension) as a measurement of the sensitivity of the Lode angle dependence. The smaller the ratio, the higher sensitivity on Lode angle the material. The last two columns of Table 6.3 are plotted in Fig. 6.6. It is shown that the higher the strain hardening effect, the lower the Lode sensitivity is.

Table 6.3: The difference in ductility of axisymmetric uniaxial tension and plain strain uniaxial tension. Experimental data from [40].

Steel	Yield Strength σ_y (MPa)	Tensile Strength σ_{uts} (MPa)	Fracture Strain ε_{st} (Axisymmetric)	Fracture Strain ε_{ps} (Plain Strain)	$h_{ave} = \frac{\sigma_{uts} - \sigma_y}{\varepsilon_{st}}$	$\frac{h_{ave}}{\sigma_y}$	Fracture Strain Ratio ($\varepsilon_{ps}/\varepsilon_{st}$)
ABS-C	262.7	428.9	1.04	0.75	166.2	0.61	0.72
A302-B	371.0	590.2	0.98	0.72	219.3	0.60	0.73
HY-80	586.1	689.5	1.22	0.73	103.4	0.14	0.60
HY-130(T)	937.7	986.0	1.06	0.39	48.3	0.05	0.37
18Ni(180)	1227.3	1289.4	1.00	0.42	62.1	0.05	0.42
10Ni-Cr-Mo-Co	1254.9	1413.5	1.16	0.36	158.6	0.11	0.31
18Ni(250)	1710.0	1772.0	0.89	0.15	62.1	0.04	0.17

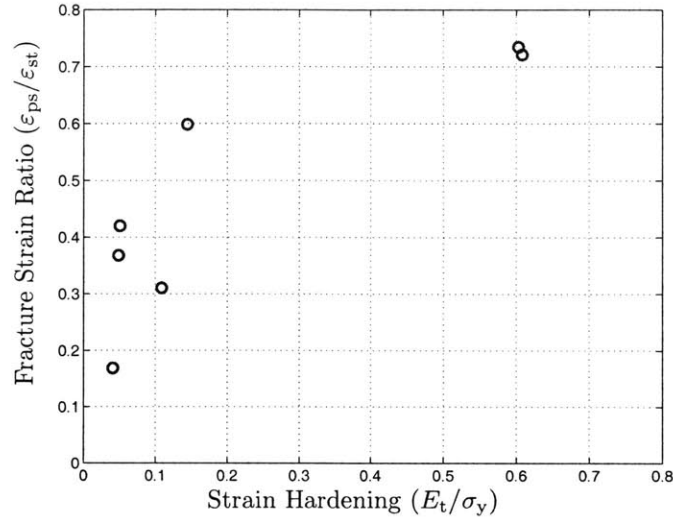


Figure 6.6: The ductility ratio of axisymmetric and plain strain tension versus the strain hardening.

It is also found from Table 6.3 and Fig. 6.6 that the decrease in ductility increases qualitatively with weaker strain hardening (lower h_{ave}/σ_y).

(b) *Johnson-Cook's tests* [3]

Neglecting the thermal and strain rate effects, the simplified Johnson-Cook strength model reduces to

$$\sigma_{eq} = A + B\varepsilon_p^n \quad (6.10)$$

Larger B/A and n indicate higher strain hardening capability. For the three material Johnson and Cook [3] and Borvik [4] tested, the following material constants were found.

Table 6.4: The material parameters and fracture strain. After [3] and [4].

Materials	A (MPa)	B (MPa)	n	B/A	ε_{st}	ε_{tor}	$\varepsilon_{tor}/\varepsilon_{st}$
OFHC copper [3]	90	292	0.31	3.24	1.5	5.0	3.3
ARMCO steel [3]	175	380	0.32	2.17	1.82	3.0	1.6
4340 steel [3]	792	510	0.26	0.64	1.1	0.2	0.18
Weldox 460 [4]	490	383	0.45	0.78	1.6	1.8	1.1

From Table 6.4, the higher B/A and n results in a higher $\varepsilon_{tor}/\varepsilon_{st}$ value, which means low Lode

angle sensitivity. Therefore, stronger strain hardening capability shows lower γ value.

(c) *heat treatment*

In Table 6.1, we compared simple tension and simple shear. Let us review these data again from the strain hardening point of view.

It is known that materials exhibit different hardening behavior after heat treatment. Annealing brings the initial yield stress lower and thus a larger hardening exponent n could be found by fitting the stress-strain curve using a power law function. On the other hand, quench lifts the material yield stress and therefore, a low hardening exponent is found comparing with the original material before quench. It can be found in table 6.1 that the only annealed material exhibits the largest difference of fracture strain in simple tension and torsion (1100-O aluminum annealed $660^\circ F$). In this case, pressure effects dominates. It is also found that the quenched steels tested by Bridgman show monotonic drop in fracture strain in shear, which suggests Lode dependence is predominant.

(d) *others*

There are also other experimental evidences that are related to the Lode angle dependence with respect to the hardening properties. Additional information can be obtained from the compact tension tests. Two competing fracture modes co-exist in a compact tension crack - (a) a flat crack and (b) a 45° shear crack. The generally observed experimental results are the higher strain hardening capability shows a flat crack and a low strain hardening capability material exhibits a shear crack [83]. This also indicates that that the increasing of material hardening capability reduces the Lode angle sensitivity of fracture strain.

6.4.2 Stören and Rice's bifurcation condition

When there is a point vertex in the yield surface, the derivative of the yield surface is non-continuous. Therefore, a bifurcation condition occurs [84]. Stören and Rice [85] predicted that the bifurcation condition under biaxial stretching from the tangential modulus and the secant modulus on the material hardening function.

It is generally considered that the onset of necking and fracture are two different phenomenon. However, there are some similarities that can be found through comparison.

For a power law strain hardening material, Stören and Rice [85] predicts the bifurcation occurs at

$$\varepsilon_b = \frac{(2\alpha - 1)^2 + 3n}{3\sqrt{\alpha^2 - \alpha + 1}}. \quad (6.11)$$

where α is the ratio of the two principal in-plane stress components and ε_b is the bifurcation strain. In their derivation, the hydrostatic pressure effect is not taken into account. Because superimposing an arbitrary hydrostatic pressure to the stress system does not alter the derivation, the bifurcation condition can be re-written for a 3D stress system using the relative ratio of the principal deviatoric stresses, i.e.

$$\varepsilon_b = \frac{(2\chi - 1)^2 + 3n}{3\sqrt{\chi^2 - \chi + 1}}. \quad (6.12)$$

In fact, Pugh showed experimentally and theoretically that the presence of the hydrostatic pressure component does not affect the onset of necking earlier [71].

Let us assume that for different azimuth angles, the ratio of the bifurcation strain to the ultimate fracture strain is constant. It can be inferred from Eq. (6.12) that the strain hardening postpones the bifurcation of the material for any possible χ . It is also interesting to compare the most disadvantageous deviatoric condition ($\chi = 0.5$) to the most advantageous deviatoric condition ($\chi = 0$ and $\chi = 1$). At $\chi = 0.5$, ε_b reaches the maximum value of $\varepsilon_b = n + \frac{1}{3}$. At $\chi = 0$ or 1 , ε_b reaches its minimum value of $\varepsilon_b = \frac{2}{\sqrt{3}}n$. Let γ_b denote the ratio of ε_b at $\chi = 0.5$ and $\chi = 0$ or 1 . From Eq. (6.12), it can be shown that

$$\gamma_b = \frac{\varepsilon_b(\chi = 0.5)}{\varepsilon_b(\chi = 0 \text{ or } 1)} = \frac{\frac{2}{\sqrt{3}}n}{n + \frac{1}{3}}. \quad (6.13)$$

Letting the Stören and Rice model and the Wilkins model predict the same behavior at these two extreme conditions by comparing Eq. (6.13) and Eq. (6.3), the stress asymmetry exponent in Wilkins model β_w is

$$\beta_w = \log_2 \left(\frac{n + \frac{1}{3}}{\frac{2}{\sqrt{3}}n} \right). \quad (6.14)$$

The normalized effective failure strain with respect to the failure strain subjected to the triaxial tensile loading at a strain plane is plotted in Fig. 6.7.

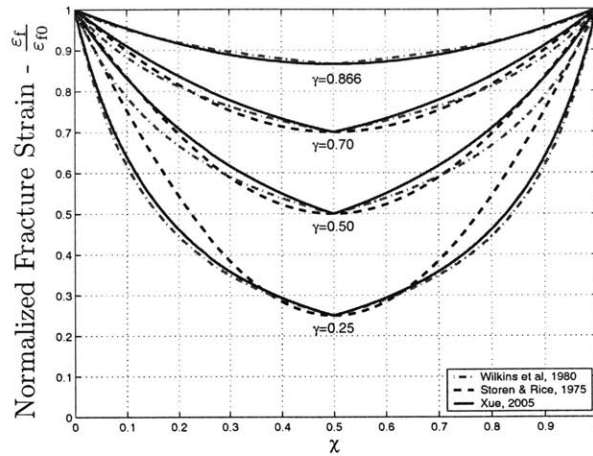


Figure 6.7: The normalized effective failure strain versus the ratio of the stress deviators.

The Stören and Rice model, the Lode angle dependence function of Wilkins model and the present polygon model are plotted in Fig. 6.8.

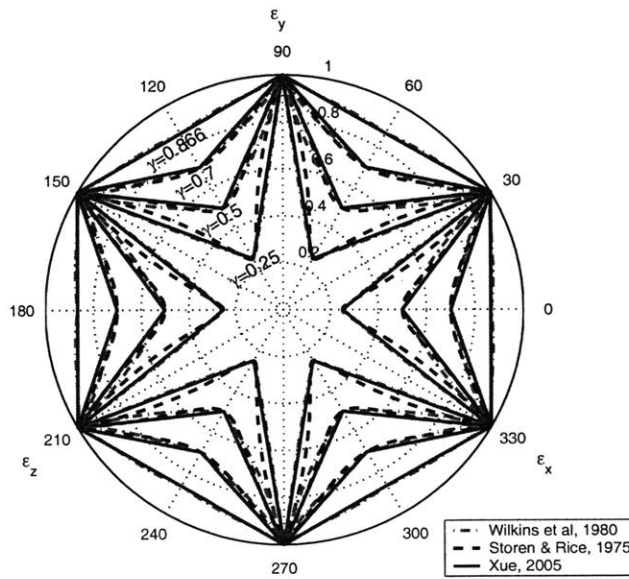


Figure 6.8: The normalized effective failure strain versus the deviatoric state.

The strain hardening exponents for the representative curves are listed in Table 6.5.

Table 6.5: The strain hardening exponents n versus strain ratio γ_b or γ .

γ_b or γ	n
0.866	1.000
0.700	0.513
0.500	0.255
0.250	0.092

Chapter 7

Summary on Damage Plasticity Model and Plane Stress Condition

7.1 Summary on damage plasticity model

The backbone of the present theory lies on the fundamental hypothesis that *“At a fixed pressure, for each proportional deviatoric loadings, the ductile damage processes are self-similar with respect to the ratio of the plastic strain and the fracture strain.”*

In particular, we proposed a set of equations to describe the damaging process and the associated material weakening effect. The ultimate goal is to provide an effective tool in modeling ductile materials. It should be noted, the chosen of dependence function are not necessarily precise for all ductile materials due to the complexity of their composition and micro structure. In the present study, the particular equations and the parameters are chosen based on the generally perceived wisdom. In summary, this set of equations can be listed as the following

$$\left\{ \begin{array}{l} \sigma_M = \hat{\sigma}_M(\varepsilon_p); \\ \sigma_{\text{eq}} = (1 - D^\beta) \sigma_M; \\ \dot{D} = m \left(\frac{\varepsilon_p}{\varepsilon_f} \right)^{(m-1)} \frac{\dot{\varepsilon}_p}{\varepsilon_f}; \\ \varepsilon_f = \varepsilon_{f0} \mu_p(p) \mu_\theta(\theta); \\ \mu_p(p) = 1 - q \log \left(1 - \frac{p}{p_{\text{lim}}} \right); \\ \text{and} \\ \mu_\theta(\theta) = 1 - (1 - \gamma) \left(\frac{|\theta_L|}{\pi/6} \right)^k. \end{array} \right. \quad (7.1)$$

where $\hat{\sigma}_M(\varepsilon_p)$ is the intrinsic matrix stress-strain property, σ_{eq} is the yield value of equivalent stress, $(1 - D^\beta)$ is the weakening function, \dot{D} is the damage rate, μ_p and μ_θ are the pressure and Lode angle dependence function respectively. The material parameters are the damage exponent m , the weakening exponent β , the shape parameter q and the limiting pressure p_{lim} in the pressure dependence function and the fracture strain ratio γ and the Lode angle dependence exponent k for instance.

Due to the incomplete of study on the Lode angle dependence function, in the present study, the Lode angle dependence exponent k in the second kind of Lode angle dependence function is assume to be unity. Further study on the shape of the Lode angle dependence function is in need to calibrate k .

In the present damage plasticity theory, two internal variables are used, namely ε_p and D . Both of the variables are scalars. We now compare the plasticity with the damage evolution in Table 7.1. To show the similarity, the stress-strain curve for the matrix material are assumed to follow a ‘‘Swift’’ type power law rule:

$$\sigma_M = \sigma_y \left(1 + \frac{\varepsilon_p}{\varepsilon_k} \right)^n, \quad (7.2)$$

where σ_y is the yield stress, ε_k is a reference strain and n is the hardening exponent.

A generalized damage plasticity model

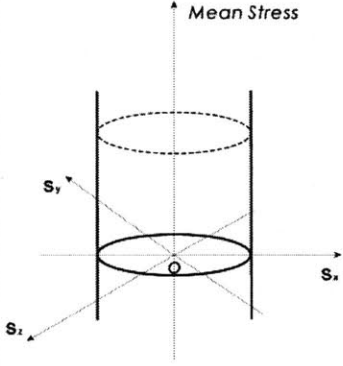
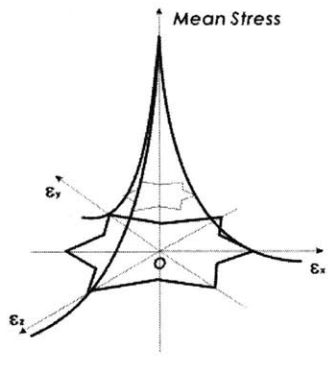
	Plasticity / Yielding	Damage coupled yield condition	Damage / Fracture
Constant value	σ_{y0} (1)	$\Phi\left(\frac{\sigma_{eq}}{\sigma_M}, D\right) = 0$ <p style="text-align: center;">(11)</p>	ε_{f0} (6)
Pressure dependence	$f_p = 1$ (2)		$\mu_p = 1 - q \log\left(1 - \frac{P}{P_{lim}}\right)$ (7)
Azimuthal dependence	$f_\theta = 1$ (3)		$\mu_\theta = \gamma + (1 - \gamma) \left(\frac{ \theta_L }{\pi/6}\right)^k$ (8)
Yield surface / Fracture envelope	 <p style="text-align: center;">$\sigma_y = \sigma_{y0} f_p f_\theta$ (4)</p>	 <p style="text-align: center;">$\varepsilon_f = \varepsilon_{f0} \mu_p \mu_\theta$ (9)</p>	
Evolution law	$\frac{d\sigma_M}{\sigma_y} = n \left(1 + \frac{\varepsilon_p}{\varepsilon_k}\right)^{(n-1)} \frac{d\varepsilon_p}{\varepsilon_k}$ (5)	$\frac{dD}{1} = m \left(\frac{\varepsilon_p}{\varepsilon_f}\right)^{(m-1)} \frac{d\varepsilon_p}{\varepsilon_f}$ (10)	

Figure 7.1: The comparison of yielding and plasticity to fracture and damage evolution.

The complete damage plasticity theory reduces to a total of nine (9) equations and two (2) parameters (σ_y and ε_{f0}). The similarity and difference between yielding and fracture are shown in Fig. 7.1. On the left hand side of Fig. 7.1, we choose von Mises type yield condition where the pressure dependence function and the azimuthal dependence function are both reduce to unity. On

the right hand side, fracture initiation for ductile materials are both pressure sensitive and Lode angle dependence in general. Therefore, non-unitary functions are given. We intentionally put “1” at denominator of left hand side of Eq. (10) in Fig. 7.1 to compare with σ_y in Eq. (5) and to emphasize that the damage value is chosen as “1” for completely damage material.

7.2 Fracture under plane stress condition

In the previous chapters, focuses are given to the constant pressure and constant Lode angle plastic loading paths. However, as already mentioned, this condition hardly represents any working condition in the real world. Therefore, in this section, we discuss one set of particular loading situations where one principal stress component is constant and equal to zero and the other two stress components are proportional. Thus, the pressure changes but the Lode angle remains constant - which is called the plane stress condition.

The plane stress condition $\sigma_{zz} = 0$ offers a subset of special problems that have been extensively studied experimentally, analytically and numerically.

A common application of plane stress condition is the sheet metal forming, where the majority of tests are conducted under the biaxial stretching because sheet metals are likely to exhibit out-of-plane wrinkle or buckling under compressive loadings. In thick plates, the out-of-plane mode is prohibited and the material tends to fail in shear when one principal compressive stress is significantly larger than the other.

In many of the applications, the in-plane loadings are proportional or nearly proportional. Therefore, it is reasonable to restrict ourselves in the scope of proportional loading in this chapter for simplicity. By proportionality, the Lode angle remains the same along the loading history.

For plane stress loading, the relative ratio of the principal deviatoric stresses can be transformed to the ratio of the two nonzero in-plane principal stresses α , i.e.

$$\alpha = \begin{cases} 1 - \chi, & \sigma_1 \leq \sigma_2 \leq 0 \\ \frac{\chi-1}{\chi}, & \sigma_1 \leq 0 \leq \sigma_2 \\ \chi, & 0 \leq \sigma_1 \leq \sigma_2 \end{cases} \quad (7.3)$$

The range of the stress ratio, the relative ratio of the stress deviators and the stress triaxiality are illustrated in the top-left half plane. The bottom-right half plane is symmetric with respect to

the line identified by $\sigma_x = \sigma_y$.

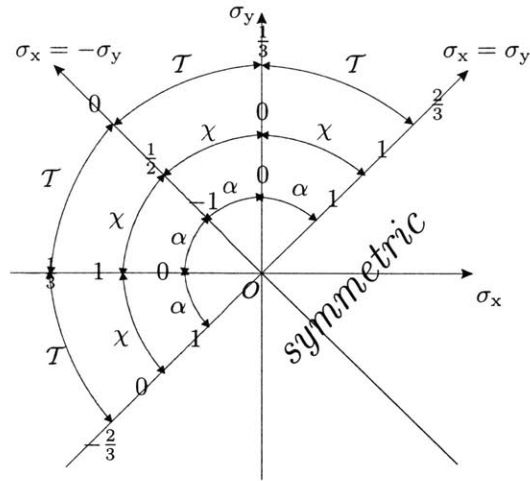


Figure 7.2: The stress ratio, the relative ratio of the stress deviators and the stress triaxiality in the plane stress condition.

For fracture under plane stress proportional loadings, the effective failure strain can be equally expressed in one of the three parameters. For example, the equivalent failure strain is plotted versus the stress triaxiality in Fig. 7.3 for 2024-T351 aluminum alloy.

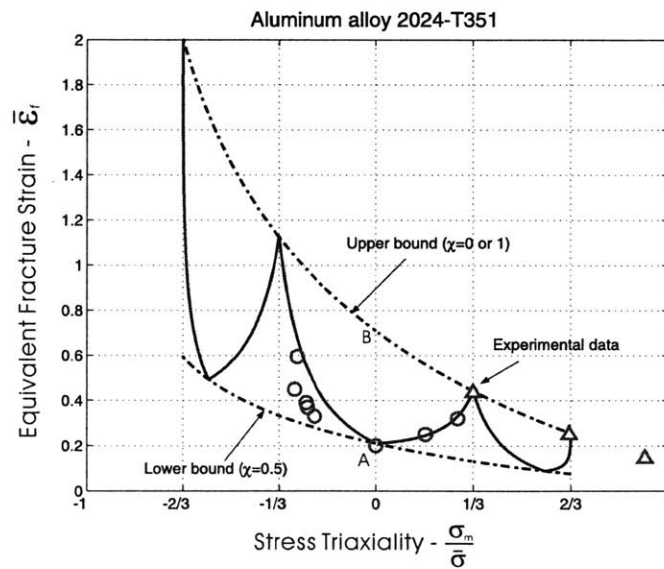


Figure 7.3: The fracture strain versus the stress triaxiality for the plane stress loading condition. Experimental data from [26].

In Fig. 7.3, the right three points (denoted by triangles) of experimental data are from the smooth and notched round bars and the rests (denoted by circles) are from the plane stress condition. For smooth and notched axisymmetric specimens, the fracture initiates at the center, where hydrostatic tension is the greatest. The upper bound shown in Fig. 7.3 is fitted from the axisymmetric data. The point of intersection of this upper bound and the vertical axis $\frac{\sigma_m}{\sigma_{eq}} = 0$ (denoted by point “B”) corresponds to the reference generalized tension condition, where the pressure is constant zero along the loading path. Point “B” defines the value of the reference fracture strain ε_{f0} . The nonlinear parameters p_{lim} and q are also obtained from the fitting of the upper bound. The ratio of the simple shear fracture strain (denoted by point “A”) and ε_{f0} defines the strain ratio γ . From Fig. 7.3, we can find that $\gamma = 0.30$. Batra et al [86] showed the fracture strain of AA 2024-T351 in torsion is about 0.4, which indicates a larger $\gamma = 0.57$.

In plane stress condition, the stress triaxiality is bounded by $-\frac{2}{3}$ and $\frac{2}{3}$. It can be clearly seen from Fig. 7.3 that the failure loci consists of three distinct branches, which correspond to $-\frac{2}{3} \leq T \leq -\frac{1}{3}$, $-\frac{1}{3} \leq T \leq \frac{1}{3}$ and $\frac{1}{3} \leq T \leq \frac{2}{3}$, respectively. Each branch represents a full cycle of χ from 0 to 1. The hydrostatic pressure of the final fracture state varies on the fracture envelop. At the $-\frac{2}{3} \leq T \leq -\frac{1}{3}$ branch, the material is under biaxial compression or in the third quadrant of the principle stress plane. Thus, the hydrostatic pressure is compressive, which increases the ductility of the material. This results in that this branch is much higher than the other two. On the other hand, the $\frac{1}{3} \leq T \leq \frac{2}{3}$ branch represents the biaxial tension or the first quadrant, which results in a decrease of the equivalent fracture strain. The middle branch or the second and fourth quadrant, which has $-\frac{1}{3} \leq T \leq \frac{1}{3}$, is mixed by a compressive hydrostatic pressure on the left half and a tensile hydrostatic pressure on the right half. The upper bound and lower bound of the fracture strain with respect to the stress triaxiality are also plotted as dash-dot lines in Fig. 7.3. These bounds shows the maximum (under generalized tension or generalized compressive loading) and minimum (under generalized shear or plane strain condition) value of the failure strain under the same hydrostatic pressure for the triaxial loading cases.

Similar results were obtained by Barsoum and Faleskog [1] using a notched tube, as shown in Fig. 7.4. Their results are plotted in the stress triaxially vs. fracture strain and the Lode parameter vs. fracture strain planes, as shown in Fig. 7.5, where the Lode parameter is defined as $\mu = (2\sigma_2 - \sigma_1 - \sigma_3)/(\sigma_1 - \sigma_3)$.

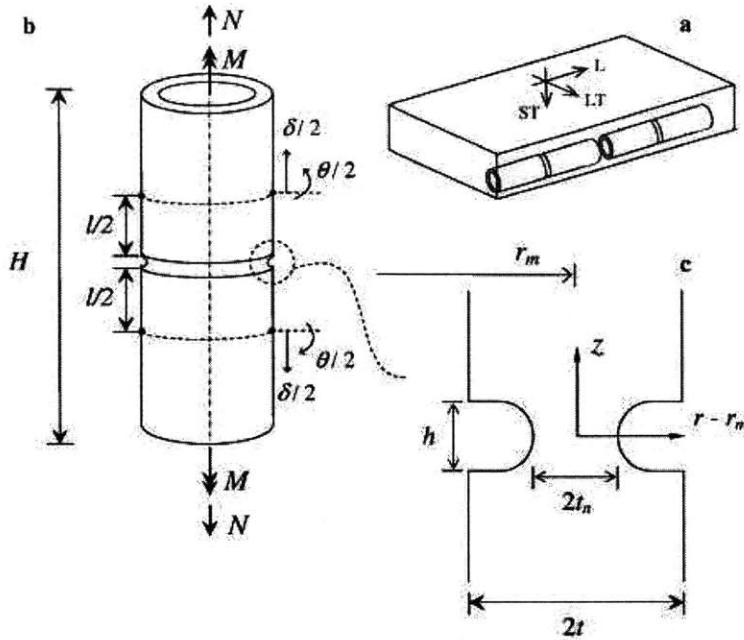


Figure 7.4: Notched tube specimen used by Barsoum and Faleskog. After Barsoum and Faleskog [1].

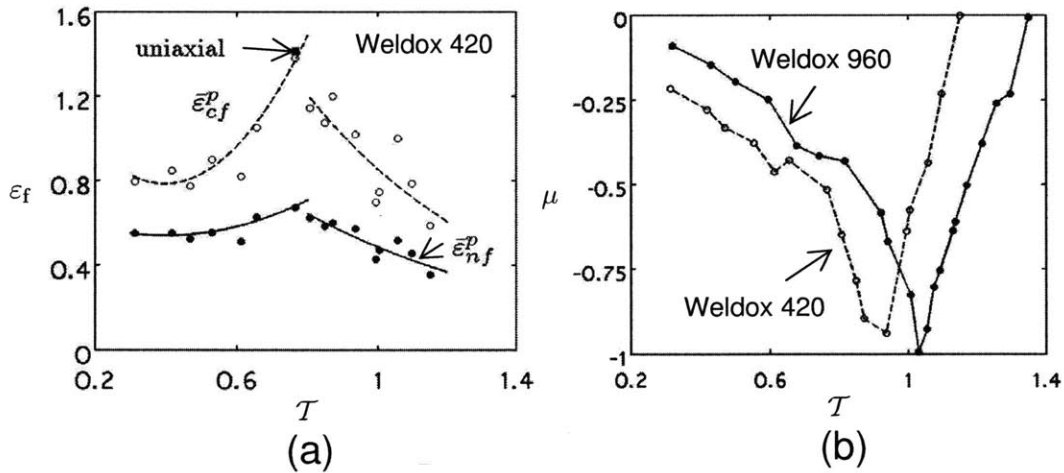


Figure 7.5: Fracture strain vs. stress triaxality and fracture strain vs. Lode parameter. After Barsoum and Faleskog [1].

Figure 7.5(a) is for material Wieldox 420 with the open circles indicating fracture strain and

the solid circles indicating strain at necking. For stress triaxiality alone, we know that the fracture strain is a monotonically decaying function. However, with the additional Lode angle effect, the shape of the fracture strain loci can change. From Fig. 7.5(b), the Lode angle effect results a lower fracture strain at both ends of the tested range of stress triaxiality where $\mu \approx 0$. The experimental fracture strain confirms this trend and shows a cusp in the middle. This is approximately where the Lode parameter is close to $\mu = -1$ (generalized tension).

In this regard, the fracture envelope can be plotted with respect to the stress triaxiality and the third invariant, alternatively [87]. The fracture envelope is shown in Fig. 7.6.

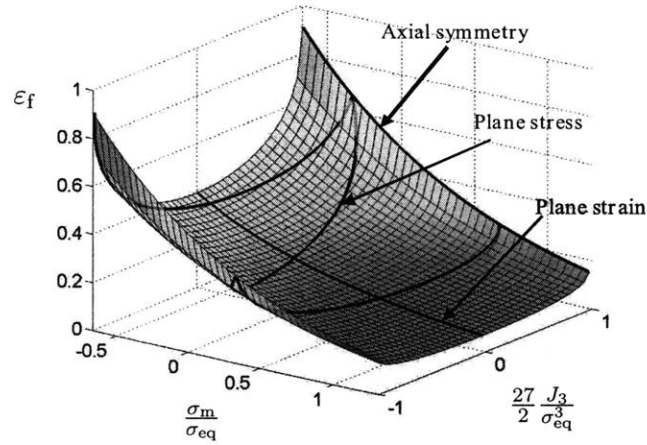


Figure 7.6: Representation of the fracture surface in the space of stress triaxiality and the deviatoric state variable. Note that the thick solid lines correspond to axisymmetric state, plane strain, and plane stress state.

It is assumed the fracture strain ratio at $\chi = 0.5$ and at $\chi = 1$ is assumed to be constant, with respect to the stress triaxiality, this ratio is slightly different for $\chi = 0.5$ and $\chi = 0$. Phenomenologically, let the upper limit and the lower limit be presented by the same exponentially decaying function, for instance, using Hancock and Mackenzie's function with different sets of parameters, i.e.

$$\begin{cases} \varepsilon_f^{\text{upper}} &= C_1 + C_2 \exp(-C_3 \sigma_m / \sigma_{\text{eq}}) & \text{for } \chi = 0; \\ \varepsilon_f^{\text{lower}} &= C_4 + C_5 \exp(-C_6 \sigma_m / \sigma_{\text{eq}}) & \text{for } \chi = 0.5. \end{cases} \quad (7.4)$$

In Chapter 13, using a modified Gurson like micro mechanical model, we show that these limited

curves are fitted by Eq. (7.4). This fracture envelope can be represented by

$$\varepsilon_f = \varepsilon_f^{\text{upper}} - \left(\varepsilon_f^{\text{upper}} - \varepsilon_f^{\text{lower}} \right) \left[1 - \left(\frac{27 |J_3|}{2 \sigma_{\text{eq}}^3} \right)^k \right]^{(1/k)} \quad (7.5)$$

where k is a shape parameter characterizing the sensitivity of the third invariant of the stress deviator.

Chapter 8

Elasto-Plastic Constitutive Equations and Numerical Aspects

Following the modeling technique of the damage plasticity theory discussed in the previous chapters, we present the constitutive equations and the numerical integration scheme applied in the present study.

The present elasto-plastic theory based on small deformation, rate-independent plasticity with strain hardening and coupled with damage.¹

8.1 Damage plasticity theory

The constitutive equations are summarized as the following.

8.1.1 Kinematics

We assume that the total strain rate $\dot{\epsilon}$ admits the decomposition²

$$\dot{\epsilon} = \dot{\epsilon}^e + \dot{\epsilon}^p. \quad (8.1)$$

where $(\dot{})$ denotes the time derivative and ϵ^e and ϵ^p denote the elastic and the plastic part of the strain tensor.

¹Advices from Professor Lallit Anand in writing this section are greatly appreciated.

²A bold-faced letter denotes a tensor quantity and a normal faced letter denotes a scalar quantity.

From the assumption that the plastic flow does not induce changes in volume, the plastic strain rate $\dot{\epsilon}^p$ is **deviatoric**, i.e

$$\text{tr}\dot{\epsilon}^p = 0. \quad (8.2)$$

8.1.2 Power

The stress power per unit volume is

$$\mathcal{P} = \boldsymbol{\sigma} : \dot{\boldsymbol{\epsilon}}. \quad (8.3)$$

On account of Eq. (8.2), the stress power can be decomposed into elastic and plastic parts:

$$\mathcal{P} = \boldsymbol{\sigma} : \dot{\boldsymbol{\epsilon}}^e + \boldsymbol{\sigma} : \dot{\boldsymbol{\epsilon}}^p. \quad (8.4)$$

Since the plastic strain rate is deviatoric, we note that Eq. (8.4) may be rewritten as:

$$\mathcal{P} = \boldsymbol{\sigma} : \dot{\boldsymbol{\epsilon}}^e + \mathbf{s} : \dot{\boldsymbol{\epsilon}}^p. \quad (8.5)$$

where

$$\mathbf{s} = \boldsymbol{\sigma} + p\mathbf{1}, \quad (8.6)$$

is the stress deviator and p is the pressure, i.e.

$$p = -\frac{1}{3}\text{tr}\boldsymbol{\sigma}. \quad (8.7)$$

The plastic dissipation power is

$$\mathcal{D} = \mathbf{s} : \dot{\boldsymbol{\epsilon}}^p \geq 0. \quad (8.8)$$

8.1.3 Constitutive equations

Elastic response

We now introduce the damage variable ($D \in [0, 1]$) to the material from the outset of separation of the matrix material from the continuum media. It is assumed the mechanical property of the matrix material does not change with respect to the damage. The plastic damage effect on the stress-strain relationship is by a weakening factor $w(D)$ which is a function of the ductile damage. It is assumed that the elastic response of the material is isotropic and governed by the *rate* constitutive equation

$$\dot{\sigma} = w(D)\mathbb{C}_0 [\dot{\varepsilon} - \dot{\varepsilon}^p], \quad (8.9)$$

where

$$\mathbb{C}_0 = 2G_0\mathbb{I} + \left(K_0 - \frac{2}{3}G_0\right) \mathbf{1} \otimes \mathbf{1} \quad (8.10)$$

is the fourth order ground-state isotropic elasticity tensor, with $G_0 > 0$ and $K_0 > 0$ the initial values of the shear and bulk moduli of the material, when $D = 0$. The elastic moduli at a damaged state, when $D \in (0, 1)$ are $G = w(D)G_0$ and $K = w(D)K_0$, respectively. The Poisson's ratio is assumed to remain constant throughout the damaging process.

Plastic response

Let

$$\sigma_{\text{eq}} \stackrel{\text{def}}{=} \sqrt{\frac{3}{2}\mathbf{s} : \mathbf{s}} \quad (8.11)$$

denote the **Mises equivalent stress** and

$$\sigma_{\text{M}} = \hat{\sigma}_{\text{M}}(\varepsilon^p) \quad (8.12)$$

denote the **resistance to the plastic flow** offered by the matrix material. The damage coupled yield condition is represented by

$$\Phi(\sigma, \sigma_{\text{M}}, D) = \sigma_{\text{eq}} - w(D)\sigma_{\text{M}} \geq 0; \quad (8.13)$$

the function $\Phi(\sigma, \sigma_{\text{M}}, D)$ is called the **yield function**.

Flow rule

We adopt the associative flow rule. The co-rotational flow rule is

$$\dot{\boldsymbol{\varepsilon}}^p = \dot{\varepsilon}^p \mathbf{n}, \quad (8.14)$$

where

$$\mathbf{n} = \frac{3}{2} \frac{\mathbf{s}}{\sigma_{\text{eq}}}, \quad (8.15)$$

is the normal outward vector to the yield surface³ and

$$\dot{\varepsilon}^p \stackrel{\text{def}}{=} \sqrt{\frac{2}{3} \dot{\boldsymbol{\varepsilon}}^p : \dot{\boldsymbol{\varepsilon}}^p}, \quad (8.16)$$

denotes the **equivalent plastic strain rate**.

Under these constitutive assumptions, the dissipation inequality Eq. (8.8) reduces to

$$\mathcal{D} = \sigma_{\text{eq}} \dot{\varepsilon}^p \geq 0, \quad (8.17)$$

and is trivially satisfied when $\dot{\varepsilon}^p > 0$.

Evolution equations for the internal variables

The evolution of σ_M due to strain hardening is taken to be

$$\dot{\sigma}_M = h(\varepsilon^p) \dot{\varepsilon}^p, \quad (8.18)$$

where $h(\varepsilon^p) = \partial \hat{\sigma}_M / \partial (\varepsilon^p)$ is the tangent modulus.

The evolution equation for the damage depends on the current stress state. From previous chapters, the damage rate takes the form

$$\dot{D} = g(\varepsilon^p, p, \theta_L) \dot{\varepsilon}^p \quad \text{with} \quad g(\varepsilon^p, p, \theta_L) = m \left(\frac{\varepsilon^p}{\varepsilon_f(p, \theta_L)} \right)^{(m-1)} \frac{1}{\varepsilon_f(p, \theta_L)} \quad (8.19)$$

where p and θ_L are the pressure and the Lode angle on the octahedral plane, m is a material constant, and ε_f denotes the fracture envelope and takes the form

³Note the tensor \mathbf{n} does not have unit magnitude

$$\varepsilon_f(p, \theta_L) = \varepsilon_{f0} \mu_p \mu_\theta, \quad (8.20)$$

where μ_p and μ_θ are the pressure dependence and the Lode angle dependence functions. The following forms are used, for example,

$$\mu_p = 1 - q \log \left(1 - \frac{p}{p_{\text{lim}}} \right), \quad (8.21)$$

and

$$\mu_\theta = 1 - (1 - \gamma) \left(\frac{|\theta_L|}{\pi/6} \right)^k, \quad (8.22)$$

where q , p_{lim} , γ and k are material constants and θ_L is the Lode angle.

Complementarity conditions. Consistency condition

The equivalent plastic strain rate $\dot{\varepsilon}^p$ is assumed to satisfy the *complementarity conditions* (Kuhn-Tucker condition) [88]:

$$\dot{\varepsilon}^p \geq 0, \quad \Phi(\boldsymbol{\sigma}, \sigma_M, D) \leq 0, \quad \text{and} \quad \dot{\varepsilon}^p \Phi(\boldsymbol{\sigma}, \sigma_M, D) = 0. \quad (8.23)$$

In addition, when $\dot{\varepsilon}^p \geq 0$, the consistency requirement

$$\dot{\varepsilon}^p \dot{\Phi}(\boldsymbol{\sigma}, \sigma_M, D) = 0. \quad (8.24)$$

needs to be satisfied. The consistency condition helps determine $\dot{\varepsilon}^p$ whenever it does not vanish. When $\dot{\varepsilon}^p > 0$

$$\dot{\Phi}(\boldsymbol{\sigma}, \sigma_M, D) = 0. \quad (8.25)$$

From Eqs. (8.9) and (8.13) and the evolution equations, Eqs. (8.18) and (8.19),

$$0 = \dot{\Phi}(\boldsymbol{\sigma}, \sigma_M, D) = \dot{\sigma}_{\text{eq}} - w(D)\dot{\sigma}_M - \sigma_M \frac{\partial w}{\partial D} \dot{D} \quad (8.26)$$

$$= \mathbf{n} : \dot{\boldsymbol{\sigma}} - w(D)h\dot{\varepsilon}^p - \sigma_M \frac{\partial w}{\partial D} g\dot{\varepsilon}^p \quad (8.27)$$

$$= w(D)\mathbf{n} : \mathbb{C}_0[\dot{\boldsymbol{\varepsilon}} - \dot{\varepsilon}^p] - w(D)h\dot{\varepsilon}^p - \sigma_M \frac{\partial w}{\partial D} g\dot{\varepsilon}^p \quad (8.28)$$

$$= w(D)\mathbf{n} : \mathbb{C}_0[\dot{\boldsymbol{\varepsilon}}] - \left[3w(D)G_0 + w(D)h + \sigma_M \frac{\partial w}{\partial D} g \right] \dot{\varepsilon}^p. \quad (8.29)$$

To carry out our analysis further we need to make an assumption about the evolution equations for the internal variables σ_M and D . In particular we *assume* that

$$\left[3wG_0 + wh + \sigma_M \frac{\partial w}{\partial D} g \right] > 0, \quad (8.30)$$

for all admissible states $(\boldsymbol{\sigma}, \sigma_M, D)$ that satisfy the yield condition. Under this assumption, $\dot{\Phi} = 0$ gives

$$\dot{\varepsilon}^p = \frac{w\mathbf{n} : \mathbb{C}_0[\dot{\boldsymbol{\varepsilon}}]}{\left[3wG_0 + wh + \sigma_M \frac{\partial w}{\partial D} g \right]}. \quad (8.31)$$

Thus, for $\Phi = 0$ and $\dot{\Phi} = 0$,

$$\dot{\varepsilon}^p \geq 0 \quad \Leftrightarrow \quad \mathbf{n} : \underbrace{(w \mathbb{C}_0[\dot{\boldsymbol{\varepsilon}}])}_{\text{trialstressrate}} \geq 0, \quad (8.32)$$

which helps to define standard loading and unloading conditions.

Similarly, we can trivially write the *damage loading/unloading condition*

$$\dot{D} \geq 0, \quad \text{and} \quad \Phi(\boldsymbol{\sigma}, \sigma_M, D) \leq 0, \quad \text{and} \quad \dot{D}\Phi(\boldsymbol{\sigma}, \sigma_M, D) = 0. \quad (8.33)$$

8.2 Time integration procedure

The backward Euler algorithm is applied to the flow rule to ensure satisfactory convergence of the solution. The state variables D_n , the stress $\boldsymbol{\sigma}_n$ and the plastic strain ε_n^p are known at time t_n . An

increment in the strain $\Delta\boldsymbol{\varepsilon}$ is applied in the time interval $[t_n, t_{n+1}]$. The task is to solve for the stress tensor and the internal variables at time t_{n+1} .

Given: $\{\boldsymbol{\sigma}_n, \boldsymbol{\varepsilon}_n^p, D_n\}$ and $\Delta\boldsymbol{\varepsilon} = \boldsymbol{\varepsilon}_{n+1} - \boldsymbol{\varepsilon}_n$ at time t_n .

Calculate: $\{\boldsymbol{\sigma}_{n+1}, \boldsymbol{\varepsilon}_{n+1}^p, D_{n+1}\}$ at time $t_{n+1} = t_n + \Delta t$.

8.2.1 Elastic update

The trial stress is calculated by assuming the incremental strain is purely elastic. Since the trial calculation is elastic, there is no damage increment. Therefore the trial stress is

$$\boldsymbol{\sigma}_{n+1}^{\text{trial}} = \boldsymbol{\sigma}_n + w(D_n) \mathbb{C}_0 [\Delta\boldsymbol{\varepsilon}]. \quad (8.34)$$

Substituting $\boldsymbol{\sigma}_{n+1}^{\text{trial}}$ into the yield function Φ , if

$$\Phi(\boldsymbol{\sigma}_{n+1}^{\text{trial}}, \sigma_M, D_n) \leq 0 \quad (8.35)$$

then the deformation is elastic and the stress at t_{n+1} is the trial stress and no damage occurs, i.e.

$$\boldsymbol{\sigma}_{n+1} = \boldsymbol{\sigma}_{n+1}^{\text{trial}} \quad (8.36)$$

$$\boldsymbol{\varepsilon}_{n+1}^p = \boldsymbol{\varepsilon}_n^p \quad (8.37)$$

$$D_{n+1} = D_n \quad (8.38)$$

If $\Phi > 0$, the deformation is elastic-plastic. The plastic strain increment is no longer zero. A plastic correction step is used to enforce the consistency condition.

8.2.2 Elastic-plastic update

evolution of plastic strain

Unlike conventional plastic model, the change of the yield surface is due to the combined effect of the strain hardening of the matrix material and the weakening due to the plastic damage. The global equilibrium has to be used to solve for the weakening of the elastic moduli.

The evolution of the deviatoric stress tensor can be graphically represented in Fig. 8.1 for the one-dimensional case.

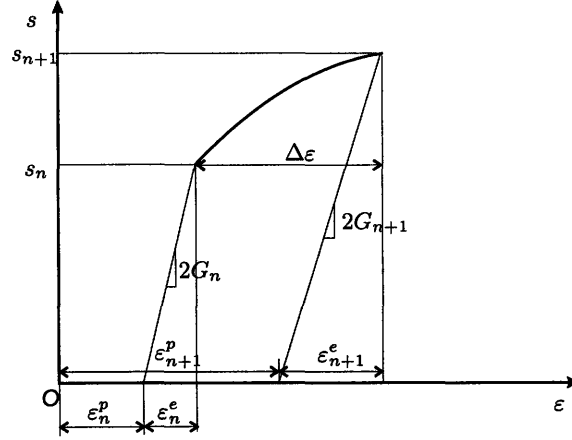


Figure 8.1: A schematic drawing illustrates the evolution of the deviatoric stress tensor.

Knowing the elastic part of strain at time t_n is

$$\boldsymbol{\varepsilon}_n^e = \frac{1}{w(D_n)} \mathbf{C}_0^{-1} \boldsymbol{\sigma}_n. \quad (8.39)$$

For simplicity, denoting the trial elastic part of the strain tensor to be

$$\boldsymbol{\varepsilon}^\dagger = \boldsymbol{\varepsilon}_n^e + \Delta \boldsymbol{\varepsilon}. \quad (8.40)$$

and the deviatoric part of $\boldsymbol{\varepsilon}^\dagger$ can be written as

$$\hat{\boldsymbol{\varepsilon}} = \boldsymbol{\varepsilon}^\dagger - \frac{1}{3} (\text{tr} \boldsymbol{\varepsilon}^\dagger) \mathbf{1}. \quad (8.41)$$

and the equivalent elastic strain is

$$\tilde{\varepsilon} = \sqrt{\frac{2}{3} \hat{\boldsymbol{\varepsilon}} : \hat{\boldsymbol{\varepsilon}}} \quad (8.42)$$

The deviatoric trial stress is

$$\mathbf{s}^{\text{trial}} = 2w(D_n)G_0 \hat{\boldsymbol{\varepsilon}}. \quad (8.43)$$

and the equivalent trial stress is

$$\sigma_{\text{eq}}^{\text{trial}} = \sqrt{\frac{3}{2} \mathbf{s}_{n+1}^{\text{trial}} : \mathbf{s}_{n+1}^{\text{trial}}} = 3w(D_n)G_0 \tilde{\varepsilon}. \quad (8.44)$$

Following the radial return algorithm, the incremental plastic strain is in the same direction as

the deviatoric trial stress

$$\Delta \boldsymbol{\varepsilon}^p = \Delta \varepsilon^p \mathbf{n}_{n+1}, \quad (8.45)$$

where \mathbf{n}_{n+1} is the direction of the deviatoric trial stress, i.e.

$$\mathbf{n}_{n+1} = \frac{3}{2} \frac{\mathbf{s}^{\text{trial}}}{\sigma_{\text{eq}}^{\text{trial}}}. \quad (8.46)$$

Note that $\hat{\boldsymbol{\varepsilon}}$ and \mathbf{n}_{n+1} are in the same direction and can be related by

$$\hat{\boldsymbol{\varepsilon}}_{n+1} = \tilde{\boldsymbol{\varepsilon}} \mathbf{n}_{n+1}. \quad (8.47)$$

Now, the task reduces to find the magnitude of the incremental plastic strain $\Delta \varepsilon^p$ that satisfies the consistency condition.

From the generalized Hooke's law, the real deviatoric stress is

$$\mathbf{s}_{n+1} = 2w(D_{n+1})G_0 (\hat{\boldsymbol{\varepsilon}} - \Delta \varepsilon^p \mathbf{n}_{n+1}) \quad (8.48)$$

$$= 2w(D_{n+1})G_0 (\tilde{\boldsymbol{\varepsilon}} - \Delta \varepsilon^p) \mathbf{n}_{n+1}. \quad (8.49)$$

Taking the inner product of Eq. (8.49) with itself gives

$$\sigma_{\text{eq}n+1} = 3w(D_{n+1})G_0 (\tilde{\boldsymbol{\varepsilon}} - \Delta \varepsilon^p), \quad (8.50)$$

From discretization of time, the continuous consistency requirement loosens to a discrete one. By the discrete consistency condition, we know that the stress at time t_{n+1} should be on the expanded or shrunk (due to the combined effect of strain hardening and material deterioration) yield surface. Therefore

$$\sigma_{\text{eq}n+1} = w(D_{n+1})\sigma_{Mn+1} = w(D_{n+1}) (\sigma_{Mn} + h\Delta \varepsilon^p). \quad (8.51)$$

where

$$h = \frac{\partial \hat{\sigma}_M}{\partial \varepsilon^p} (\varepsilon_n^p), \quad (8.52)$$

is the forward gradient of the plastic strain hardening modulus.

From Eqs. (8.50) and (8.51), the magnitude of the plastic correction is

$$\Delta\varepsilon^p = \frac{3G_0\tilde{e} - \sigma_{Mn}}{3G_0 + h}. \quad (8.53)$$

Once $\Delta\varepsilon^p = \Delta\varepsilon^p \mathbf{n}_{n+1}$ is known, the problem is fully defined.

internal variables update

Two internal variables ε^p and D need to be updated.

The damage is solved using Euler forward method. Knowing the pressure and the relative ratio of the stress deviator at time t_n , the reference fracture strain ε_f is computed using Eq. (8.20). The damage at time t_{n+1} is

$$D_{n+1} = D_n + m \left(\frac{\varepsilon_n^p}{\varepsilon_f} \right)^{(m-1)} \frac{\Delta\varepsilon^p}{\varepsilon_f} \quad (8.54)$$

The weakening factor is then calculated

$$w(D_{n+1}) = 1 - D_{n+1}^\beta. \quad (8.55)$$

The update on the plastic strain is trivially

$$\varepsilon_{n+1}^p = \varepsilon_n^p + \Delta\varepsilon^p. \quad (8.56)$$

stress update

The elastic strain at time t_{n+1} is

$$\varepsilon_{n+1}^e = \varepsilon^\dagger - \Delta\varepsilon^p. \quad (8.57)$$

and

$$\boldsymbol{\sigma}_{n+1} = w(D_{n+1}) \mathbb{C}_0 \varepsilon_{n+1}^e. \quad (8.58)$$

We emphasize, in the present algorithm, the elastic moduli degrades as damage accumulates. The advantage of the present formula is two-folded:

(1) It is physically sound to incorporate the weakening of elastic moduli of the material since it is not negligible for large plastic damage problems.

(2) It is computationally more efficient because only one correction step is needed to solve the consistency condition within each time step.

8.2.3 Summary of integration procedure

Given: $\{\sigma_n, \varepsilon_n^p, D_n\}$ and $\Delta\varepsilon = \varepsilon_{n+1} - \varepsilon_n$ at time t_n .

Step 1:

Calculate

$$\left. \begin{aligned} \varepsilon_n^e &= \frac{1}{w(D_n)} \mathbf{C}_0^{-1} \sigma_n; \\ \varepsilon^\dagger &= \varepsilon_n^e + \Delta\varepsilon; \\ \hat{\varepsilon} &= \varepsilon^\dagger - \frac{1}{3} (\text{tr} \varepsilon^\dagger) \mathbf{1}; \\ \tilde{\varepsilon} &= \sqrt{\frac{2}{3} \hat{\varepsilon} : \hat{\varepsilon}}. \end{aligned} \right\} \quad (8.59)$$

$$\sigma_{n+1}^{\text{trial}} = \sigma_n + w(D_n) \mathbf{C}_0 [\Delta\varepsilon]. \quad (8.60)$$

$$\sigma_{\text{eq}}^{\text{trial}} = 3w(D_n) G_0 \tilde{\varepsilon}. \quad (8.61)$$

Step 2:

IF

$$\sigma_{\text{eq}}^{\text{trial}} \leq (1 - D_n) \sigma_{Mn}(\varepsilon_n^p), \quad (8.62)$$

THEN (*elastic update*)

$$\left. \begin{aligned} \sigma_{n+1} &= \sigma_{n+1}^{\text{trial}}, \\ \varepsilon_{n+1}^p &= \varepsilon_n^p; \\ D_{n+1} &= D_n. \end{aligned} \right\} \quad (8.63)$$

ELSE IF

$$\sigma_{\text{eq}}^{\text{trial}} > (1 - D_n)\sigma_{Mn}(\varepsilon_n^p), \quad (8.64)$$

THEN (*elastic-plastic update*)

$$\left. \begin{aligned} \mathbf{n}_{n+1} &= \frac{3}{2} \frac{\mathbf{s}^{\text{trial}}}{\sigma_{\text{eq}}^{\text{trial}}}; \\ \Delta\varepsilon^p &= \frac{3G_0\tilde{\varepsilon} - \sigma_{Mn}}{3G_0 + h}; \\ \Delta\varepsilon^p &= \Delta\varepsilon^p \mathbf{n}_{n+1} \end{aligned} \right\} \quad (8.65)$$

and

$$\left. \begin{aligned} D_{n+1} &= D_n + m \left(\frac{\varepsilon_n^p}{\varepsilon_f} \right)^{(m-1)} \frac{\Delta\varepsilon^p}{\varepsilon_f}; \\ w(D_{n+1}) &= 1 - D_{n+1}^\beta; \\ \varepsilon_{n+1}^p &= \varepsilon_n^p + \Delta\varepsilon^p. \end{aligned} \right\} \quad (8.66)$$

and

$$\left. \begin{aligned} \varepsilon_{n+1}^e &= \varepsilon^\dagger - \Delta\varepsilon^p; \\ \sigma_{n+1} &= w(D_{n+1})\mathbf{C}_0\varepsilon_{n+1}^e. \end{aligned} \right\} \quad (8.67)$$

END

All necessary field variables $\{\sigma_{n+1}, \varepsilon_{n+1}^p, D_{n+1}\}$ are updated at time $t_{n+1} = t_n + \Delta t$.

Chapter 9

Experimental Program

The damaging process is complicated when multi-axial and/or non-proportional loadings are considered. Even when an experiment is done, a quantitative analysis of the results to determine the damage function is often hard to conduct. In the present chapter, an experimental program is presented. The objective of this experimental program is to determine the material parameters for further numerical study. The material selected to be experimentally investigated is aluminum alloy 2024-T351.

Aluminum alloy 2024-T351 is one of the widely used aluminum alloy in industry. Its application includes aircraft structural components, aircraft fittings, hardware, truck wheel and parts for the transportation industry because of its high strength, excellent fatigue resistance and good strength-to-weight ratio. The main alloying element of 2024-T351 is copper. The heat treatment for this material is solution heat treated, stress-relieved stretched and then cold worked. The chemical composition of aluminum alloy 2024 is listed in Table 9.1.

Table 9.1: The chemical composition of aluminum alloy 2024.

	Si	Fe	Cu	Mn	Mg	Cr	Zn	Ti
Weight %	0.50	0.50	3.8-4.9	0.30-0.9	1.2-1.8	0.10	0.25	0.15

One reason for choosing aluminum alloy 2024-T351 is that there is a wealth of works on the mechanical properties of the aluminum alloy 2024-T351 covering the experimental investigation

and numerical simulation, which makes comparison between results obtained by different research groups and cross-validation possible. Another reason for the choice is that this material has been investigated before in the Impact and Crashworthiness Lab [89].

All experiments were conducted using a screw driven 200 kN MTS universal testing machine. The test conditions cover a wide range of mean stress and Lode angle. The program includes a set of un-notched and notched round bars under axial tension, a set of cylinders under axial compression, a set of doubly-grooved plates (transversely plane strain) under uniaxial tension and a set of three point bending tests. A material parameter calibration process is then followed. The cylinder compression tests and the un-notched and notched round bar under tension tests will be used to calibrate the pressure dependence of the material. The Lode angle dependence is calibrated from the doubly-grooved plate under uniaxial tension tests and the axial tension tests of round bars. From previous chapters, a set of minimum four parameters defining the fracture envelope needs to be calibrated.

A parallel numerical study of these tests were conducted and are reported in Chapter 10. The objectives of the numerical simulations are to assess the obtained material parameter from experiments and to fine tune the parameters using an iterative “*try-and-error*” method. The main aspects to be assessed are the predicted fracture modes and the load-deflection curves.

A block of 4”-by-4” cross-section and 6-foot-long aluminum alloy 2024-T351 were purchased from McMaster.com. All specimens in the present experimental study were cut from this block. The cross-section 4”-by-4” was chosen with the initial assumption of less anisotropy in the two lateral direction of same size. This assumption was later disproved by the experimental results. This suggests rolling process was involved in the history of processing this material. For the convenience of further discussion, Fig. 9.1 shows the direction convention for the principal directions of the aluminum alloy block.

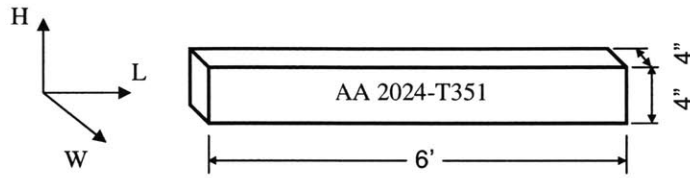


Figure 9.1: The direction convention for the block of aluminum alloy.

9.1 Pressure dependence calibration

9.1.1 Un-notched and notched round bar tensile tests

A series of tensile specimens were cut in the longitudinal direction. The geometry and the dimensions of the specimens used in this line of study are shown in Fig. 9.2.

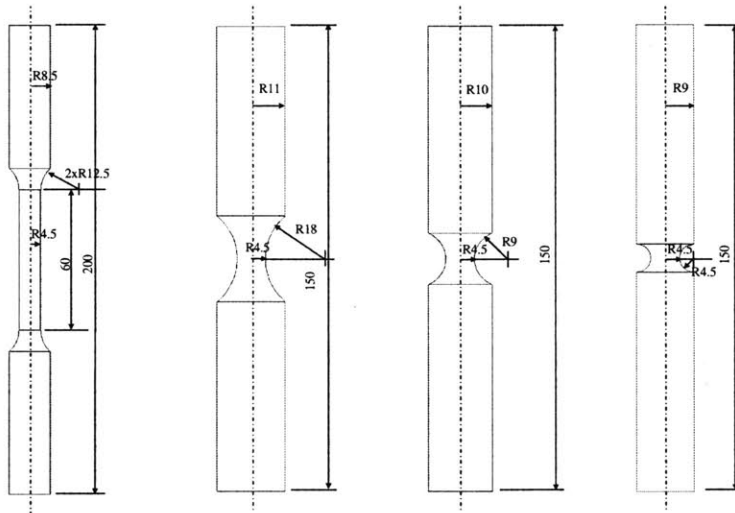
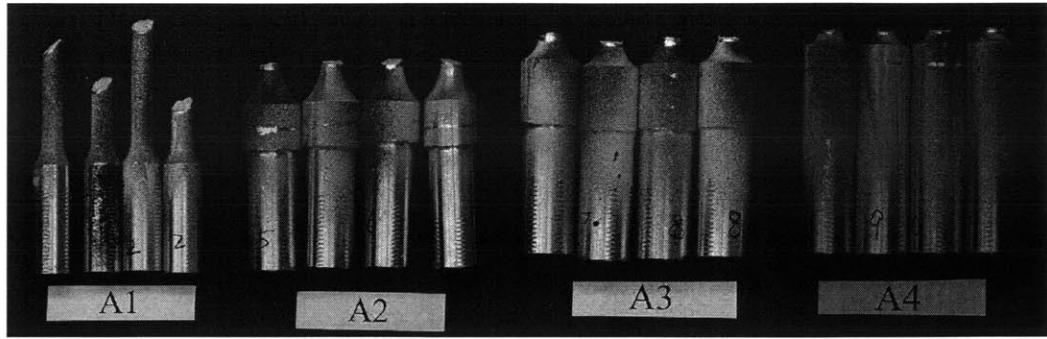


Figure 9.2: The un-notched and notched round bar specimen. (from left to right: un-notched, notch radii=18mm, 9mm and 4.5mm, respectively)

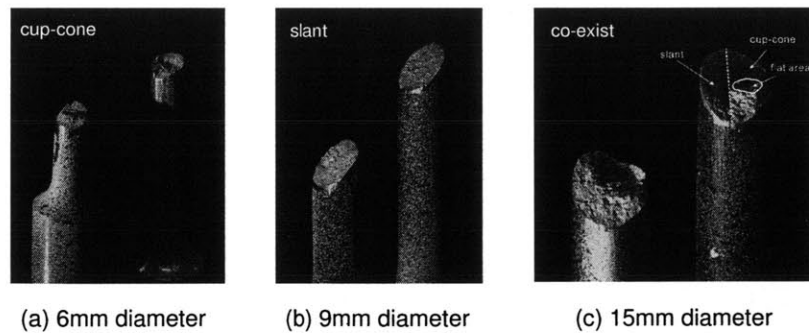
The specimens were pulled all the way to complete separation. The post mortem specimens are shown in Fig. 9.3.



(a) Un-notched (b) 18 mm notch (c) 9 mm notch (d) 4.5 mm notch

Figure 9.3: The post mortem specimens of un-notched and notched round bars.

For the notched specimens, a cup-cone type of fracture mode is found. It is noteworthy that the 9mm diameter un-notched round bars shows a slant dominant type of crack rather than a cup-cone type of fracture commonly found in ductile metals. Additional tests on two different diameters were performed with 6mm diameter and 15mm diameter un-notched round bars. The fracture surfaces are shown in Fig. 9.4. For the 6mm diameter specimen, there is a flat area in the center of the crack and the shear lips are on opposite side of the two separated side. For the 15mm diameter round bar, a mixed slant and cup-cone mode is found. The slant fracture surface does not extend to the whole area, but covers half of the fracture surface. A similar mode of cup-cone was found on the other half of the fracture surface.



(a) 6mm diameter (b) 9mm diameter (c) 15mm diameter

Figure 9.4: Different fracture modes were found for un-notched round tensile bars. Left: 6mm, middle: 9mm and right: 15mm diameters.

Chapter 10

Determination of the Fracture Envelope

Experimental investigation brings information needed to better understand the real world events. In return, such understanding has to be verified by additional measurement. In reality, direct experimental measurement is often incomplete and difficult in the local fracture point or in the time frame. Therefore, we need computational tools to expand our vision and to reveal more details of the physical world.

The proposed damage plasticity model is implemented into a finite element code LS-DYNA as a user defined material subroutine. In this chapter, we combine the numerical tools with the experimental program in the previous chapter to determine the fracture envelope of aluminum alloy 2024-T351. The calibrated material parameters are used in the following chapters to assess the validity and accuracy of the proposed damage plasticity model.

The objectives of this study are (1) to determine the matrix stress-strain curve; (2) to determine the pressure sensitivity; and (3) to determine the Lode angle dependence.

From the development of the damage plasticity model, the mechanical response of the solid material is coupled with the damaging process. Moreover, the rate of damage depends on the stress/strain state of the material. The current experimental technique does not allow the author to single out only one factor at a time and to measure the fracture dependence of it. Therefore, there is no easy way to calibrate these curves since the influential factors are entangled. Assumptions have to be made to allow a starting point to be estimated. The starting data are then used in an

iteration using numerical methods. A “*try-and-error*” method is adopted and parallel simulation jobs were run in order to have good agreement with the more than one experimental curves.

10.1 Determination of the stress-strain curve

As described in the previous modeling chapters, the matrix material is considered to be isotropic and volumetrically conservative in plastic deformation. It is further assumed that the matrix material obeys J_2 plasticity theory. Therefore, no pressure dependence or Lode angle dependence of the matrix strength is assumed in the present study.

Ideally, the upsetting load displacement curve is preferred to be used to calibrate the matrix stress strain curve. The reason is two-fold. Firstly, the plastic deformation induced material weakening is less significant in upsetting tests. Secondly, the fracture strain in upsetting is significantly higher than that in tensile test, which allows more accurate curve fitting.

While the necking problem introduces geometric non-uniformity, the upsetting tests also have barreling problem due to frictions on end surfaces. Rather than tracking the exact change of geometry of the compressed cylinder along the deformation path, we use the numerical methods to obtain the matrix stress-strain curve.

The load displacement curves of the present material show larger than expected difference in tension and in compression. Considering the fact that the material is anisotropic and has micro structure texture, it is not possible to find a stress strain curve that agrees well both in tension and in compression. Therefore, we calibrate the matrix strength in tension and compression separately.

For many metallic materials, the stress-strain curve can be assumed to be a power law function. In order to obtain a precise fit of the experimental curves, a three parameter power law relationship is necessary, such as the so-called “*Swift*” relationship [95]. We assume the strain hardening of the matrix material obeys the following rule:

$$\sigma_M = \sigma_{y0} \left(1 + \frac{\epsilon_p}{\epsilon_k} \right)^n \quad (10.1)$$

where σ_{y0} is a the original yield stress, ϵ_k is a reference strain and n is the strain hardening exponent.

It is generally accepted that the damage accumulation is an acceleration process. The stiffness reduction is a negligible at the beginning of the plastic distortion [14]. For an intact material, the

loss of material strength due to damage is ignored; therefore, the matrix strength can be fitted using Eq. (10.1). We used the true stress strain curve of the upsetting tests of 11.25mm long cylinder to determine the matrix stress strain curve.

To minimize the friction effect, the first test of 11.25mm long cylinder in the second batch (with Teflon sheets) is used as the starting curve. The raw experimental load-displacement curve (with machine compliance) is shown in Fig. 10.1. Plotted also in Fig. 10.1 are the total deformation of the specimen, where the compliance of the testing machine is subtracted, and the plastic portion of the specimen deformation.

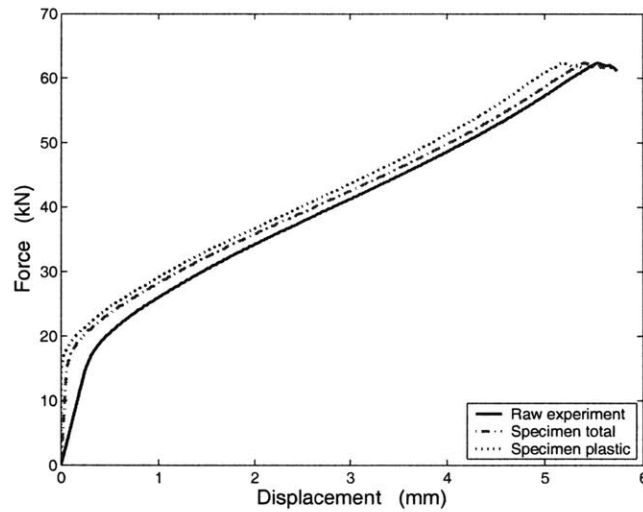


Figure 10.1: The experimental load-displacement curve of the upsetting test used in curve fitting (specimen A-11-1).

Assuming the compressive deformation is uniform, the true stress strain curve can be calculated. The true stress strain curve is then fitted using Eq. (10.1). Figure 10.2 shows fitting results for different ranges from $[0 - 0.05]$, $[0 - 0.10]$, $[0 - 0.20]$, $[0 - 0.30]$ to $[0 - 0.40]$. The abscissa in Fig. 10.2 is the absolute value of the logarithmic strain in the compressed cylinder. It is acknowledged that the three-parameter power law curve fitting generate slightly different results when fit with different plasticity ranges of the true stress strain curve. However, such difference is not significant. It can be seen that the difference of these fittings curves are negligible in the strain range of $[0 - 0.2]$.

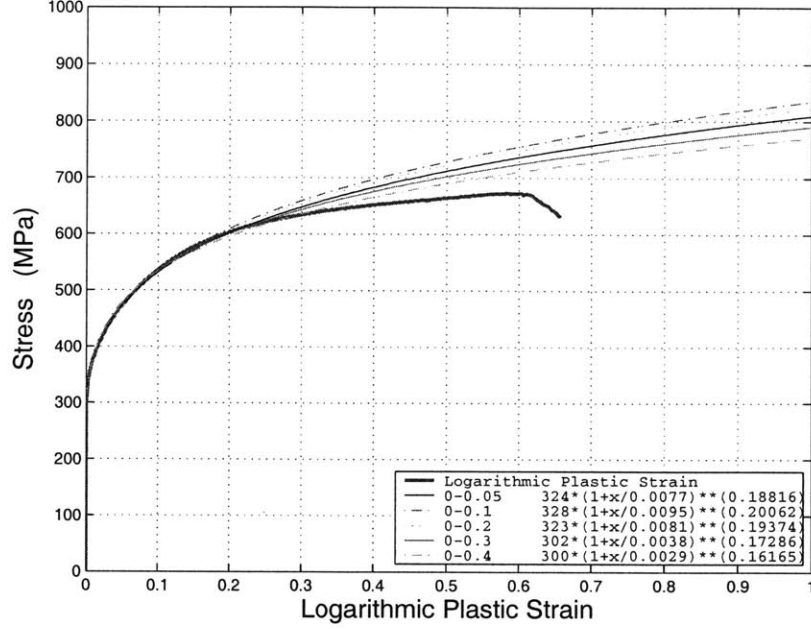


Figure 10.2: The direction convention for the block of aluminum alloy.

After a few trial simulations, the fitting results from [0 - 0.3] was used as the starting point for iterative simulations. The matrix stress strain curves in compression can be represented by

$$\sigma_M = 302 \left(1 + \frac{\epsilon_p}{0.00387} \right)^{0.173} . \quad (10.2)$$

The tensile stress strain curve is shorter than compressive curves and does not allow to be fitted in a wide range. It is often assumed that the material does not exhibits sensible weakening before necking in tensile round bar occurs. Therefore, in the present study, we assume the material strength before necking occurs in a un-notched tensile round bar is not subjected to weakening. For the present material, necking occurs around 12%. We fit the tensile stress strain curve before the onset of necking in the range of [0 - 0.1]. The post necking true stress strain is extrapolated using the fitted curve. The fitted tensile stress strain curve for matrix can be represented by

$$\sigma_M = 300 \left(1 + \frac{\epsilon_p}{0.00769} \right)^{0.185} . \quad (10.3)$$

The experimental tensile stress strain curve and the fitted one for matrix material are plotted

together in Fig. 10.3. For comparison convenience, the compressive stress strain curve are also plotted.

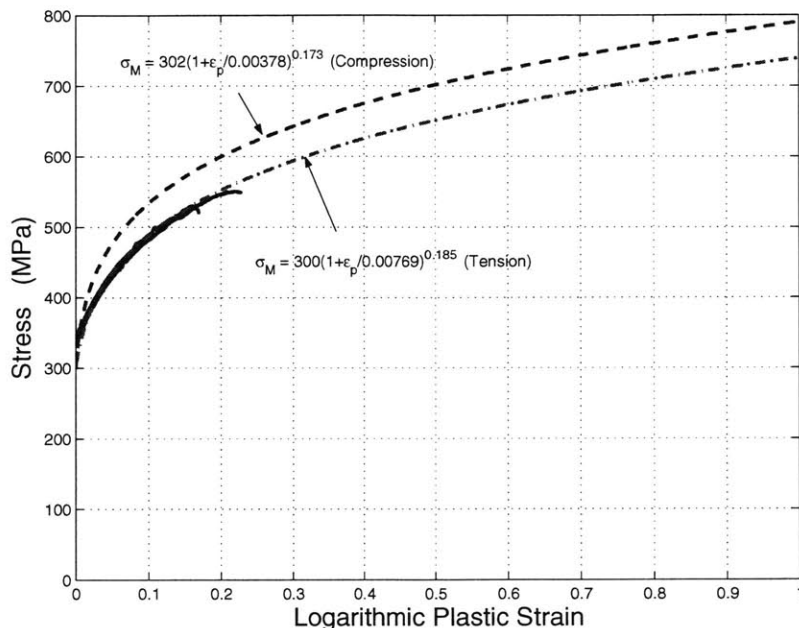


Figure 10.3: The experimental tensile stress strain curve and the fitted one for matrix in the longitudinal direction.

10.2 Determining the weakening function

In the real world, the material weakens due to plastic damage. The experimentally measure load-displacement relationship along the full plastic loading path up to the fracture point is compared with the matrix material response to obtain a weakening function.

In the proposed damage plasticity model, the damage accumulation depends on the strain ratio $\varepsilon_p/\varepsilon_f$, i.e. the ratio of the current plastic strain to the fracture strain based on the current stress state. The fracture strain in the upsetting test is assumed to be constant and is estimated using the mean pressure. The Lode angle is approximately $\theta_L = \pi/6$. The damage rate is assumed to be linearly depends on the plastic strain, which results a quadratic damage along the path. Using a power law weakening function, the only parameter needs to be calibrated is the weakening exponent

β in the weakening function $w(D)$.

Prior to this experimental study, estimation [96] was made from a set test results of notched and un-notched tensile round bars by Bao [89] (see Table 10.1). The fracture strain in uniaxial compression test is estimated to be 1.1. Knowing the power law damage rule with an exponent of 2.0, the intrinsic mechanical response of the material can be determined if the weakening exponent is known. In order to obtain some confidence in the above fitting results, the intrinsic mechanical response of the material in a uniaxial compression is plotted in Fig. 10.4 for several weakening exponents $\beta = 1$, $\beta = 2$ and $\beta = 3$. The matrix stress strain curve corresponds to an infinity β .

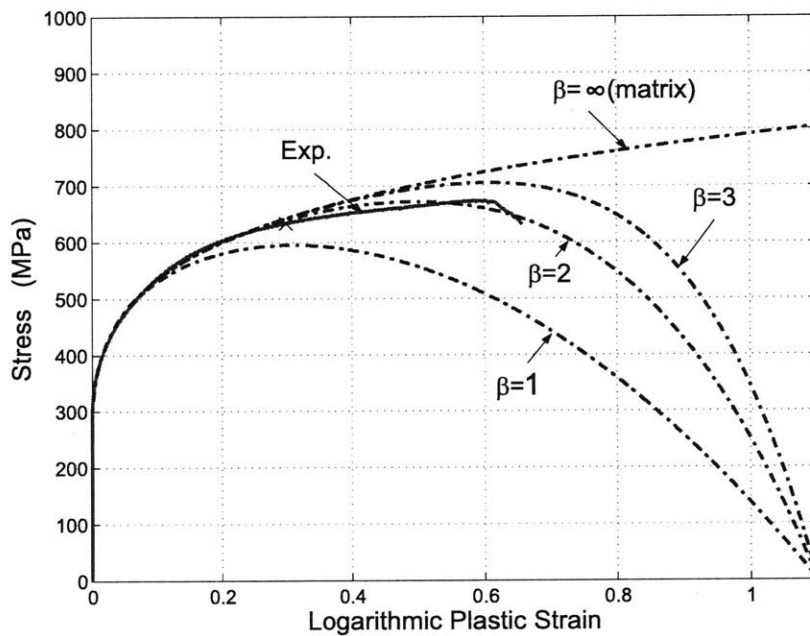


Figure 10.4: The intrinsic relationship of the stress strain curve of the material.

From Fig. 10.4, it can be determined that the weakening factor $\beta = 2$ fit the current material best.

Now, a set of starting parameters is found for the material aluminum alloy 2024-T351. These parameters are listed in Table 10.1.

Table 10.1: A list of material parameters used as a starting point for further iterative fine tuning.

ε_{f0}	p_{lim}	q	γ	m	β
0.7	926 MPa	0.97	0.3	2.0	2.0

An exhaustive study of the dependence on all the parameters involved is overwhelming. Therefore, assumptions and estimations have to be made to simplify the procedure. We consider that we have enough confidence in the determined matrix material strength and the damaging and weakening parameters. As is revealed in Chapter 8, the tested material exhibits some kind of texture in the micro structure and there is a difference in load displacement curve between tension and compression. This difference cannot be modeled by the damage alone. Here, we adopted two different set of matrix strength parameters, i.e. σ_{y0} , ε_k and n , for tension and for compression. We assume other material parameters are identical for all load condition. Moreover, we fix the damaging exponent m and the weakening exponent β in our iteration. The iterative numerical study is focused on the calibration of the material parameters regarding to the fracture envelope.

10.3 Determination of the fracture envelope

Four parameters are needed in the present set of functions to defined the fracture envelope - one for reference strain ε_{f0} , two for pressure dependence function p_{lim} and q and one for the Lode angle dependence function γ .

From the starting set of parameters, a set of four numerical simulations using one upsetting test, one tensile un-notched round bar, one tensile notched round bar and one tensile doubly-grooved plate were run in conjunction with the experiments. This set of cases was selected to include at least three different pressure tests and at least two different Lode angle tests.

The selected numerical models are shown in Fig. 10.5. To be realistic, we deemphasize the mesh dependence of finite element simulation of fracture problems here. The mesh size is chosen largely based on trial calculation and previous experiences. For the calibration simulation performed here, the mesh size is chosen to be around 0.1-0.15mm for four-node axisymmetrical elements and 0.3mm for eight-node brick elements. Main factors in the consideration are to complete the calculation

within a reasonable amount of time and to keep the element size small to reflect the strain gradient.

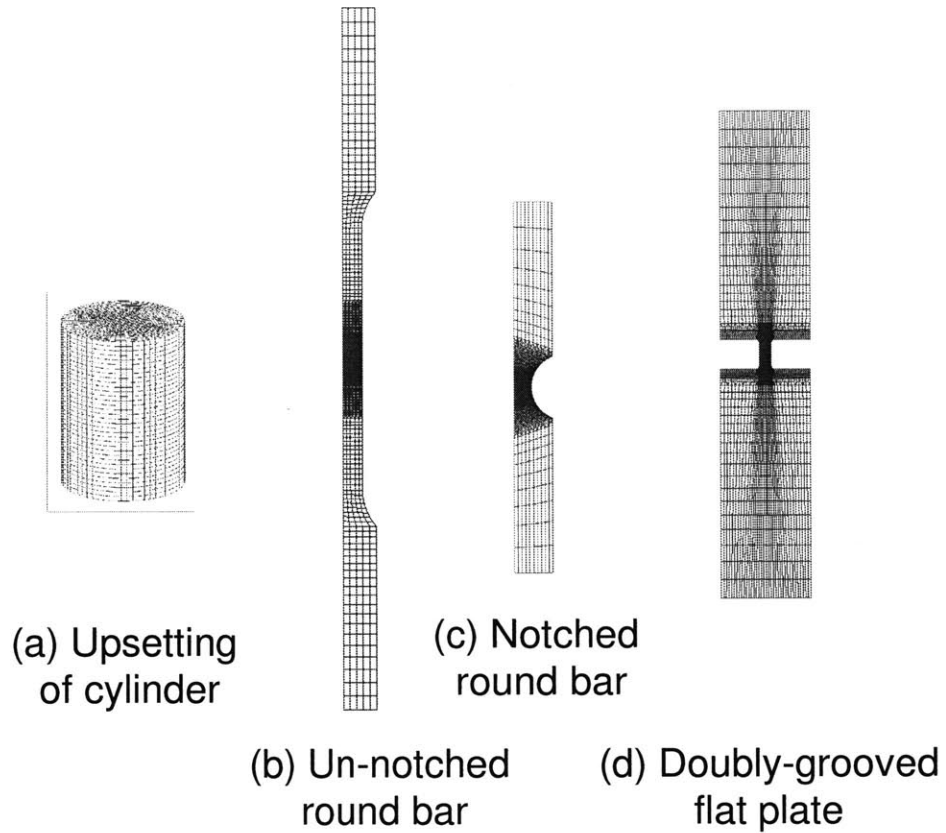


Figure 10.5: The four models used in the calibration of the fracture envelope: (a) upsetting of cylinder (brick elements); (b) tensile un-notched round bar (axisymmetric elements); (c) tensile notched round bar (axisymmetric elements); (d) doubly-grooved flat plate (plane strain elements).

About 40 simulations were performed while adjusting the four concerned parameters until good agreement is reached between all four numerical simulation and their corresponding experiment results. These results are shown below.

After the iterative numerical calibration procedure, the complete set of material parameters for

the material aluminum alloy 2024-T351 is listed in Table 10.2.

Table 10.2: A list of calibrated material parameters.

ϵ_{f0}	p_{lim}	q	γ	m	β
0.8	800 MPa	1.5	0.4	2.0	2.0

The comparison of the simulation results using the above parameters are the following.

(a) Upsetting of cylinder

The simulation is based on the compression 11.25mm long 8mm diameter cylinder with Teflon sheets as lubricant. The compressive matrix stress strain curve is used.

The deformation sequences are shown in Fig. 10.6. Plotted are the damage contours at the outer surface. A cut-out damage contour plot for a quarter of the model corresponding to the full model in Fig. 10.6 is shown in Fig. 10.7. Based on a few trial calculations, it is found that results from the friction coefficient 0.02 agree well with experiments. A more detailed discussion on the friction effects is in Chapter 11.

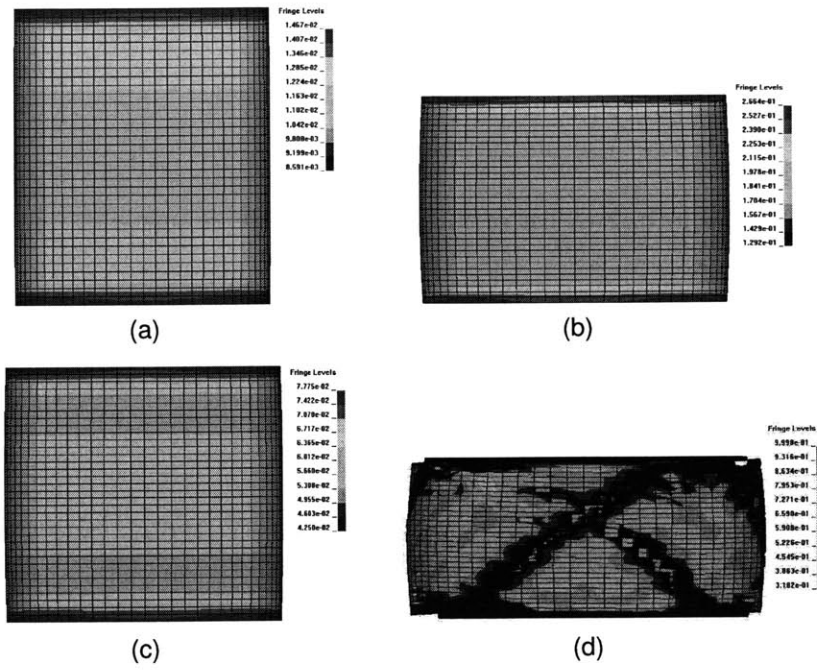


Figure 10.6: The deformation sequences of the upsetting test. Plotted is the damage contours.

Chapter 11

Prediction with Damage Plasticity

Model

In this chapter, a series of numerical simulation calculations for selected representative load conditions have been performed. These simulations can be separated into two parts. The first part represents the additional tests that were performed. The objective of this part is to verify the proposed model and to assess the accuracy of the material parameters. The second part of numerical simulation reported in this chapter was performed prior to the calibration of the material 2024-T351. The objective of these simulations is to illustrate the predictive capability of the proposed model in a wider range of loading conditions. The corresponding experiments were documented in early literatures. Consistent agreement is found between the predicted fracture patterns and the experimental results.

11.1 Notched round bars

In Chapter 10, we used the notched round bar with a 9mm notch radius in addition to other experiments to calibrate the material parameters related to damage and fracture. In this section, we further study the notched round bars with a 18mm and a 4.5mm notch radii. The experimental results are reported in Chapter 9.

11.1.1 Notch radius 18mm

The notched round bar with notch radius 18mm was simulated using axisymmetric elements. The element size at the notched area is about 0.1mm on each side. The deformation sequences of the notched section are shown in Fig. 11.1. A cup-cone fracture mode is predicted and the same was observed in the experiments.

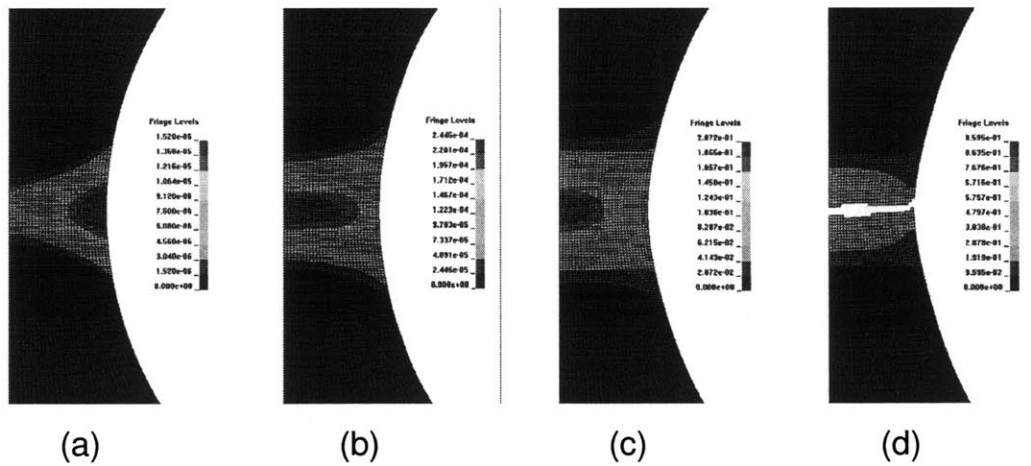


Figure 11.1: The deformation sequences of the notched specimen with a notch radius of 18mm.

It can be shown in Fig. 11.1 that at just beyond yielding point (Fig. 11.1(a)), the damage is the maximum at the outer surface. However, soon after yielding occurs, damage increases much faster at the center of neck due to the build up of the hydrostatic tension. The fracture initiates from the center of the neck and propagates towards the outer surface. A comparison of the load-deflection curve of the transverse plane strain tests is shown in Fig. 11.2.

gle dependence and without material weakening effect; case (c) without Lode angle dependence and with material weakening effect and case (d) without either Lode angle dependence or material weakening effect. The two calculations deactivating Lode dependence of fracture assumes the same fracture behavior for all deviatoric situations, i.e. $\gamma = 1$ with the second kind of Lode angle dependence function.

The predicted the fracture modes are shown in Fig. 11.16.

Numerical simulation efforts have been made to obtain a realistic fracture mode in the literature. It was found that the load-displacement curve can be achieved with two-dimensional finite element model using crack tip opening angle criterion [105] or microscopic void-nucleation-growth-coalescence model [106]. However, the three-dimensional nature in the near tip zone is not represented in these two-dimensional analysis. Three-dimensional finite element model using crack-tip-opening angle is also used to show the tunneling effect [107–109]. In these studies, the tunneling effect can be correctly modeled, but a flat through thickness fracture mode is predicted along the crack paths.

Although extensive theoretical and numerical work has been conducted on the stress and strain fields in the sharp notch crack tip, an insightful investigation of the transition from a flat crack to a slant mode is still lacking and is in need. In this study, we focus on the flat to slant transition in the fracture mode.

11.4.1 Slant/flat crack and mode transition

The compact tension (CT) specimens are sometimes observed to develop slant cracks within certain range of thickness to ligament ratio for some materials and in other cases a flat crack is observed [97; 110]. Simulation of the CT specimen reveals a complex deformation pattern. Close to the center of the crack tip in the thickness direction, fracture initiates in Mode I flat crack. Near the lateral surface of the specimen, the through thickness stress component disappears. In the process of the crack propagation towards the surface, shear lips form in a similar way as in a cup-cone fracture due to the transition of stress state. The initially opposite small shear lips create asymmetric forces at the crack tip and eventually turns the crack into a slant mode throughout the thickness direction [99; 100].

Numerical simulation efforts have been made to obtain a realistic fracture mode. It was found that the load-displacement curve can be predicted with plane strain finite element model using void-nucleation-growth-coalescence model [106; 111]. Three-dimensional finite element model using crack-tip-opening angle is also used to show the tunneling effect [108; 109]. Mathur *et al* [112] shows the void volume fraction become localized in two shear bands formed in the 45° direction ahead of the crack tip. Besson [113] predicted a shear localization by introducing anisotropy in the Gologanu model [114].

In the present study, we focus on the predicting of the slant fracture mode. The specimen is designed according to ASTM E399 with $a/W = 0.5$. The geometry is shown in Fig. 11.21.

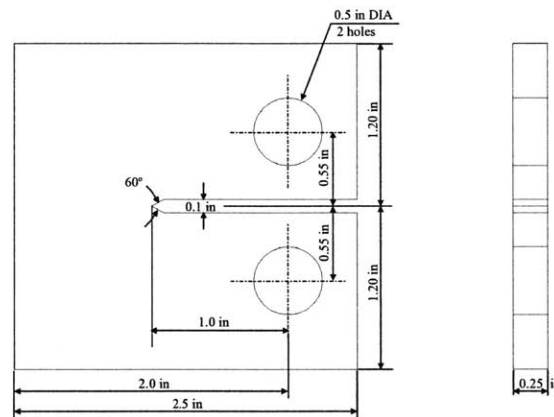
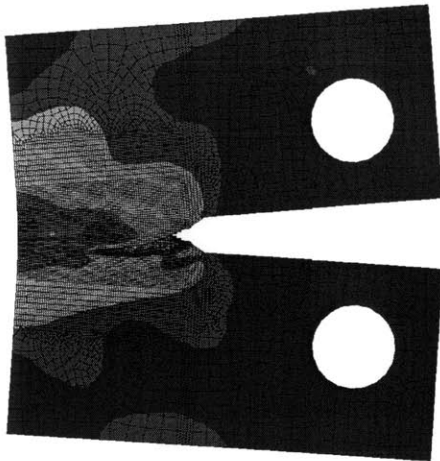
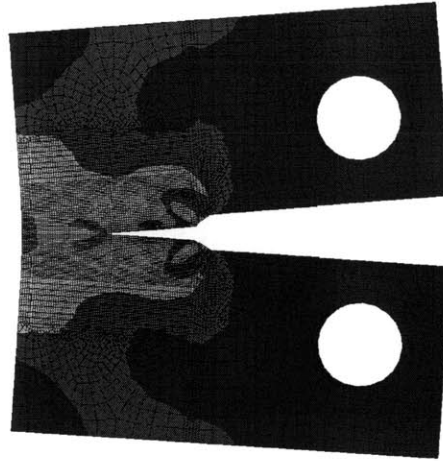


Figure 11.21: The geometry configuration of the compact tension specimen.

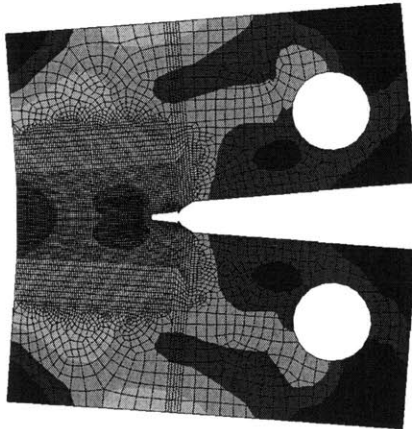
To study the effect of the Lode angle and the weakening effect separately, we predict the fracture mode using the four combinations of with/without the material weakening and/or the Lode angle dependence. For the runs with material deterioration, the calibrated matrix stress-strain curve is used; for non-deterioration runs, the true stress-strain curve is the input. The fracture modes for each case are shown in Fig. 11.22. The compact tension specimen was loaded by two 0.5 inch diameter frictionless pins moving in opposite direction.



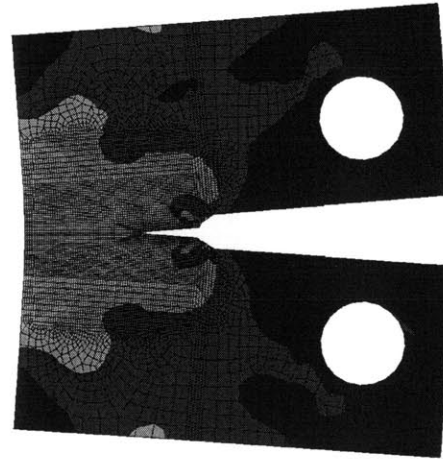
(a) w/ Lode and w/ weakening



(b) w/ Lode and w/o weakening



(c) w/o Lode and w/ weakening



(d) w/o Lode and w/o weakening

Figure 11.22: The fracture modes of a compact tension specimen for the four cases. The von Mises equivalent stress contours are plotted.

The generally experimentally observed results regarding the slant or flat crack in a compact tension specimen is that a higher strain hardening capability tends to promote a flat crack while a low strain hardening capability tends to promote a slant crack [115; 116]. For instance, Asserin-Lebert *et al.* shows the same Al 6056 alloy exhibits a slant profile in the age hardened heat treated condition T751 ($\sigma_{y0} = 300MPa, n \approx 0.06$) but a flat fracture mode in the annealed state ($\sigma_{y0} = 70MPa, n \approx 0.2$) [115].

In the present study, we use the damage plasticity model and fix other material parameters and a series simulation is conducted by changing the strain hardening exponent and the fracture strain ratio γ to examine their influence on the fracture mode. The simulated fracture modes are shown in Fig. 11.23, where a symbol “□” indicates a flat fracture mode and a symbol “△” indicates a slant fracture mode.

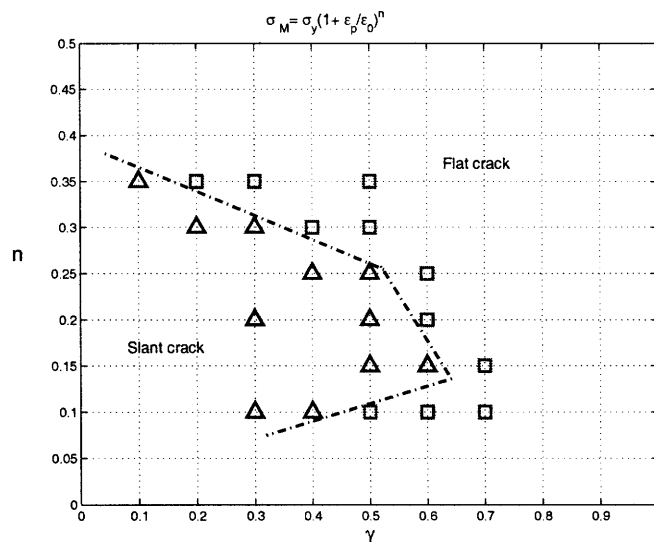


Figure 11.23: Fracture mode found in the simulation for various n and γ combinations.

The material parameters other than n and γ used to generate Fig. 11.23 are listed in Table 11.1.

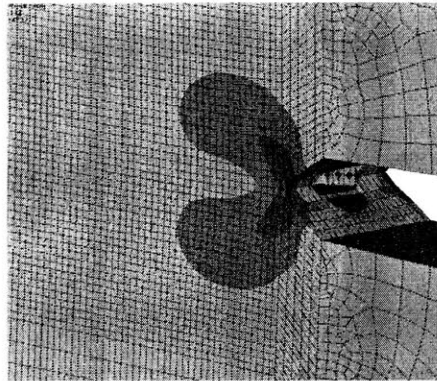
Table 11.1: Fixed material parameters in study of n and γ relationship.

σ_y	ϵ_k	ϵ_{f0}	p_{lim}	q	m	β
300 MPa	0.005	0.8	1000 MPa	1.0	2.0	2.0

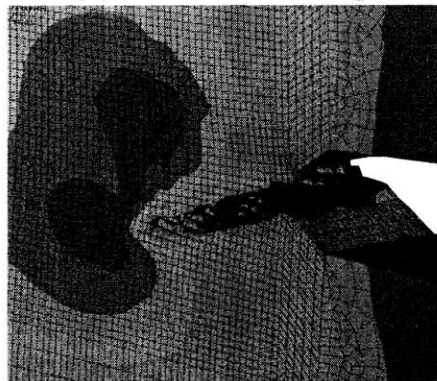
A transition from slant fracture mode to a flat fracture mode is observed from low n and low γ to high n and high γ zone except for n less than 0.15. This transition is shown in Fig. 11.23 approximately by dash-dot line. This agrees with the general experimental observation by a number of researchers.

Compact tension tests of aluminum alloy 2024-T351 were carried out by Mahmoud and Lease [99].

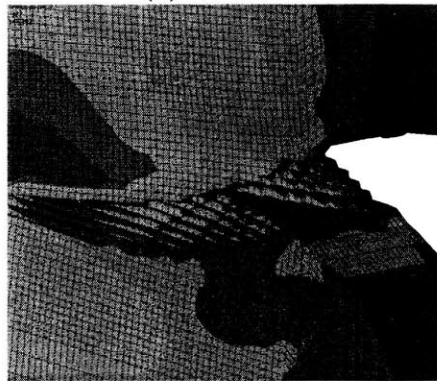
They tested larger panel with the same thickness as in the present paper and found a slant fracture mode for the 6.35mm thick specimen. From the simulation results, it is observed that only the simulation which considers both the material deterioration effect and the Lode angle dependence of fracture predicts the correct fracture mode. In the remaining three simulations, a flat fracture pattern is predicted. It is shown that the initial tunneling effect was captured by all four cases. A sequence of the crack-tip opening for the first case is shown in Fig. 11.24. It is also found that the crack propagates slower for cases without the Lode angle dependence (c) and (d) than those with Lode angle dependence (a) and (b). This is due to inadequate characterization of the lower ductility in the generalized shear condition.



(a) initial flat tunneling



(b) transition



(c) slant crack propagation

Figure 11.24: The time sequence of the flat tunneling, transition from flat to slant crack and the slant crack propagation. Plotted is the von Mises equivalent stress.

It is noteworthy that the mesh along the crack path was slightly skewed in the thickness direction, as shown in Fig. 11.25. This treatment is necessary because a trial calculation with a

symmetric mesh showed a symmetric “X” shaped crack developed due to the symmetry in the vertical direction. In the finite element model, the skewed mesh is designed such that a 9% difference in the element size at the two surfaces is introduced. The same mesh is used in all four runs.

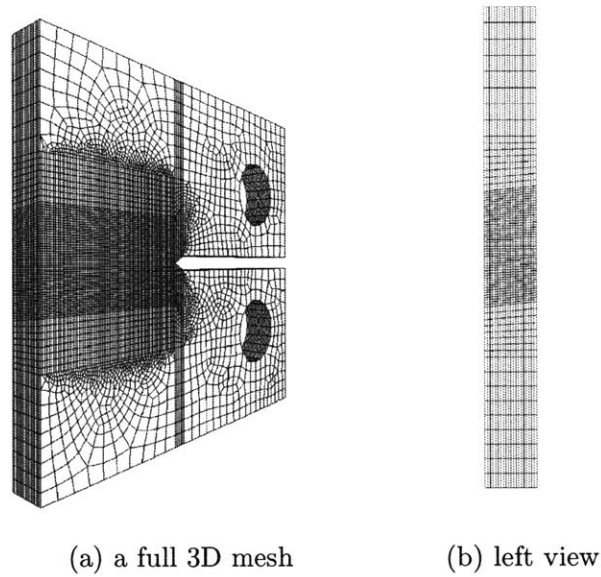


Figure 11.25: The initial mesh and a left view showing the skew of mesh in the thickness direction.

The load-displacement curves for the four cases are plotted in Fig. 11.26. The shape of the curves from models considering the material weakening agrees well with the experimental curves [99]. A sharp drop in loading at the initiation of fracture for the two cases that ignore the material weakening effect is not observed in the experiments [99].

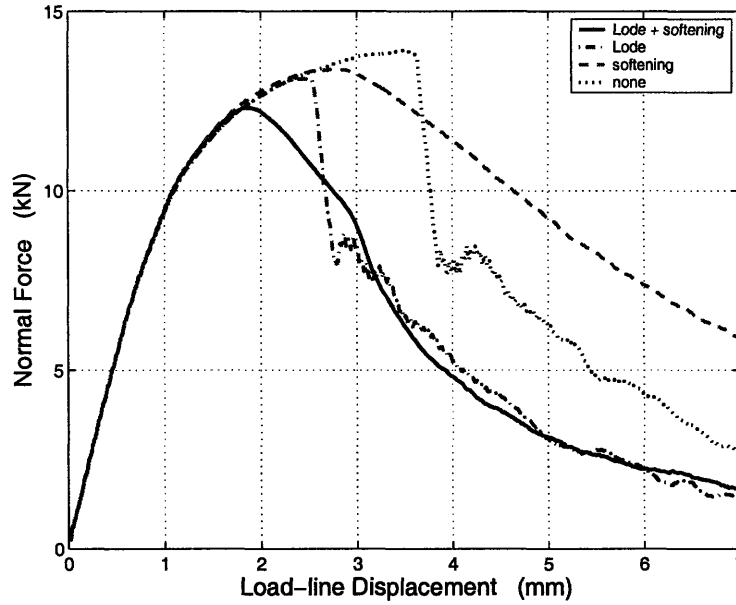


Figure 11.26: Comparison of the normal load versus load-line displacement curve for the four cases.

In summary, the numerical simulation results show that both the Lode angle dependence and the material weakening play vital roles in predicting a slant fracture in compact tension specimen. The synergistic effect of the two makes the transition from a flat crack to a slant crack possible.

11.4.2 Mahmoud and Lease's experiment

Compact tension tests of the aluminum alloy 2024-T351 was carried out by Mahmoud and Lease [99]. They tested large panels with the several different thicknesses and found a slant fracture mode for specimens with 2.3, 6.35 and 12.7mm thickness. The specimen is designed according to ASTM E399 with width $W = 203\text{mm}$ and a crack length to specimen width ratio $a/W = 0.4$. Here, we model the 6.35mm-thick CT plate. The simulation was carried out using the new damage plasticity material model. Element deletion method was used to model the crack. Due to the three-dimensional nature at the crack tip, the CT specimen is modeled by 8-node brick elements throughout. The displacement boundary conditions remote from the crack tip are applied through the contact of frictionless cylindrical pins with the two holes. The initial fatigue crack is not modeled though the geometry of the CT specimen, but the original chevron starter notch is replaced by a straight-through notch, since in general the fatigue crack is flat. The angle of the notch is 60° . The region

ahead of the pre-crack is discretized using 0.45x0.50x0.50mm (WxLxH) elements.

A realistic fracture mode is depicted in the finite element solution, as shown in Fig. 11.27. The element near the mid plane failed first. The initial crack propagation shows a flat tunneling which indicates strong pressure dependence due to the build-up of constraints in the thickness direction. The transition of flat-to-slant starts almost immediately when the central tunnel reaches the outer surfaces. Two shear lips form in the opposite direction and grow toward each other, which form a triangular flat tunneling zone. At the end of this triangular zone, the two shear lips merge and the fracture surface becomes one slant surface.

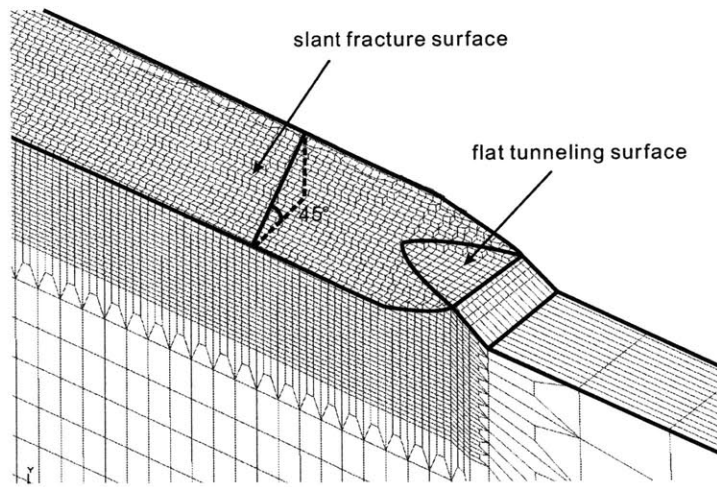


Figure 11.27: The fracture surface of the compact tension specimen shows the initial tunneling that followed by a slant mode.

The external load is plotted in Fig. 11.28 versus the crack extension at the mid plane and at surface. It is noticed that the numerical result of the load is steeper at the initial loading phase. Partially, this is because the fatigue crack ahead of the crack tip in the physical tests is neglected in the finite element model. It is found that the predicted initiation stage of the crack in the compact tension specimen is noticeably large than the experimentally observed load. This is due to the fatigue crack prior to the monotonic loading on the specimen, while in the simulation, the material ahead of the pre-crack tip is intact. Beyond the crack initiation stage, the predicted the load-crack extension curve is found to be in fairly good agreement with the experimental data [99].

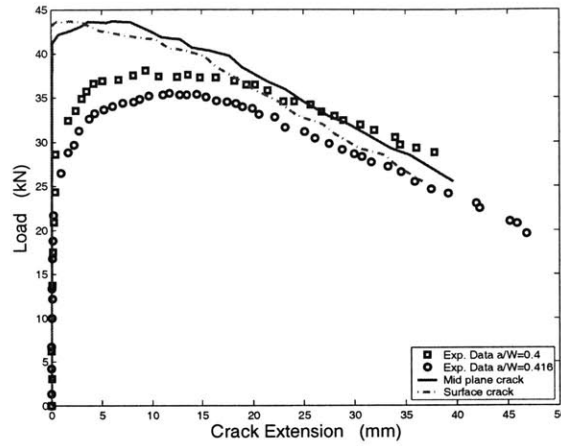
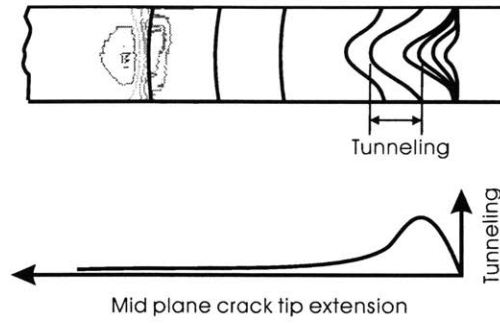
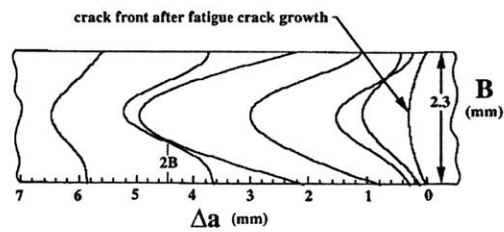


Figure 11.28: Comparison of the simulation and the experimental normal load versus load-line displacement curves.

As the fracture turns progressively to a slant mode, the extent of tunneling effect reduces. Figure 11.29 shows the crack front in a top view. The extent of tunneling peaks at about 4.1mm at mid plane crack extension to about 4.5mm. Then, the tunneling stabilized at about 1mm after the crack changes to a slant mode. Similar behavior of tunneling effect in the 2.3mm thick compact tension is shown in Fig. 11.29(b) [98].



(a) Top view of the crack fronts from simulation. Plotted contours are the stress component in the loading direction.



(b) Experimentally observed crack fronts from Dawicke *et al* [98].

Figure 11.29: The crack front in the top view of a compact tension specimen clearly shows the change of the extent of tunneling.

Sutton *et al* [117] showed that the tunneling in the flat crack propagation is more significant than in the slant crack propagation, as shown in Fig. 11.30. Because of the asymmetry of the crack shape, the through thickness hydrostatic tension can build up like in the symmetric flat crack propagation. The tunneling is largely due to this hydrostatic tension. We use the ratio of the difference in the crack length on the mid plane and on the outer surface with respect to the specimen thickness to denote the extent of tunneling.

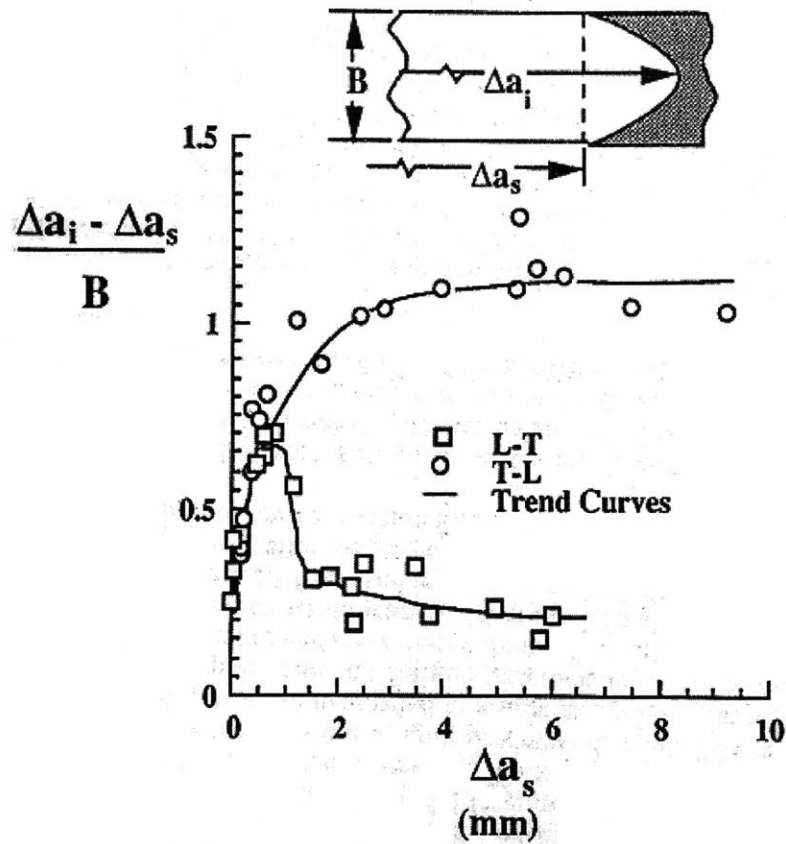


Figure 11.30: The tunneling in the flat crack propagation is more significant than in the slant crack propagation. After Sutton *et al* [117].

By setting the Lode angle function to unity, the crack propagation becomes flat. The difference of the tunneling in the flat crack and slant crack propagation in these two simulation situations is shown in Fig. 11.31. The tunneling in flat crack stabilizes after an initial increase. On the other hand, the slant crack shows

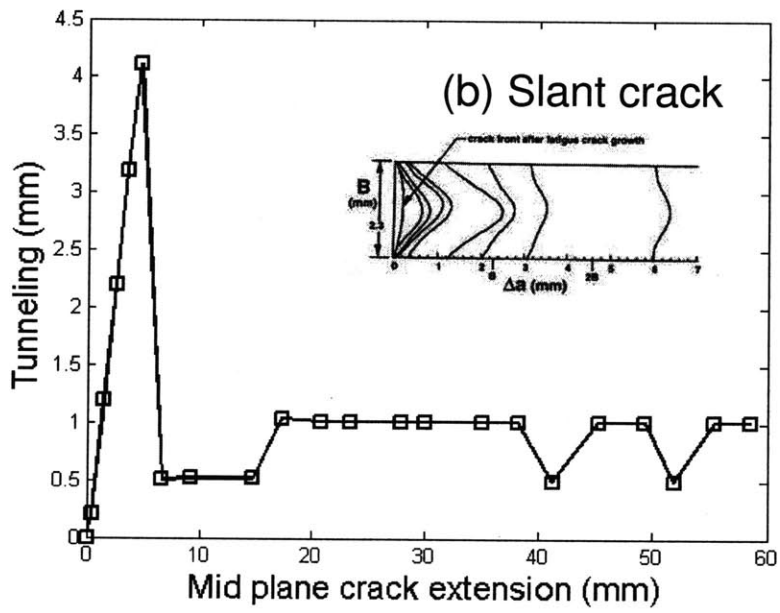
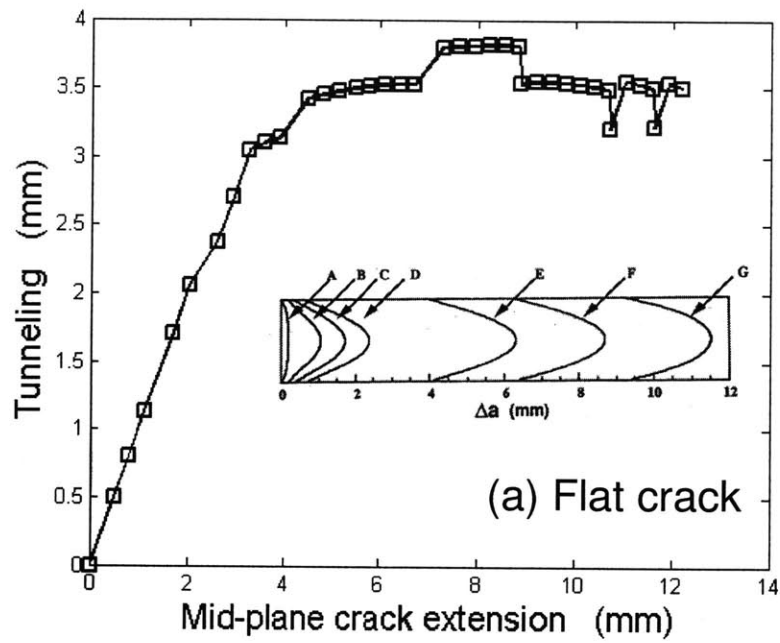


Figure 11.31: Simulation results show more significant tunneling in flat crack than in slant crack propagation.

11.5 Cup-cone fracture of a round bar

The following three simulation, i.e. (1) cup-cone fracture of a round bar, (2) doubly grooved flat plate and (3) dog-bone flat tensile specimen, were done prior to the full calibration of the material constants of aluminum alloy 2024-T351. We show this results for a demonstration of the crack pattern and damage pattern only. The material parameters used in these three simulations are:

Table 11.2: A set of material parameters used in the simulations.

ε_{f0}	p_{lim}	q	γ	m	β
0.7	926 MPa	1.75	0.4	1.73	1.0

The uniaxial tension of a smooth round bar is often used as a standard test to determine the material strength. For ductile metals, the specimen usually forms a localized neck before final fracture occurs. Careful examination of the microstructure at the neck reveals that the fracture starts at the center of the neck and propagates towards the free outer surface. The initial crack is in tensile mode and is perpendicular to the loading direction. The crack propagates until a large shear lip occurs [118; 119]. A “cup-cone” shaped fracture surface is thus formed.

The numerical calculation shows a realistic “cup-cone” fracture mode as shown in Fig. 11.32. Similar results were obtained by Tvergaard and Needleman[49] and Besson *et al.* [120] using Gurson-like model [16] and more recently by Scheider and Brocks [121] using cohesive model. In the present study, the proposed damage plasticity model is applied. The simulation is performed using axisymmetric brick elements. The un-notched round bar has a diameter of 9mm and is discretized using 0.1mm by 0.1mm elements at the middle section. The crack propagation is shown in Fig. 11.32.

Chapter 12

Microscopic Approach to Fracture - A Modified Gurson Model

The Gurson-like material model has attracted a great deal of attention and various modifications to this model have been proposed. The solid is considered as a porous medium and the constitutive equations are governed by the first and second stress invariants and the void volume fraction internal variable. One of the most important improvements to this model was made by Tvergaard and Needleman, who extended the void-nucleation-growth-coalescence in a phenomenological way [48; 49]. Meanwhile, little attention was given to the dependence of the damage evolution on the third stress invariant. On the other hand, McClintock proposed damage model based on the void evolution in localized shear band [132]. In the present paper, the GTN model is further extended to incorporate the void shearing mechanism. A new internal damage variable is introduced to describe not only the void volume fraction but also the damage associated with void shearing. Numerical aspects are addressed concerning the integration of the constitutive relations. The present model is implemented into the existing finite element code and numerical simulations have been performed. Two examples illustrate the predictive performance of the modified model in this chapter.

12.1 Introduction

The damage evolution and fracture criteria can be either based on the macroscopic state variables [10; 22; 133] or on the micro-mechanism [16; 17; 19]. The macroscopic description of damage

is obtained from external observation, such as the reduction of the fracture strain; while the microscopic description uses internal state variable determined from microstructure or meso-scale cell structure to quantify the deterioration of material. In the present chapter, we extend the Gurson model to include the dependence on the Lode angle. This extension is largely based on the void shearing mechanism [132].

From a microscopic point of view, the continuum constitutive law breaks down at a level of a porous media, which can be a result of voids nucleation and growth in plastically deformed solids. The first step to describe the mechanical behavior of a voided solids was made by McClintock [17] and Rice and Tracey [19]. Thereafter, there have been continuous efforts to modify the solution to be more accurate and realistic in capturing various aspects of the void controlled fracture. There is a wealth of publications which discuss the constitutive and numerical aspects of the voided material model. It is not the attempt of the current thesis to list the exhaustive development. Rather, we focus on the modeling of the void shearing effect and the Lode angle dependence of fracture prediction.

Probably, one of the most referenced void-nucleation-growth-coalescence models is the so-called Gurson-Tvergaard-Needleman (GTN) model. Gurson developed a pressure dependent approximate solution for yielding of a porous material [16]. Tvergaard and Needleman extended Gurson's solution in the quantitative aspects of fracture criterion and the void nucleation function [48] and [49]. The numerical implementation of this extended model has been extensively studied [134; 135] and utilized to capture some distinctive features in axisymmetric tensile failure and transverse plane strain fracture [49; 52].

From the analysis of the void shear mechanism, it is found that an initially spherical void become spheroidal and the free surfaces of voids move closer to the boundary of the void containing cell. An additional "*artificial strain*" is constructed to quantify the associated damage of void shearing. This portion of damage is missing in the original Gurson type of constitutive model because the material volume is conservative under simple shear due to the lack of hydrostatic pressure change. In a more complex loading case of combined tension and shear, a heuristic model based on the Lode angle is proposed to incorporate the void shearing damage. In this way, the third stress invariant is included in the constitutive model.

12.2 Yield function

The original yield function for porous media derived by Gurson [16] was modified by Tvergaard [48] to include the void coalescence effect. The modified yield function is

$$\Phi = \frac{\sigma_{\text{eq}}^2}{\sigma_{\text{M}}^2} + 2q_1 f^* \cosh \left\{ \frac{3q_2 \sigma_{\text{m}}}{2\sigma_{\text{M}}} \right\} - [1 + (q_1 f^*)^2] = 0, \quad (12.1)$$

where $q_1 = q_2 = 1$ for the spherically symmetrical deformation. Tvergaard [48] found that the set of parameters $q_1 = 1.5$ and $q_2 = 1$ yields to improved results. The void volume function f^* is defined as

$$f^*(f) = \begin{cases} f, & \text{for } f \leq f_c \\ f_c + \frac{1/q_1 - f_c}{f_f - f_c} (f - f_c) & \text{for } f_c \leq f \leq f_f \end{cases} \quad (12.2)$$

where f_c and f_f are the critical void fraction and the void volume fraction at fracture. The void coalescence is considered to take place when the void volume fraction reaches a critical value f_c and the material fractures when the void volume fraction reaches f_f . Despite it has been argued whether the void volume fraction is a constant for various loading cases, e.g. [136], the GTN model has achieved success in many applications [49].

From Eq. (12.1), the macroscopic strength of material depends on the matrix strength, the void volume fraction and the applied hydrostatic tension. The void volume fraction represents the associated damage to the solids. Equation (12.1) also includes a hydrostatic pressure dependence.

However, there are limitations when applying Gurson's model. Firstly, there is no shear consideration in this model. For instance, in pure shear, the growth rate of voids is zero due to constant zero pressure. If total volume fraction to be nucleated is less than the void volume fraction at fracture, then the material is predicted not to fail at all. Secondly, the theoretical work by Gurson shows such dependence in the positive range of mean stresses. However, due to the symmetry of the yield function with respect to zero mean stress, the Gurson model does not predict increase strength with respect to hydrostatic pressure.

12.3 Void coalescence

From metallographic observations, it is found that the nucleation, growth and coalescence of micro voids play an important role in the formation of cracks, see [53; 118; 119], and more recently [137]. When the voids grow so large that they begin to interact with another; the deformation becomes highly localized. This process is understood as “*void coalescence*”. In the cause of coalescence, the shape of individual void no longer regular and thus the Gurson’s solution breaks down. In general, such void linkage can occur at any orientations. In particular, the ligament between voids often breaks in two directions: (a) perpendicular to the loading directions and (b) in the localized shear direction [138]. The coalescence starts when the size of the voids and the ligament between voids becomes nearly equal [19; 23; 139].

In the generalized tension condition, the void growth usually dominates in the maximum principal loading direction and the ligaments between void experience higher hydrostatic tensions due to the quick loss of effective load carrying area. The reduction of cross-sectional area further exaggerates the void growth and coalescence. In a plane strain load condition, localized shear deformation dominates. It has been observed experimentally that void coalescence is dominated by a number of smaller voids in the inter-void ligament. This is called “*void sheeting*”. For some metals, there exist two size of void nucleation particles [140]. Palmer and Smith [141] showed that the smaller particles tend to nucleate at a larger strain. Within the neck of localized ligament, the equivalent plastic strain of the matrix material becomes so large that voids begin to form around the secondary void nucleation particles.

An example of the co-existence of the large void coalescence or small void sheeting is depicted by the uniaxial tensile failure of a round bar. McClintock showed there are three competing fracture mechanism in the tensile fracture of a round bar: (a) normal fracture; (b) shear fracture; (c) delamination fracture [142]. The normal fracture dominates at the center of the neck and the shear fracture dominates at the shear lip. The delamination failure is caused by the linkage of void parallel to the loading direction, which in this case remains incipient throughout the failure process.

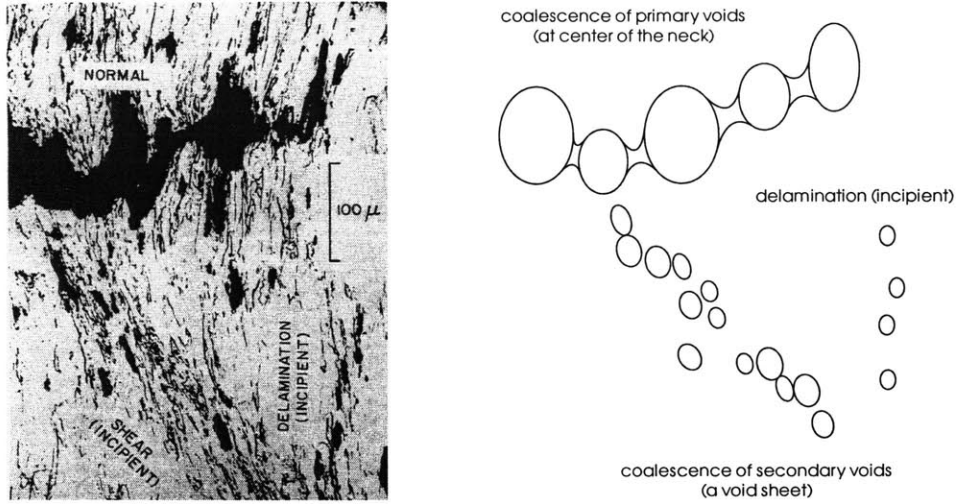


Figure 12.1: The competition of three fracture mechanisms. (left: actual crack and void, after Bluhm and Morrissey (1965) [142]; right: idealized void spacing and linkage.)

McClintock et al [132] related the damage associated with the coalescence in a localized shear band to Berg's viscous solution [50]. The void linkage in the shearing direction occurs when

$$\ln \left(\frac{L}{2R} \right) = \frac{\sqrt{3}\epsilon_{eq}}{2(1-n)} \sinh \frac{\sqrt{3}(1-n)\sigma_m}{\sigma_{eq}} + \ln \sqrt{1 + 3\epsilon_{eq}^2}, \quad (12.3)$$

where L is the void spacing in the shear direction, R is the initial void radius (see Fig. 12.2), n is the material strain hardening exponent. The first term in the right hand side of Eq. (12.3) represents the damage associated with the void growth and the second term represents the effect of rotation of the voids. It should be emphasized that the hydrostatic tension remains constant in simple shear and there is no macroscopic dilation. Therefore, the rotation of voids does not change the volume fraction, but an additive physical damage is caused by the void rotation. Therefore, "void sheeting" mechanism is more detrimental to the integrity of the material.

Tvergaard [143] considered the void coalescence to occur as the deformation localizes. A critical void volume fraction is proposed above which the coalescence starts. The difference between the micro-mechanism of large void coalescence and void sheeting is not taken into account.

The normal coalescence of large voids has a length scale of 10^{-4} m from Fig. 12.1 and it rapidly propagates across the cross-sectional area. This void coalescence is considered as the initiation of micro cracks, which is captured by the deletion of elements or separation of adjacent elements in

the finite element analysis. However, the void coalesce in a void sheet is in a progressive fashion due to the rotation and connection of smaller voids, as shown in Fig. 12.1.

It appears clearer that the void coalescence is not completely controlled by a critical value of the plastic strain of the matrix material or the void volume fraction. Rather the triaxial stress state and the loading history play important roles in the void coalescence. In the present paper, we extended the Gurson model to incorporate the Lode angle dependence of fracture by introducing the void shearing mechanism.

12.4 Void shearing mechanism

Considering a 2D problem, where a square cell having length L contains a cylindrical void of radius R at the center, when the cell structure is subjected to simple shear straining, the void elongates in the preferred direction, as shown in Fig. 12.2. Because the volume conservation of the cell structure, it is reasonable to assume the relative position of the void does not change with respect to the cell. The minimum distance between the free surface of the void and the boundary of the representative volume element decreases as the shear strain increases.

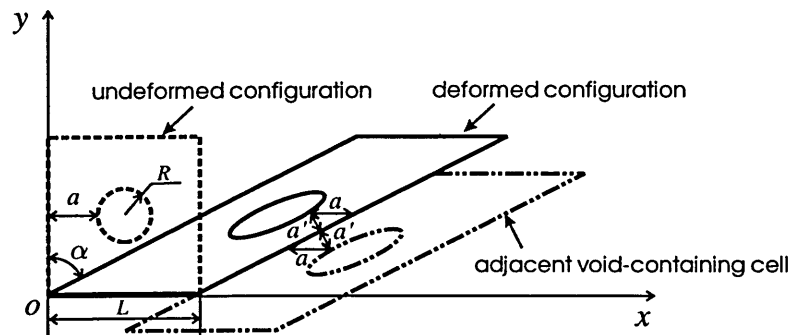


Figure 12.2: A schematic drawing illustrates the void shear mechanism.

Another example of void linkage due to shearing is given by Weck *et al.* [116; 144]. Two void arrangement is set for pulling and the failure mechanism show two distinct fracture model by internal necking and void shearing as shown in Fig. 12.3.

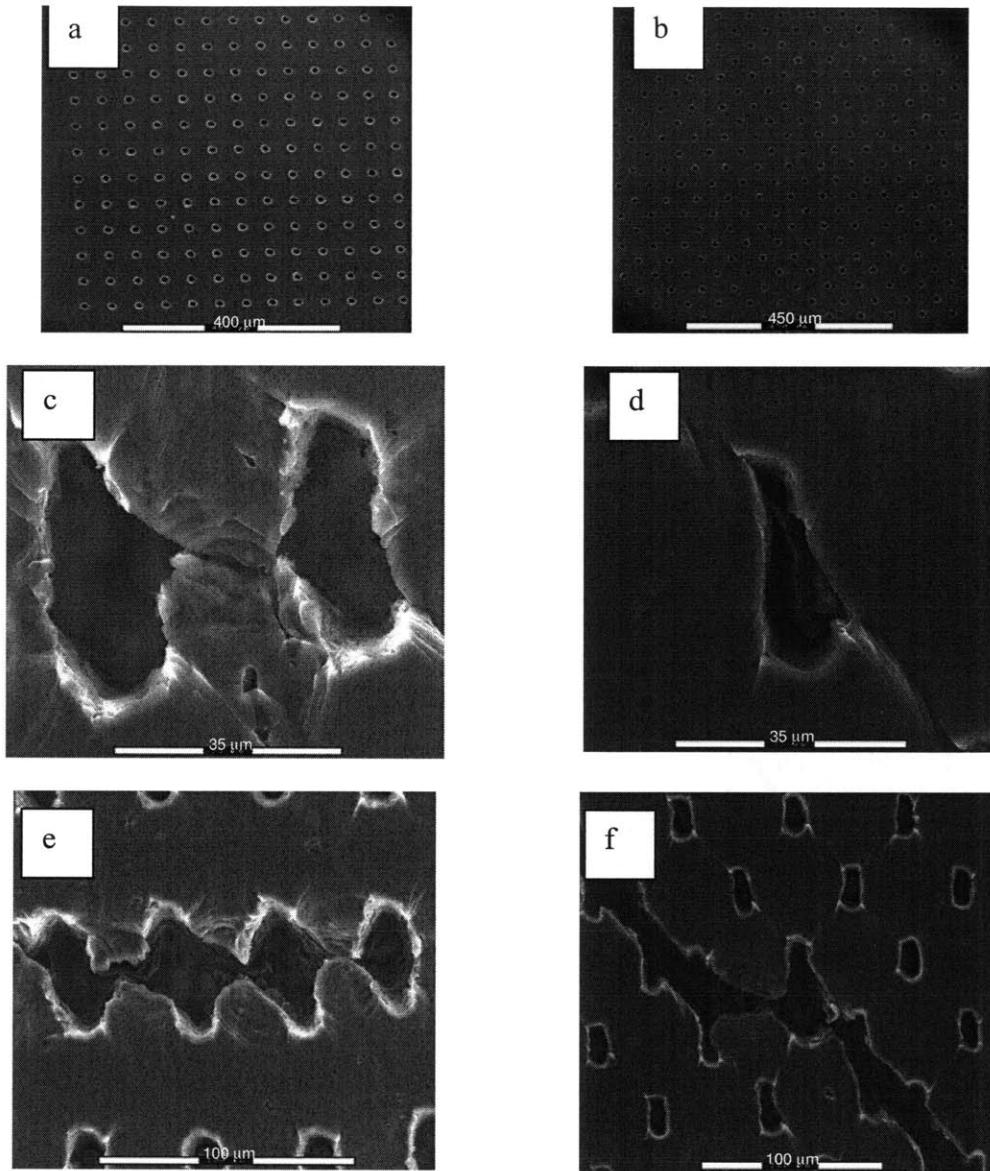


Figure 12.3: Two different failure mechanism: internal void necking and void shearing. From [116] (after Weck *et al.* [144]).

The initial minimum distance between the free surface of the void and the cell boundary is

$$a = \frac{L}{2} - R. \quad (12.4)$$

At a simple shear strain γ , we have

$$\tan \alpha = \gamma. \quad (12.5)$$

where α is the deformation angle shown in Fig. 12.2. The minimum distance at a deformed configuration becomes

$$a' = a \cos \alpha = a \sqrt{\frac{1}{1 + \gamma^2}}. \quad (12.6)$$

It should be noted that this minimum distance is not defined on two material points fixed with respect to the cell structure. Rather, the location of the corresponding material points are changing with the plastic flow. Using the logarithm definition of strain, we define an “artificial” strain associated with the reduction of the minimum distance

$$\varepsilon_{\text{rot}} = \log \frac{a}{a'} = \log \sqrt{1 + \gamma^2}. \quad (12.7)$$

For small γ , this strain reduces to

$$\varepsilon_{\text{rot}} = \frac{1}{2} \gamma^2. \quad (12.8)$$

Comparing this artificial strain with the maximum possible value at which the free surface of the void touches the boundary of the cell, the relative damage associated with the shearing of the void is

$$D_{\text{rot}} = \frac{\log \sqrt{1 + \gamma^2}}{\log \frac{L}{2R}}. \quad (12.9)$$

Using Taylor’s expansion, Eq. (12.9) can be approximated by the leading terms of the denominator and the numerator, i.e.

$$D_{\text{rot}} = \frac{\frac{1}{2} \gamma^2}{\sqrt{\frac{\pi}{4f}} - 1} \quad (12.10)$$

Knowing $\gamma = \sqrt{3} \varepsilon_{\text{eq}}$ for simple shear and for small void volume fractions, Eq. (12.10) can be approximately written as

$$D_{\text{rot}} = \frac{3}{\sqrt{\pi}} f^{(1/2)} \varepsilon_{\text{eq}}^2. \quad (12.11)$$

For the 3D case, similar relation can be obtained, i.e.

$$D_{\text{rot}} = \frac{3}{2} \left(\frac{6}{\pi} \right)^{(1/3)} f^{(1/3)} \varepsilon_{\text{eq}}^2 \quad (12.12)$$

Therefore, it is heuristic to represent the incremental void shear damage to be

$$dD_{\text{rot}} = q_3 f^{q_4} \varepsilon_{\text{eq}} d\varepsilon_{\text{eq}}, \quad (12.13)$$

where $q_3 = 1.69$ and $q_4 = 1/2$ for 2D or $q_3 = 1.86$ and $q_4 = 1/3$ for 3D problems respectively for the present idealized cell structure. For intermediate to large values of f ($f > 0.05$), the term “-1” neglected in the denominator of Eq. (12.10) becomes important and q_3 is too conservative. In the present study, we use the value of $q_3 = 3.0$ and $q_4 = 1/3$. Due to the complexity of the actual material structures, these constants are considered to be material dependent and can be calibrated by fitting experimental results.

Zhang et al [145] and Kim et al [146] conducted a numerical simulation using a single representative volume element (RVE). They determined the void coalescence from the drop of the load-displacement curve. However, only one RVE is used and the relative location with the neighboring element is not reflected. Therefore, the void shearing effect is not captured.

12.5 Lode angle dependent GTN model

The void shearing mechanism accelerates the damage accumulation when the material is subjected to a shear loading. Experimental observation also shows that many metals shows less ductility in shear than in tension at the same hydrostatic pressure level, e.g. [26; 40].

As the void grows to certain extent, the coalescence process begins. The microscopic straining within a cell structure becomes inhomogeneous. New voids tends to nucleate in the vicinity of the shortest ligaments between large voids, where deformation is highly localized. This facilitates the coalescence in the preferred direction, which is normal to the loading direction in this case. On the other hand, the void shear mechanism reduces the distance between the free surface of voids, which facilitates the linkage of voids in the shear direction. These two competing mechanisms co-exists in the neck of a tensile round bar, as illustrated by McClintock [17] (see Fig. 12.1).

In the numerical implementation, the initial condition of the cell at each time step is considered a single void at the center of the cell. During the deformation of the given time step, the void enlarges and new voids nucleate in the remaining matrix. At the end of the time step, an approximate “homogenization” process is performed, where the deformed cell is “homogenized” back to an enlarged single void cell structure [136]. This procedure is illustrated in Fig. 12.4 as the path (a)-(b)-(d).

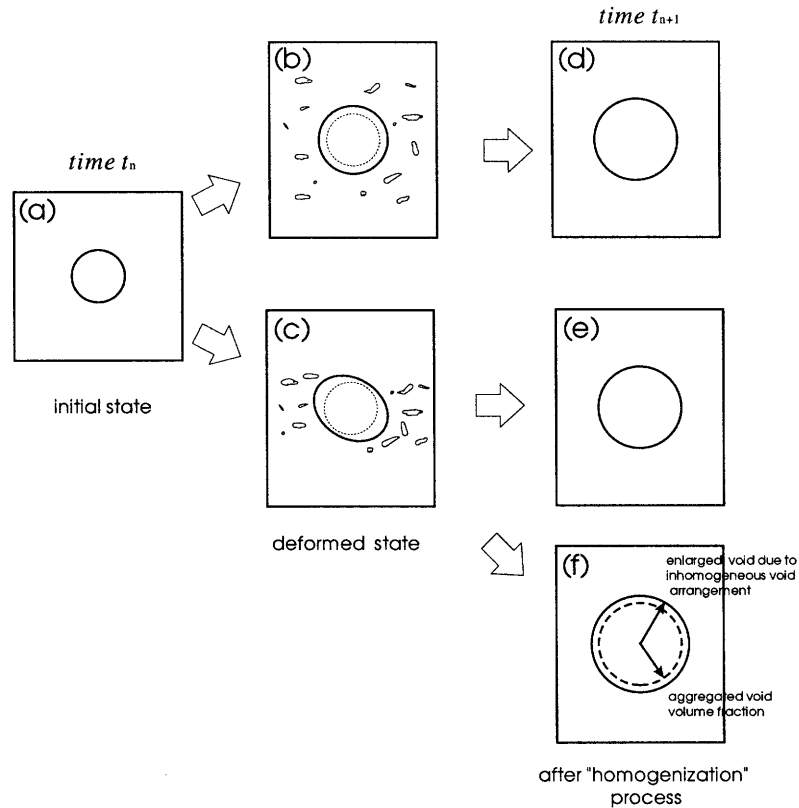


Figure 12.4: The approximate treatment of the nucleation and growth of voids at each time step.

There are at least two ways to incorporate this Lode angle dependence of fracture strain. One way is to consider the constitutive equations for the porous material remain the same as the GTN model, and introduce a separate state variable, i.e. a damage counter, to predict the onset of fracture. This is illustrated by the path (a)-(c)-(e), in which the damage variable D is not related to the constitutive equation. The other is to revise the constitutive equation to accommodate the new damage variable. This is illustrated in Fig. 12.4 as path (a)-(c)-(f), in which the damage is used to replace the void volume fraction function f^* in the GTN model.

Equation (12.13) is obtained for simple shear situation. For arbitrary loading case, the damage relationship becomes complicated. The deviatoric state has to be considered. In this regards, a Lode angle function g_θ is assumed to represent the azimuthal dependence. Equation (12.13) is rephrased as

$$dD_{\text{rot}} = q_3 f^{q_4} g_\theta \varepsilon_{\text{eq}} d\varepsilon_{\text{eq}}, \quad (12.14)$$

where the end conditions of $g_\theta = 0$ for generalized tension and $g_\theta = 1$ for the generalized shear condition have to be satisfied. One of such function can be

$$g_\theta = 1 - \frac{6|\theta_L|}{\pi}, \quad (12.15)$$

where θ_L is the Lode angle [5], which is defined as

$$\theta_L = \tan^{-1} \left\{ \frac{1}{\sqrt{3}} \left[2 \left(\frac{s_2 - s_3}{s_1 - s_3} \right) - 1 \right] \right\}. \quad (12.16)$$

where s_1 , s_2 and s_3 are the principal stress deviators.

In the GTN model, the damage is represented by the void volume fraction. However, studies have shown that the void volume fraction is not a constant at fracture [138; 147]. With the introduction of the “artificial strain” from the void shearing mechanism, a new internal state variable, the so-called “damage” is used to represent the actual deterioration of materials from plasticity damage in the Gurson type of constitutive model. The separation of damage from the void volume fraction allows further development to include other material defects such as the micro cracks.

Together with the reduction of cell walls, the minor axis of the cell also decreases. The free surface of the voids can touch the void nucleating particles, which are presumably rigid. In this case, a “void shear locking” occurs. Fleck *et al* [148] discussed the softening of particle enclosed voids. They found the softening could be reduced by a factor of two at zero mean stress. The radial locking and axial locking of voids is also discussed recently by and Siruguet and Leblond [149]. They found that the void grows faster at low stress triaxiality with the enclosed inclusions. In the present paper, this effect is neglected and the void is considered empty.

A comparison of the damage evolution in the GTN model and the present model is shown

in Fig. 12.5. The damage evolution from an arbitrary loading path is shown in Fig. 12.5(b). The portion of damage associated with void nucleation and growth and from the void shearing is graphically illustrated. The fracture occurs when the damage reaches unity.

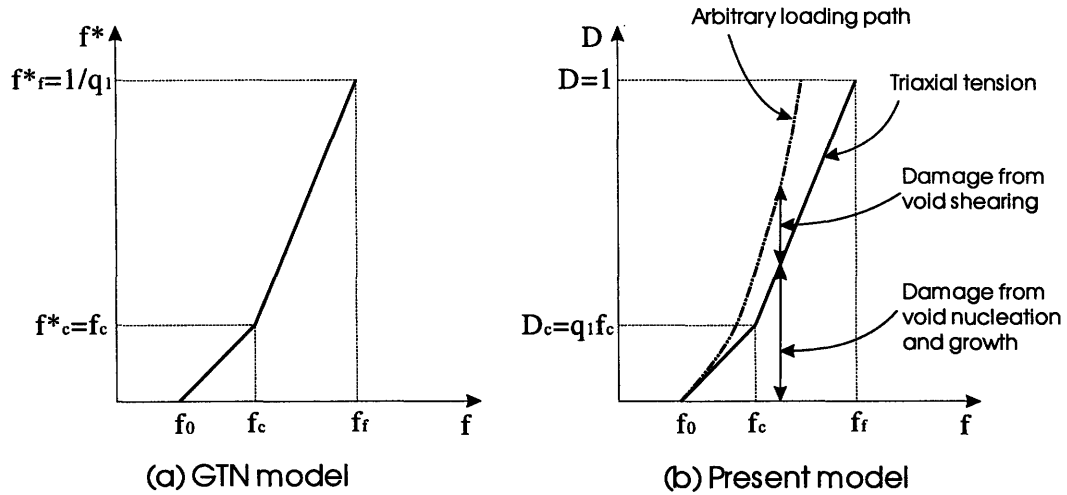


Figure 12.5: The void volume fraction of the GTN model and the damage evolution in the present model.

12.6 Fracture criterion

The Gurson model uses a critical void volume fraction at fracture as the fracture criterion. A fundamental question is whether the volume fraction of void at fracture is constant for different loading conditions. This issue has been numerically analyzed by various groups using unit-cell models [138; 147]. It becomes evident that the volume fraction of voids is not sufficient to describe the fracture.

Due to the loading history dependence of the fracture initiation, the evolution of the damage is described in a rate form of

$$dD^* = K_D (q_1 df + dD_{rot}), \quad (12.17)$$

where K_D is the damage rate coefficient. The damage evolution accelerates as the damage reaches a critical value D_c to characterize the void coalescence process. Comparing with the original form of GTN model, we found

$$K_D = \begin{cases} 1 & \text{for } D^* \leq D_c \\ \frac{1/q_1 - f_c}{f_f - f_c} & \text{for } D_c < D^* \leq 1. \end{cases} \quad (12.18)$$

where f_f and f_c are the void volume fraction at fracture and the critical void volume fraction at uniaxial tension and $D_c = q_1 f_c$. Therefore, in the case of uniaxial tension, the present model degenerates to the original GTN model, where $g_\theta = 0$ and the dD_{rot} disappears in Eq. (12.17).

Methods 1: Damage counter

Retaining the yield function of the GTN model, i.e. Eq. (12.1), we introduce the damage D as a third internal state variable besides the plastic strain and the void volume fraction. The onset of fracture is predicted when the damage reaches unity and the material is considered to fracture. In the finite element analysis, the element is removed and all stress components are set to zero. Using this method, the original stress integration is not changed. However, the actual fracture point of the material is determined by the loading path, which is Lode dependent. For generalized tensile loading, the fracture and the complete loss of load carrying capacity occurs simultaneously. However, for all other cases, the fracture is a suddenly loss of load carrying capacity, which is reflected on the load-displacement curve as a sharp drop of the loading. In the case of plane strain loading, for example the simple shear, the damage evolution rate is the highest, which results in the lowest ductility at the same hydrostatic tension.

Method 2: Damage constitutive model

In method 1, the GTN yield function retains and the void shearing effect is only considered for fracture prediction. However, the accelerated void nucleation in the reduced ligament between voids also introduces material softening. In method 2, we incorporate the replace the volume fraction function f^* with the damage function D . Using the convention that the fracture occurs when the damage reaches unity and letting $q_1 f^* = D^*$, Eq. (12.1) can be re-written as

$$\Phi = \left(\frac{\sigma_{\text{eq}}}{\sigma_M} \right)^2 + 2D^* \cosh \left(\frac{3q_2 \sigma_m}{2\sigma_M} \right) - (1 + D^{*2}) = 0. \quad (12.19)$$

For pressure independent plastic material, at a reference state of constant zero pressure, the yield function reduces to

$$\Phi = \frac{\sigma_{\text{eq}}^2}{\sigma_M^2} - (1 - D^*)^2 = 0. \quad (12.20)$$

or,

$$\sigma_{\text{eq}} = (1 - D^*)\sigma_M, \quad (12.21)$$

which is the yield condition with weakening, e.g. [10].

As the damage accumulates towards unity, the yield surface shrinks towards the triaxial axis. The effect of damage and the hydrostatic tension on the yield stress is plotted on the normalized equivalent stress and mean stress plane, as shown in Fig. 12.6.

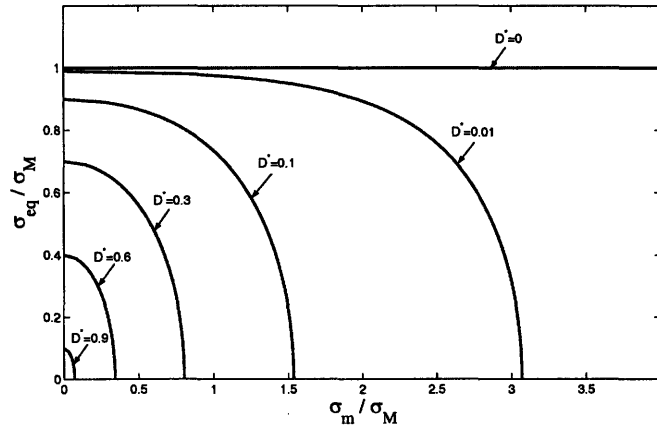


Figure 12.6: The Gurson yield surface depends on the mean stress and the damage.

It should be emphasized that at any damage state the yield surface of the modified GTN model is a spheroidal in the principal stress space, which is similar to that of the GTN model. However, the size of that spheroid is Lode angle dependent. The plane strain $\theta_L = 0$ provides the least ductile case and, therefore, the size of the spheroid shrinks most quickly. On the other hand, because of the axisymmetry, the void shearing effect is absent in generalized tension. Thus, the damage is minimum and the size of the spheroidal is the largest.

12.7 Numerical implementation

In the pressure dependent constitutive model, the equivalent stress and the mean stress are two independent variables. Aravas [134] proposed a general backward Euler procedure for the pressure dependent plasticity. A detailed derivation can also be found in Simonsen and Li [135]. Forward Euler procedure is proposed by Worswick and Pelletier [150]. In the present chapter, we use the backward Euler stress integration throughout the calculations.

The first method uses the damage as a fracture predictor only. Therefore, the stress integration procedure does not change. For the second method, a new state variable D is encountered and the evolution function is a function of the Lode angle θ_L .

The consistency requires

$$\dot{\Phi} = 0. \quad (12.22)$$

Knowing the yield function at time t^n is zero, Eq. (12.22) yields

$$\Phi^n (\sigma_m^{n+1}, \sigma_{eq}^{n+1}, D^{n+1}, \sigma_M^{n+1}) = 0, \quad (12.23)$$

where the superscript n denotes the values at time step n .

From the flow rule (Eq. (2.29)), the dilatational strain and the equivalent plastic strain are

$$\dot{\epsilon}_m = \dot{\lambda} \left(\frac{\partial \Phi}{\partial \sigma_m} \right), \quad (12.24)$$

$$\dot{\epsilon}_{eq} = \dot{\lambda} \left(\frac{\partial \Phi}{\partial \sigma_{eq}} \right). \quad (12.25)$$

Eliminating $\dot{\lambda}$ from Eqs. (12.24) and (12.25), one obtains the constraint equation

$$F = \dot{\epsilon}_m \frac{\partial \Phi}{\partial \sigma_{eq}} - \dot{\epsilon}_{eq} \frac{\partial \Phi}{\partial \sigma_m} = 0. \quad (12.26)$$

At each time step, the prediction-correction algorithm is used. The trial stress is obtained from elastic update, in which the material is assumed to be purely elastic. In Gurson's model, no damage associated elastic modulus decrease is considered. If the yield function evaluated from the trial stress is greater than zero, a relaxation (correction) step follows. The incremental dilatational strain and the equivalent plastic strain are determined in the relaxation step where Eqs. (12.23)

and (12.26) are solved using Newton's method.

In the current methods, there are three internal state variables, namely ε_p , f and D which represent the matrix plastic strain, the void volume fraction and the damage. Of the three state variables, the matrix plastic strain ε_p and the damage D appear in the yield function. The void volume fraction is involved in the update of internal state.

At each iteration, the iterative variables are obtained by solving

$$\begin{bmatrix} K_{11} & K_{12} \\ K_{21} & K_{22} \end{bmatrix} \begin{bmatrix} d\dot{\varepsilon}_m^k \\ d\dot{\varepsilon}_{eq}^k \end{bmatrix} = \begin{bmatrix} -F^k \\ -\Phi^k \end{bmatrix} \quad (12.27)$$

where the superscript k denotes the k^{th} iteration and

$$\begin{aligned} K_{11} = \frac{\partial F}{\partial \dot{\varepsilon}_m} &= \frac{\partial \Phi}{\partial \sigma_{eq}} + \dot{\varepsilon}_m \left[(-\Delta t K) \frac{\partial^2 \Phi}{\partial \sigma_{eq} \partial \sigma_m} + \sum_{i=1}^3 \frac{\partial^2 \Phi}{\partial \sigma_{eq} \partial H_i} \frac{\partial H_i}{\partial \dot{\varepsilon}_m} \right] \\ &- \dot{\varepsilon}_{eq} \left[(-\Delta t K) \frac{\partial^2 \Phi}{\partial \sigma_m^2} + \sum_{i=1}^3 \frac{\partial^2 \Phi}{\partial \sigma_m \partial H_i} \frac{\partial H_i}{\partial \dot{\varepsilon}_m} \right] \end{aligned} \quad (12.28)$$

$$\begin{aligned} K_{12} = \frac{\partial F}{\partial \dot{\varepsilon}_{eq}} &= -\frac{\partial \Phi}{\partial \sigma_m} + \dot{\varepsilon}_m \left[(-3\Delta t G) \frac{\partial^2 \Phi}{\partial \sigma_{eq}^2} + \sum_{i=1}^3 \frac{\partial^2 \Phi}{\partial \sigma_{eq} \partial H_i} \frac{\partial H_i}{\partial \dot{\varepsilon}_{eq}} \right] \\ &- \dot{\varepsilon}_{eq} \left[(-3\Delta t G) \frac{\partial^2 \Phi}{\partial \sigma_m \partial \sigma_{eq}} + \sum_{i=1}^3 \frac{\partial^2 \Phi}{\partial \sigma_m \partial H_i} \frac{\partial H_i}{\partial \dot{\varepsilon}_{eq}} \right] \end{aligned} \quad (12.29)$$

$$K_{21} = \frac{\partial \Phi}{\partial \dot{\varepsilon}_m} = -\Delta t K \frac{\partial \Phi}{\partial \sigma_m} + \sum_{i=1}^3 \frac{\partial \Phi}{\partial H_i} \frac{\partial H_i}{\partial \dot{\varepsilon}_m}, \quad (12.30)$$

$$K_{22} = \frac{\partial \Phi}{\partial \dot{\varepsilon}_{eq}} = -3\Delta t G \frac{\partial \Phi}{\partial \sigma_{eq}} + \sum_{i=1}^3 \frac{\partial \Phi}{\partial H_i} \frac{\partial H_i}{\partial \dot{\varepsilon}_{eq}}. \quad (12.31)$$

The partial derivatives of the internal state variables ε^p and D with respect to $\dot{\varepsilon}_m$ and $\dot{\varepsilon}_{eq}$ in Eqs. (12.28) is obtained from their evolutionary equation. With the addition of dependence on the Lode angle, the general functional form for the evolution of internal state variable becomes

$$\dot{H}_i = h_i \left(\dot{\varepsilon}_m, \dot{\varepsilon}_{eq}, \sigma_m, \sigma_{eq}, \theta_L, H^\beta \right). \quad (12.32)$$

where H denotes the internal state variable (here, $H_1 = \varepsilon^p$ and $H_2 = D$), β is the total number of

internal state variables and $i = 1, 2, \dots, \beta$.

$$\frac{\partial H_i}{\partial \dot{\epsilon}_m} = \frac{\partial h_i}{\partial \dot{\epsilon}_m} + \frac{\partial h_i}{\partial \sigma_m} \frac{\partial \sigma_m}{\partial \dot{\epsilon}_m} + \frac{\partial h_i}{\partial \theta_L} \frac{\partial \theta_L}{\partial \dot{\epsilon}_m} + \sum_{j=1}^{\beta} \frac{\partial h_i}{\partial H_j} \frac{\partial H_j}{\partial \dot{\epsilon}_m} \quad (12.33)$$

$$\frac{\partial H_i}{\partial \dot{\epsilon}_{eq}} = \frac{\partial h_i}{\partial \dot{\epsilon}_{eq}} + \frac{\partial h_i}{\partial \sigma_{eq}} \frac{\partial \sigma_{eq}}{\partial \dot{\epsilon}_{eq}} + \frac{\partial h_i}{\partial \theta_L} \frac{\partial \theta_L}{\partial \dot{\epsilon}_{eq}} + \sum_{j=1}^{\beta} \frac{\partial h_i}{\partial H_j} \frac{\partial H_j}{\partial \dot{\epsilon}_{eq}} \quad (12.34)$$

The partial derivatives of internal variables with respect to the incremental dilatational strain and the equivalent strain are solved from Eqs. (12.33) and (12.34). The Lode angle dependence in the above equations are represented by the partial derivatives $\partial \theta_L / \partial \dot{\epsilon}_m$ and $\partial \theta_L / \partial \dot{\epsilon}_{eq}$. However, the flow rule, Eqs. (12.24) and (12.25), is independent on θ_L , which means

$$\frac{\partial \theta_L}{\partial \dot{\epsilon}_m} = 0, \quad \text{and} \quad \frac{\partial \theta_L}{\partial \dot{\epsilon}_{eq}} = 0. \quad (12.35)$$

Applying Eq. (12.35) to Eqs. (12.33) and (12.34), the introduction of the Lode angle dependence to the Gurson type model does not generate additional computational complexity in the stress integration except for the explicit expression in the update of internal variables.

The partial derivatives used above are listed in the Appendix.

12.8 Numerical simulation

The GTN model has been successful in predicting the classic ‘‘cup-cone’’ fracture mode and the transverse plane strain fracture [49; 120]. The success is due to several factors, which include: the void induced material softening and the strain controlled void nucleation function. However, there are also several drawbacks. For instance, the material parameters are highly coupled, which makes the calibration process difficult. Moreover, to determine the micro structure related values, a simple arithmetic average over the volume may not be adequate.

Another important issue is that the GTN can not predict shear fracture accurately, especially at low stress triaxiality. At high stress triaxiality, the void growth is more substantial; while at low stress triaxiality, the void growth is not significant and the void shearing effect has more contribution toward failure. In the present modified model, with the introduction of the void shear effect, the simple shear failure can be simulated. This can be demonstrated by using a simple

unit cell model. In addition to the unit cell model, simulations using the the uniaxial tension of a smooth round bar and the transverse plane strain also shows the similarities and the differences of the modified model with the original GTN model.

12.8.1 Unit cell

The mechanical behavior of the modified constitutive model and the proposed modification can be illustrated using a unit cell model. Two loading cases (a) uniaxial tension and (b) simple shear are used to demonstrate the difference between the current model and original GTN model. To allow the necking to occur in uniaxial tension, the cell is discretized by three equal size 8-node brick elements aligned in the x -direction, as shown in Fig. 12.7. The two facets in the YZ plane are loaded at a constant velocity in the X - and Y -direction, which represents uniaxial tension and simple shear condition. The thick arrows show the loading directions.

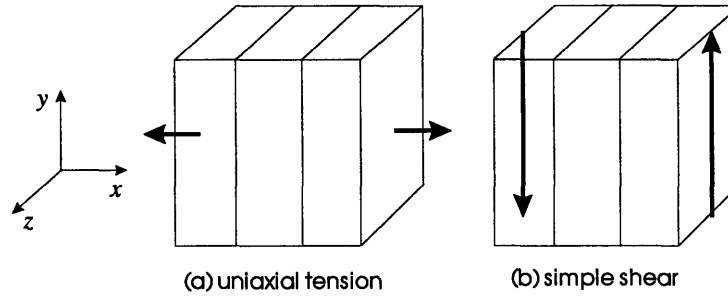


Figure 12.7: A three-element unit cell used to illustrate the modified GTN model.

The hardening properties of the matrix material are assumed to be governed by a piecewise power law relationship

$$\varepsilon = \begin{cases} \frac{\sigma}{E} & \text{for } \sigma \leq \sigma_y \\ \frac{\sigma_y}{E} \left(\frac{\sigma}{\sigma_y} \right)^{1/n} & \text{for } \sigma > \sigma_y \end{cases}, \quad (12.36)$$

where ε is the total strain, E is the Young's modulus, σ_y is the yield stress and n is the strain hardening exponent.

The matrix material hardening parameters are $E = 70GPa$, $\sigma_y = 231MPa$, $n = 0.1$ and $\nu = 0.3$. The material parameters related to the void nucleation and damage evolution are listed in Table 12.1.

Table 12.1: Material parameters for the modified GTN model.

variables:	q_1	q_2	q_3	q_4	f_0	f_c	f_F	f_N	ε_N	S_N
value	1.5	1.0	3.0	0.33	0.0	0.05	0.25	0.04	0.2	0.1

(a) Simple tension

In simple tension, the Lode angle is constant -30° and $g(\theta) = 0$. Therefore, the original GTN model, the damage counter and the damage yielding model are essentially the same. The numerical calculation predicts the same results as expected. See Fig. 12.8.

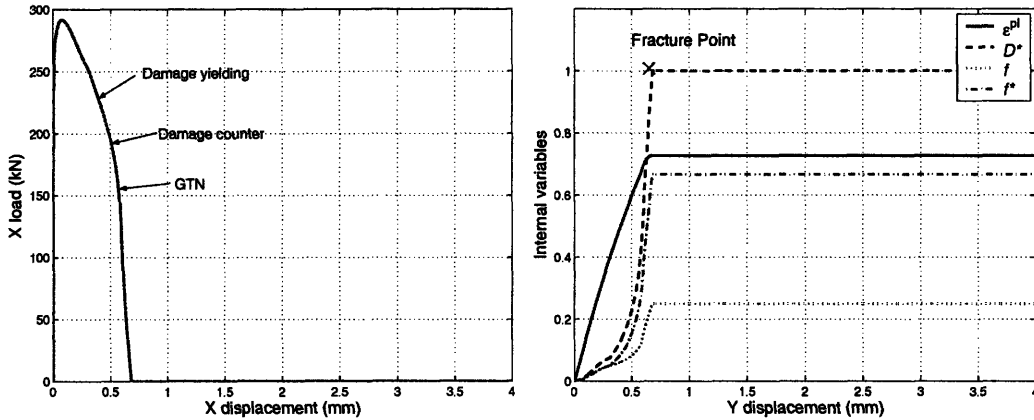


Figure 12.8: Comparison of the load-displacement curves and the internal state variables for the GTN, damage counter and damage yielding models in uniaxial tension.

(b) Simple shear

The simple shear is another limiting case, where the Lode angle is constant 0° and $g(\theta) = 1$. The differences of the original GTN model, the damage counter model and the damage yielding model can be fully observed in this example. The Y-direction load and the displacement curve for simple shear is shown in Fig. 12.9.

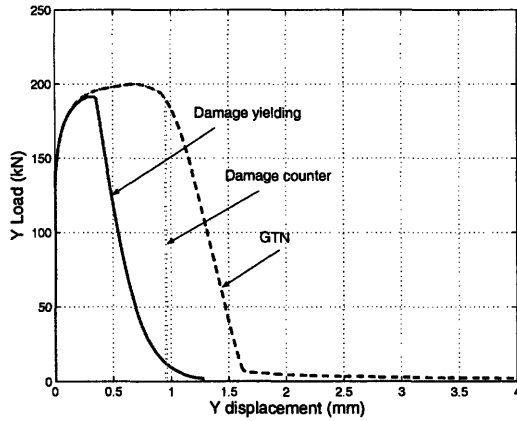


Figure 12.9: Comparison of the load-displacement curves for the GTN, damage counter and damage yielding models.

The GTN model does not predict a fracture and unrealistic shear deformation was observed. The damage counter and the damage yielding model both predict fracture at a realistic extent of deformation. The evolution of the internal variables for the three models are plotted in Figs. 12.10 to 12.12

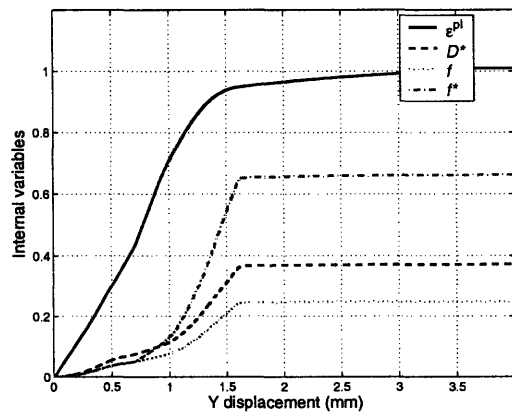


Figure 12.10: Internal variables for GTN model.

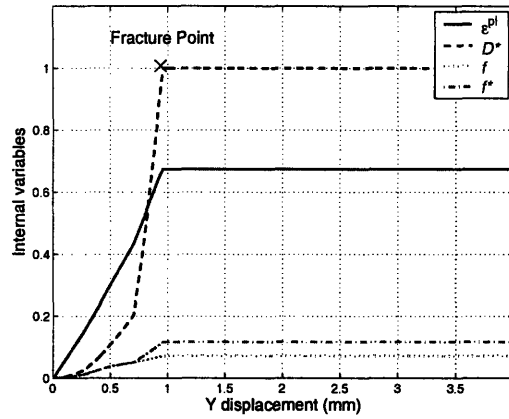


Figure 12.11: Internal variables for the damage counter GTN model.

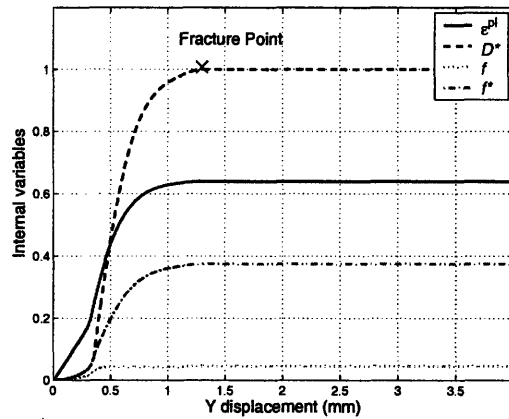


Figure 12.12: Internal variables for the damage yielding GTN model.

The comparison of the D^* in the GTN, damage counter and damage yielding models, as shown in Fig. 12.13. In the GTN model, the void shearing effect is completely ignored, thus, the accumulation rate is the lowest. In the damage counter model, the damage is integrated explicitly after the plasticity iteration, which results in an intermediate accumulation rate. In the damage yielding model, the feedback from accumulated damage exaggerates the softening process and, therefore, the damage accumulation rate is the largest.

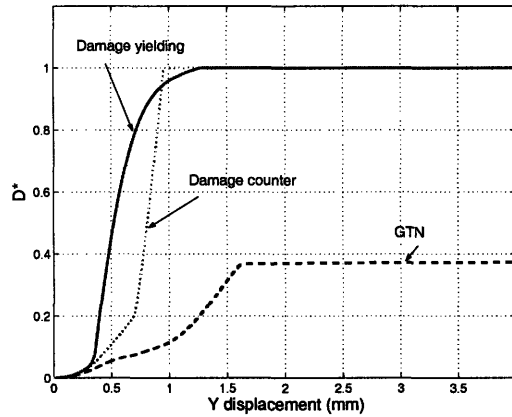


Figure 12.13: Comparison of the damage evolution in the GTN, damage counter and damage yielding model.

12.8.2 Uniaxial tension of a round bar

Uniaxial tension of a round bar is often used to study the void growth in metals [151]. For ductile metals, the material instability starts with forming a neck. It followed by the initiation of fracture at the center of the neck with linkage of adjacent voids due to high hydrostatic tension. The coalescence of voids usually form a zig-zag configuration this is globally perpendicular to the loading direction [119]. As the crack propagates towards the free surface, the last zig is large and forms a shear lip.

Besson *et al* [122] studied the plane strain tensile rupture using Gurson model and concluded that the use of f^* function favors flat fracture. With the introduction of the void shear mechanism, the region under shear slip undergoes more damaging than those in generalized tension under the same hydrostatic tension. Therefore, the void shear mechanism helps to form a shear lip in the cup-cone type of fracture.

The original mesh and the tensile cracks predicted by the original GTN model, the damage counter model and the damage yielding model are shown in Fig. 12.14.

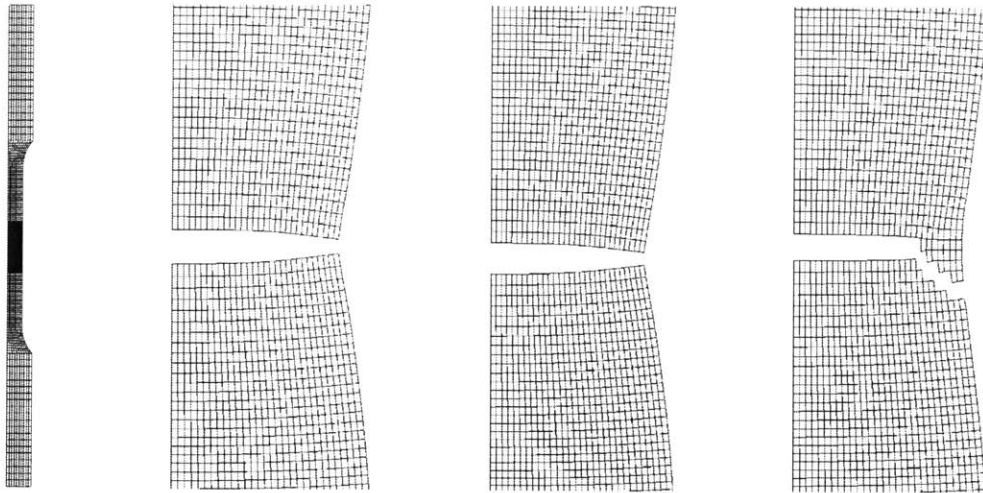


Figure 12.14: Tensile crack of a round bar predicted by three material models. left to right: (1) before test; (2) GTN; (3) Method 1; (4) Method 2.

A cup-and-cone failure mode is predicted using the modified yielding method. The original GTN model and the damage counter method predict a flat crack. The line contours of the deviatoric state variable $\chi = \frac{s_2 - s_3}{s_1 - s_3}$ is plotted in Fig. 12.15, which shows two shear bands occur ahead of the crack tip.

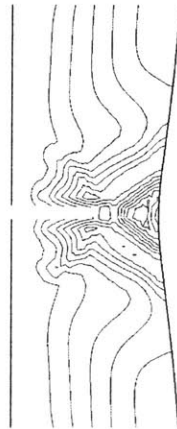


Figure 12.15: The line contours of the deviatoric state variable at the mode transition of the crack from tensile to shear.

12.8.3 Transverse plane strain tension

The transverse plane strain cracks predicted by the original GTN and the damage yielding models are both slant type of fracture, as shown in Fig. 12.16. The line contours of damage before crack occurs show two preferred directions of crack propagation, as illustrated in Fig. 12.17.

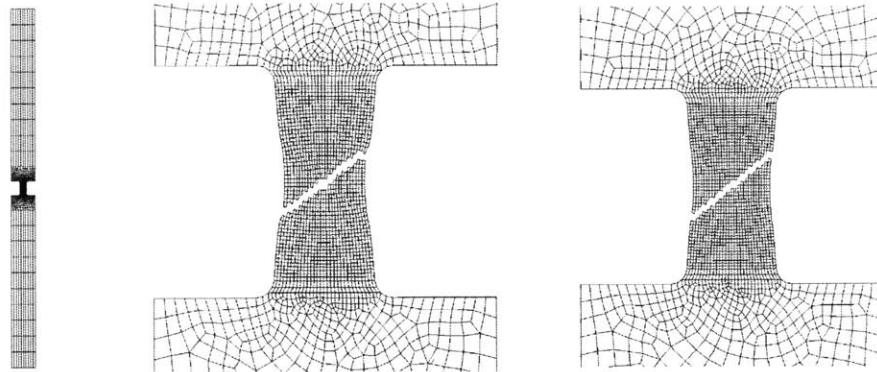


Figure 12.16: Transverse plane strain cracks predicted by three material models. left to right: (1) before test; (2) GTN; (3) Damage yielding method.

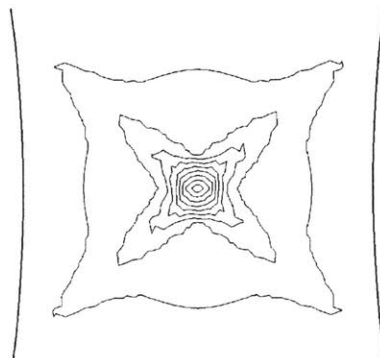


Figure 12.17: The line contours of the damage in gaged section of the doubly groove plate.

A careful examination of Fig. 12.16 reveals that the GTN model shows a deeper neck that the damage yielding model predicts. This can be more clearly shown by the load-displacement curves.

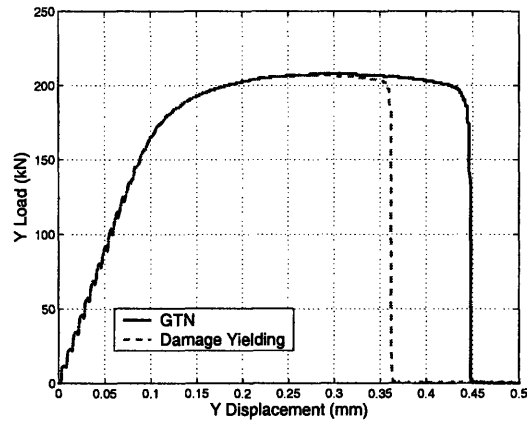


Figure 12.18: The line contours of the damage in gaged section of the doubly groove plate.

Due to the additional void shear damage, the damage yielding model predicts a lower ductility at the transverse plane strain condition than the original Lode angle independent GTN model.

12.9 Conclusions

Successful numerical prediction of fracture of specimen subjected to transverse plane strain and axisymmetric tension loading using Gurson model in the past three decades. The void volume fraction has been used as the damage indicator [49; 152]. It has been pointed out that the void volume fraction is not sufficient in characterizing the ductile fracture in complex loading conditions. The Lode angle dependence was modeled for damage accumulation and fracture initiation in the framework of continuum mechanics of solids. In the present chapter, the Gurson type of pressure dependent constitutive model is modified to include the Lode angle dependent damage in a heuristic way. The void shearing effect, which is missing previously, is incorporated in the Gurson model to describe the Lode angle dependence.

Two methods have been adopted (a) the damage counter and (b) the damage associative yielding model. The former describes the yielding based on the void volume fraction and predicts the onset of fracture using a separate damage indicator. Therefore, the fracture is a sudden drop in the load-displacement curve. The later considers the yielding directly from the damage indicator and the load carrying capacity drops smoothly. Both model are capable of predict the fracture in simple shear. The difference between these two models is a fundamental question, i.e. whether the yielding

and the plasticity damage are governed by the same set of internal state variables or two different sets. This question remains open and no attempt has been made in the present paper to answer this question.

Simulations of the axial tension of a round bar and the transverse plane strain condition are performed. The proposed model helps to predict a “cup-cone” type of fracture. In doubly grooved flat plate, the predicted fracture strain is less than predicted by GTN model.

Appendix

The yield function is

$$\Phi = \left(\frac{\sigma_{\text{eq}}}{\sigma_{\text{M}}} \right)^2 + 2D^* \cosh \left(\frac{3q_2 \sigma_{\text{m}}}{2\sigma_{\text{M}}} \right) - (1 + D^{*2}) \quad (12.37)$$

The three internal variables are

$$H_1 = \varepsilon^p \quad (12.38)$$

$$H_2 = f \quad (12.39)$$

$$H_3 = D. \quad (12.40)$$

The evolution of internal state variables are

$$\dot{H}_1 = h_1 = \frac{\sigma_{\text{m}} \dot{\varepsilon}_{\text{m}} + \sigma_{\text{eq}} \dot{\varepsilon}_{\text{eq}}}{(1-f)\sigma_{\text{M}}} \quad (12.41)$$

$$\dot{H}_2 = h_2 = (1-f)\dot{\varepsilon}_{\text{m}} + A_{\text{N}}\dot{\varepsilon}^p \quad (12.42)$$

$$\dot{H}_3 = h_3 = h_2 + q_3 f^{q_4} g(\theta) \varepsilon_{\text{eq}} \dot{\varepsilon}_{\text{eq}}. \quad (12.43)$$

The partial derivatives are

$$m_1 = \frac{\partial \Phi}{\partial \sigma_m} = \frac{3q_2 D^*}{\sigma_M} \sinh \left(\frac{3q_2 \sigma_m}{2\sigma_M} \right) \quad (12.44)$$

$$m_2 = \frac{\partial \Phi}{\partial \sigma_{eq}} = \frac{2\sigma_{eq}}{\sigma_M^2} \quad (12.45)$$

$$m_3 = \frac{\partial \Phi}{\partial H_1} = -\frac{\sigma'_M}{\sigma_M^2} \left[2\frac{\sigma_{eq}^2}{\sigma_M} + 3q_2 D^* \sigma_m \sinh \left(\frac{3q_2 \sigma_m}{2\sigma_M} \right) \right] \quad (12.46)$$

$$m_4 = \frac{\partial \Phi}{\partial H_2} = 0 \quad (12.47)$$

$$m_5 = \frac{\partial \Phi}{\partial H_3} = 2\frac{\partial D^*}{\partial D} \left[\cosh \left(\frac{3q_2 \sigma_m}{2\sigma_M} \right) - D^* \right] \quad (12.48)$$

$$m_6 = \frac{\partial^2 \Phi}{\partial \sigma_m \partial H_1} = -\frac{3q_2 D^* \sigma'_M}{\sigma_M^2} \left[\sinh \left(\frac{3q_2 \sigma_m}{2\sigma_M} \right) + \frac{3q_2 \sigma_m}{2\sigma_M} \cosh \left(\frac{3q_2 \sigma_m}{2\sigma_M} \right) \right] \quad (12.49)$$

$$m_7 = \frac{\partial^2 \Phi}{\partial \sigma_m \partial H_2} = 0 \quad (12.50)$$

$$m_8 = \frac{\partial^2 \Phi}{\partial \sigma_m \partial H_3} = \frac{3q_2}{\sigma_M} \frac{\partial D^*}{\partial D} \sinh \left(\frac{3q_2 \sigma_m}{2\sigma_M} \right) \quad (12.51)$$

$$m_9 = \frac{\partial^2 \Phi}{\partial \sigma_{eq} \partial H_1} = \frac{-4\sigma_{eq} \sigma'_M}{\sigma_M^3} \quad (12.52)$$

$$m_{10} = \frac{\partial^2 \Phi}{\partial \sigma_{eq} \partial H_2} = 0 \quad (12.53)$$

$$m_{11} = \frac{\partial^2 \Phi}{\partial \sigma_{eq} \partial H_3} = 0 \quad (12.54)$$

$$m_{12} = \frac{\partial^2 \Phi}{\partial \sigma_m^2} = \frac{9q_2^2 D^*}{2\sigma_M^2} \cosh \left(\frac{3q_2 \sigma_m}{2\sigma_M} \right) \quad (12.55)$$

$$m_{13} = \frac{\partial^2 \Phi}{\partial \sigma_{eq}^2} = \frac{2}{\sigma_M^2} \quad (12.56)$$

$$m_{14} = \frac{\partial^2 \Phi}{\partial \sigma_m \partial \sigma_{eq}} = 0 \quad (12.57)$$

where σ'_M is the tangent modulus of the matrix material, i.e. $\sigma'_M = \partial \sigma_M / \partial \varepsilon^p$.

The partial derivatives of the internal variables are calculated using Eqs. (12.58) and (12.59).

$$\left\{ \begin{array}{ccc} 1 - \Delta t \frac{\partial h_1}{\partial H_1} & -\Delta t \frac{\partial h_1}{\partial H_2} & -\Delta t \frac{\partial h_1}{\partial H_3} \\ -\Delta t \frac{\partial h_2}{\partial H_1} & 1 - \Delta t \frac{\partial h_2}{\partial H_2} & -\Delta t \frac{\partial h_2}{\partial H_3} \\ -\Delta t \frac{\partial h_3}{\partial H_1} & -\Delta t \frac{\partial h_3}{\partial H_2} & 1 - \Delta t \frac{\partial h_3}{\partial H_3} \end{array} \right\} \left\{ \begin{array}{c} \frac{\partial H_1}{\partial \varepsilon_m} \\ \frac{\partial H_2}{\partial \varepsilon_m} \\ \frac{\partial H_3}{\partial \varepsilon_m} \end{array} \right\} = \Delta t \left\{ \begin{array}{c} \frac{\partial h_1}{\partial \varepsilon_m} - \Delta t K \frac{\partial h_1}{\partial \sigma_m} \\ \frac{\partial h_2}{\partial \varepsilon_m} - \Delta t K \frac{\partial h_2}{\partial \sigma_m} \\ \frac{\partial h_3}{\partial \varepsilon_m} - \Delta t K \frac{\partial h_3}{\partial \sigma_m} \end{array} \right\} \quad (12.58)$$

$$\begin{pmatrix} 1 - \Delta t \frac{\partial h_1}{\partial H_1} & -\Delta t \frac{\partial h_1}{\partial H_2} & -\Delta t \frac{\partial h_1}{\partial H_3} \\ -\Delta t \frac{\partial h_2}{\partial H_1} & 1 - \Delta t \frac{\partial h_2}{\partial H_2} & -\Delta t \frac{\partial h_2}{\partial H_3} \\ -\Delta t \frac{\partial h_3}{\partial H_1} & -\Delta t \frac{\partial h_3}{\partial H_2} & 1 - \Delta t \frac{\partial h_3}{\partial H_3} \end{pmatrix} \begin{pmatrix} \frac{\partial H_1}{\partial \dot{\varepsilon}_{\text{eq}}} \\ \frac{\partial H_2}{\partial \dot{\varepsilon}_{\text{eq}}} \\ \frac{\partial H_3}{\partial \dot{\varepsilon}_{\text{eq}}} \end{pmatrix} = \Delta t \begin{pmatrix} \frac{\partial h_1}{\partial \dot{\varepsilon}_{\text{eq}}} - 3G\Delta t \frac{\partial h_1}{\partial \sigma_{\text{eq}}} \\ \frac{\partial h_2}{\partial \dot{\varepsilon}_{\text{eq}}} - 3G\Delta t \frac{\partial h_2}{\partial \sigma_{\text{eq}}} \\ \frac{\partial h_3}{\partial \dot{\varepsilon}_{\text{eq}}} - 3G\Delta t \frac{\partial h_3}{\partial \sigma_{\text{eq}}} \end{pmatrix} \quad (12.59)$$

$$z_1 = \frac{\partial h_1}{\partial H_1} = -\frac{h_1}{H_1} \sigma'_M \quad (12.60)$$

$$z_2 = \frac{\partial h_2}{\partial H_1} = A_n \left[\frac{\partial h_1}{\partial H_1} - \frac{(\varepsilon^p - \varepsilon_n) h_1}{s_n^2} \right] \quad (12.61)$$

$$z_3 = \frac{\partial h_3}{\partial H_1} = \frac{\partial h_2}{\partial H_1} + q_3 f^{q_4} g(\theta) \left[h_1 + H_1 \frac{\partial h_1}{\partial H_1} \right] \quad (12.62)$$

$$z_4 = \frac{\partial h_1}{\partial H_2} = \frac{h_1}{(1-f)} \quad (12.63)$$

$$z_5 = \frac{\partial h_2}{\partial H_2} = -\dot{\varepsilon}_m + A_n \frac{\partial h_1}{\partial H_2} \quad (12.64)$$

$$z_6 = \frac{\partial h_3}{\partial H_2} = \frac{\partial h_2}{\partial H_2} + q_3 q_4 f^{q_4-1} g(\theta) H_1 h_1 \quad (12.65)$$

$$z_7 = \frac{\partial h_1}{\partial H_3} = 0 \quad (12.66)$$

$$z_8 = \frac{\partial h_2}{\partial H_3} = 0 \quad (12.67)$$

$$z_9 = \frac{\partial h_3}{\partial H_3} = 0 \quad (12.68)$$

$$z_{10} = \frac{\partial h_2}{\partial \sigma_m} = \frac{\dot{\varepsilon}_m}{(1-f)\sigma_M} \quad (12.69)$$

$$z_{11} = \frac{\partial h_2}{\partial \sigma_m} = A_n \frac{\partial h_1}{\partial \sigma_m} \quad (12.70)$$

$$z_{12} = \frac{\partial h_3}{\partial \sigma_m} = 0 \quad (12.71)$$

$$z_{13} = \frac{\partial h_1}{\partial \sigma_{eq}} = \frac{\dot{\varepsilon}_{eq}}{(1-f)\sigma_M} \quad (12.72)$$

$$z_{14} = \frac{\partial h_2}{\partial \sigma_{eq}} = A_n \frac{\partial h_1}{\partial \sigma_{eq}} \quad (12.73)$$

$$z_{15} = \frac{\partial h_3}{\partial \sigma_{eq}} = 0 \quad (12.74)$$

$$z_{16} = \frac{\partial h_1}{\partial \dot{\varepsilon}_m} = \frac{\sigma_m}{(1-f)\sigma_M} \quad (12.75)$$

$$z_{17} = \frac{\partial h_2}{\partial \dot{\varepsilon}_m} = (1-f) + A_n \frac{\partial h_1}{\partial \dot{\varepsilon}_m} \quad (12.76)$$

$$z_{18} = \frac{\partial h_3}{\partial \dot{\varepsilon}_m} = 0 \quad (12.77)$$

$$z_{19} = \frac{\partial h_1}{\partial \dot{\varepsilon}_{eq}} = \frac{\sigma_{eq}}{(1-f)\sigma_M} \quad (12.78)$$

$$z_{20} = \frac{\partial h_2}{\partial \dot{\varepsilon}_{eq}} = A_n \frac{\partial h_1}{\partial \dot{\varepsilon}_{eq}} \quad (12.79)$$

$$z_{21} = \frac{\partial h_3}{\partial \dot{\varepsilon}_{eq}} = 0 \quad (12.80)$$

In the matrix form and using the above definition of m_i and z_i ,

$$\begin{pmatrix} 1 - \Delta tz_1 & -\Delta tz_4 & -\Delta tz_7 \\ -\Delta tz_2 & 1 - \Delta tz_5 & -\Delta tz_8 \\ -\Delta tz_3 & -\Delta tz_6 & 1 - \Delta tz_9 \end{pmatrix} \begin{pmatrix} \frac{\partial H_1}{\partial \dot{\epsilon}_m} \\ \frac{\partial H_2}{\partial \dot{\epsilon}_m} \\ \frac{\partial H_3}{\partial \dot{\epsilon}_m} \end{pmatrix} = \Delta t \begin{pmatrix} z_{16} - \Delta t K z_{10} \\ z_{17} - \Delta t K z_{11} \\ z_{18} - \Delta t K z_{12} \end{pmatrix} \quad (12.81)$$

$$\begin{pmatrix} 1 - \Delta tz_1 & -\Delta tz_4 & -\Delta tz_7 \\ -\Delta tz_2 & 1 - \Delta tz_5 & -\Delta tz_8 \\ -\Delta tz_3 & -\Delta tz_6 & 1 - \Delta tz_9 \end{pmatrix} \begin{pmatrix} \frac{\partial H_1}{\partial \dot{\epsilon}_{eq}} \\ \frac{\partial H_2}{\partial \dot{\epsilon}_{eq}} \\ \frac{\partial H_3}{\partial \dot{\epsilon}_{eq}} \end{pmatrix} = \Delta t \begin{pmatrix} z_{19} - \Delta t K z_{13} \\ z_{20} - \Delta t K z_{14} \\ z_{21} - \Delta t K z_{15} \end{pmatrix} \quad (12.82)$$

Substituting the zeros in z_i , and one gets

$$\begin{pmatrix} 1 - \Delta tz_1 & -\Delta tz_4 \\ -\Delta tz_2 & 1 - \Delta tz_5 \end{pmatrix} \begin{pmatrix} \frac{\partial H_1}{\partial \dot{\epsilon}_m} \\ \frac{\partial H_2}{\partial \dot{\epsilon}_m} \end{pmatrix} = \Delta t \begin{pmatrix} z_{16} - \Delta t K z_{10} \\ z_{17} - \Delta t K z_{11} \end{pmatrix} \quad (12.83)$$

$$\frac{\partial H_3}{\partial \dot{\epsilon}_m} = \Delta t \left(z_3 \frac{\partial H_1}{\partial \dot{\epsilon}_m} + z_6 \frac{\partial H_2}{\partial \dot{\epsilon}_m} \right) \quad (12.84)$$

and

$$\begin{pmatrix} 1 - \Delta tz_1 & -\Delta tz_4 \\ -\Delta tz_2 & 1 - \Delta tz_5 \end{pmatrix} \begin{pmatrix} \frac{\partial H_1}{\partial \dot{\epsilon}_{eq}} \\ \frac{\partial H_2}{\partial \dot{\epsilon}_{eq}} \end{pmatrix} = \Delta t \begin{pmatrix} z_{19} - \Delta t K z_{13} \\ z_{20} - \Delta t K z_{14} \end{pmatrix} \quad (12.85)$$

$$\frac{\partial H_3}{\partial \dot{\epsilon}_{eq}} = \Delta t \left(z_3 \frac{\partial H_1}{\partial \dot{\epsilon}_{eq}} + z_6 \frac{\partial H_2}{\partial \dot{\epsilon}_{eq}} \right) \quad (12.86)$$

Chapter 13

Conclusions and Future Research

13.1 Conclusions on the damage plasticity theory

In the present thesis, a new damage plasticity model is developed based on a “*cylindrical decomposition*”. The theoretical background of the cylindrical decomposition is put forward to incorporate the pressure sensitivity and the Lode angle dependence of ductile fracture. A nonlinear damage accumulation rule taking accounts of the acceleration of damaging process along plastic deformation path is adopted such that the damaging rate can be obtained from the current stress and strain state. In addition to the damage accumulation, a weakening function associated with the damaging process characterizes the material deterioration.

This damage plasticity model is based on extensive experimental observations documented in the past century. An combined experimental and numerical program is further carried out to access and verify the assumptions of the model. Aluminum alloy 2024-T351 is used to study the material parameters. Experiments include un-notched and notched tensile round bars, doubly-grooved flat plates under tension, compression of cylinders and three point bending of rectangular bars were performed.

The complete elasto-plastic constitutive model and the numerical integration scheme of the damage plasticity model is also presented. An Euler backward procedure on the plasticity evolution and an Euler forward procedure on the damage evolution are proposed. The procedure is integrated in to an explicit code as a user subroutine.

A series of simulations based on a set of four selected tests were done to calibrate the material

constants. The initial material constants were obtained directly from experimental data and a “*trial-and-error*” procedure is then followed to fine tune the material parameters. The matrix stress strain curve is determined from curve fitting of in the range of low plastic damage. The obtained fracture characterizing material constants are then used to calculate the fracture pattern of the upsetting tests, three point bending tests and compact tension tests. Good agreement is achieved in both fracture patterns and the load displacement curves.

An important finding is that the transition of the crack from a flat nature to a slant one is governed by the joint effect of the Lode angle dependence and the material weakening. These two factors entangled together in the formation of shear bands. The Lode angle dependence factor shows a faster damage accumulation speed in the shear bands and the deformation is future localizes within the shear bands due to material weakening effect.

13.2 Future research

Although success has been achieved using the proposed damage plasticity model to reconstruct and predict realistic fracture models and the load-displacement curves, improvements can be made in the following directions.

13.2.1 Lode angle dependence function

As pointed out in Chapter 2, the least studied area in the modeling of ductile fracture is the Lode angle dependence. It is often tacitly assumed that ductile fracture is independent of the Lode angle (or the third invariant of the deviatoric stresses). However, in the present thesis, we have shown that the ductile fracture is indeed depends on the Lode angle of the loading condition.

In the present model, we defined a new material parameter γ to characterize the difference in the ductility between $\chi = 0$ and $\chi = 0.5$. It is important progress in the ductile fracture modeling because we have shown that it is one of the most important driving force in the competition between and flat and a slant fracture mode in examples such as the crack propagation in compact tension specimens.

However, the experimental work in this direction is still scarce. Functional forms have been proposed in the present thesis. More detailed work is to be done to obtain the necessary parameters. An improvement in the experimental technique is essential in determining the Lode dependence

function.

13.2.2 Damage accumulation

We have separated different damage quantities for the purpose of characterize the evolution of damage. Fractional ductility is used as the “*damage*” and fractional stiffness is used as the weakening factor. There, of course, other micro mechanical phenomena associated with the damage accumulation, such as the widely used void volume fraction. However, the measurement of micro structure related parameters is difficult and is often described in a stochastic way. The proposed damage plasticity model uses a ductility and stiffness measurement, such that the damage evolution is considered on the macro scale.

In this regard, experiments have been performed and measurements are made typically using simple tension specimens. The damaging process is mingled with the pressure effects. It seems that an experimental technique that allow the material to deform under a constant pressure is of great interest to the mechanical community to further justify the proposed damage plasticity model and is also of great value to the ease of material constant calibration.

13.2.3 Damage coupling in the material strength

The last thing, which should be pointed out is the damage coupling to the material strength. It has been shown the importance of the introduction of a weakening effect to the material strength due to the accumulation of damage. Whether the pressure dependence of the weakening for ductile materials is essential in the modeling of ductile fracture is still debatable. In the present theory, we have shown that without this pressure dependence in the yield function, good results can be obtained. By neglecting this effect, the numerical integration scheme becomes much simpler. An iterative process has been reduced to a simple radial mapping method for materials obey associative flow rule.

In a phenomenological way, a power law weakening function is proposed and a three parameter power law function is adopted to obtain reasonably good results of the matrix stress strain curves. Because of the relatively short global displacement in the final range of deformation before fracture and the scattering of experimental data, difficulties in calibrate the material weakening related curves is hard to overcome. The phenomenological nature of the weakening function may still be

used until new experimental technology appears.

Appendix A

Appendix

A: Bridgman Test Results

The complete list of data used from Bridgman's test results are shown in Table A.1.

Table A.1: Collected results of the Bridgman's Tests (after [2], p.50-59.)

Material	Confining Pressure (MPa)	Final Flow Stress (MPa)	Strain at Fracture	Remarks
1-0	275.800	1130.78	1.35	
	0.100	1006.67	0.91	
	965.300	1958.18	3.01	
2-0	0.100	1310.05	0.77	
	806.715	1627.22	2.45	
	372.330	1406.58	1.34	
2-1	1296.260	2344.3	3.55	
	0.100	1144.57	0.86	
	365.435	1406.58	1.35	
2-2	1158.360	1523.8	3.02	
	599.865	1703.07	1.84	
	0.100	1034.25	0.73	
2-3	1385.895	2165.03	3.23	
	399.910	1172.15	1.24	
	0.100	910.14	0.5	
2-5	324.065	1054.93	0.86	
	868.770	1613.43	2.1	
	0.100	2247.77	0.84	
2-6	282.695	2364.99	1.11	
	682.605	2875.22	1.58	x ^a
	475.755	2413.25	1.19	
	1772.015	3461.29	2.35	
2-6	0.100	2530.47	0.68	
	289.590	2516.68	1.01	

Continued on next page

^aThe 'x' mark indicates the data is not used in the curve fitting.

Table A.1 – continued from previous page

Material	Confining Pressure (MPa)	Final Flow Stress (MPa)	Strain at Fracture	Remarks
	730.870	2647.68	1.58	
	1020.460	3468.18	2.05	
	1882.335	3516.45	2.75	x
2-7	0.100	1544.48	0.95	
	293.038	1730.65	1.26	
	875.665	2330.51	1.94	
	1523.795	2647.68	2.56	x
3-0	0.100	1241.1	0.46	
	661.920	1703.07	1.39	x
	2695.945	3840.51	4.29	
	179.270	1254.89	0.61	
4-0	0.100	1130.78	0.23	
	1379.000	2247.77	2.2	
	772.240	1661.69	1.03	
	2723.525	2585.63	3.76	x
	193.060	1330.73	0.4	
4-1	0.100	1316.94	0.33	
	744.660	1792.7	1.14	
	1682.380	2247.77	3.01	
4-2	0.100	985.985	0.33	
	1275.575	1792.7	1.75	
	682.605	1268.68	0.88	
	179.270	1096.31	0.44	
	1861.650	1744.43	2.77	
4-3	0.100	965.3	0.12	
	992.880	1399.68	0.79	
	372.330	1041.15	0.25	x
	2151.240	2895.9	3.08	
4-5	0.100	2171.93	0.13	
	275.800	2192.61	0.23	
	399.910	2289.14	0.27	
	2192.610	372.33	2.27	x
	1778.910	3171.7	1.77	
	1372.105	2861.43	1.19	
5-0-Longitudinal	0.100	1268.68	1.12	
	572.285	1468.64	1.75	
	2054.710	985.985	3.65	x
	1565.165	2102.97	2.98	
7-0-rolling	0.100	1379	1.1	
	792.925	1827.18	2.22	
	1068.725	2123.66	2.71	
9-2	0.100	1820.28	0.88	
	0.100	1778.91	0.89	
	772.240	2096.08	1.63	
	1434.160	2971.74	2.57	
	2640.785	3840.51	3.73	x
	0.100	2027.13	0.85	
	896.350	2309.82	1.54	
	1192.835	3033.8	2.11	
	413.700	2185.72	1.28	
	1854.755	4054.26	2.98	
	1882.335	3495.76	2.76	

Continued on next page

Table A.1 – continued from previous page

Material	Confining Pressure (MPa)	Final Flow Stress (MPa)	Strain at Fracture	Remarks
9-3	0.100	1268.68	0.92	
	1282.470	1744.43	2.78	
	999.775	2468.41	2.37	x
	234.430	1447.95	1.1	
	0.100	1241.1	0.81	
9-4	0.100	1123.89	0.89	
	124.110	861.875	1.13	
	799.820	1654.8	2.14	
	0.100	1123.89	0.9	
	510.230	1241.1	1.56	
9-6	1254.890	2034.03	2.83	
	0.100	1337.63	0.98	
	434.385	1709.96	1.39	
10-1	1096.305	1958.18	2.1	
	565.390	2344.3	0.22	
	1861.650	3599.19	0.98	
16-0	2302.930	3571.61	1.43	
	1282.470	1820.28	3.52	
	1806.490	2254.67	4.38	
17-0	655.025	1620.33	2.57	
	751.555	2502.89	2.09	
	1551.375	2723.53	2.29	
18-0	2413.250	3806.04	2.76	
	717.080	2413.25	2.51	
	1558.270	3026.91	2.69	
19-1	2385.670	510.23	3	
	0.100	2158.14	0.59	
	1006.670	2868.32	1.3	
	2585.625	6826.05	2.6	x
	2330.510	3764.67	2.37	x
19-2	1627.220	3206.18	1.88	
	0.100	2482.2	0.49	
	792.925	2785.58	0.91	
	1654.800	3737.09	1.36	
19-3	2475.305	3413.03	1.64	x
	0.100	2626.99	0.25	
	2344.300	3640.56	1.45	
	0.100	2654.57	0.14	
	2502.885	4068.05	1.37	
	786.030	2889.01	0.41	
	1551.375	3730.2	0.79	

Continued on next page

Table A.1 – concluded from previous page

Material	Confining Pressure (MPa)	Final Flow Stress (MPa)	Strain at Fracture	Remarks
19-4	0.100	2826.95	0.07	
	2758.000	4116.31	0.98	x
	772.240	3399.24	0.32	
	1647.905	3868.09	0.68	

Bibliography

- [1] I. Barsoum and J. Faleskog. Rupture mechanisms in combined tension and shearexperiments. *International Journal of Solids and Structures*, 44(6):1768–1786, 2007.
- [2] P. W. Bridgman. *Studies in large plastic flow and fracture*. McGraw-Hill Inc., 1952.
- [3] G.R. Johnson and W.H. Cook. Fracture characteristics of three metals subjected to various strains, strain rates, temperatures and pressures. *Engineering Fracture Mechanics*, 21(1):31–48, 1985.
- [4] T. Børvik, O. S. Hopperstad, T. Berstad, and M. Langseth. A computational model of viscoplasticity and ductile damage for impact and penetration. *European journal of mechanics. A, Solids*, 20:685–712, 2001.
- [5] W. von Lode. Versuche über den einfluß der mittleren hauptspannung auf die fließgrenze. *Zeitschrift für angewandte mathematik und mechanik*, 5(2):142–144, 1925.
- [6] J. P. Bardet. Lode dependences for isotropic pressure-sensitive elastoplastic materials. *Transactions of the ASME*, 57:498–506, 1990.
- [7] Stephen Timoshenko. *History of strength of materials*. McGraw-Hill, New York, 1953.
- [8] H.P. Rossmannith. *Fracture research in retrospect - an anniversary volume in honour of George R. Irwin's 90th birthday*, chapter The struggle for recognition of engineering fracture mechanics, pages 37–93. A.A.Balkema Publishers, Rotterdam, 1997.
- [9] M.T. Huber. Specific deformation work as a measure of material damage [in polish],. *Czasopismo Techniczne, Lwów*; reedited: *M.T. Huber. Pisma, Warszawa 1957, PWN*, 2:1–20, 1904.

- [10] J. Lemaître. A continuous damage mechanics model for ductile fracture. *Journal of Engineering Materials and Technology - Trans. of the ASME*, 107:83–89, 1985.
- [11] J.L. Chaboche. Continuum damage mechanics: Part I - general concepts. *Journal of Applied Mechanics - Trans. of the ASME*, 55:59–64, 1988.
- [12] S. Murakami. Mechanical modeling of material damage. *Journal of Applied Mechanics - Trans. of the ASME*, 55:280–286, 1988.
- [13] J. Lemaître. How to use damage mechanics. *Nuclear Engineering and Design*, 80:233–245, 1984.
- [14] J. Lemaître. *A course on damage mechanics*. Springer, Berlin; New York, 1992.
- [15] L.M. Kachanov. On the creep fracture time. *Izv. Akad. Nauk USSR Otd. Tekh.*, 8:26–31, 1958. (in Russian).
- [16] A. L. Gurson. Continuum theory of ductile rupture by void nucleation and growth: Part I. Yield criteria and flow rules for porous ductile media. *Journal of Engineering Materials and Technology - Trans. of the ASME*, 99:2–15, 1977.
- [17] F. A. McClintock. A criterion for ductile fracture by growth of holes. *Trans. ASME. Journal of Applied Mechanics*, 35:363–371, 1968.
- [18] M. G. Cockcroft and D. J. Latham. Ductility and the workability of metals. *Journal of the Institute of Metals*, 96:33–39, 1968.
- [19] J. R. Rice and D. M. Tracey. On the ductile enlargement of voids in triaxial stress fields. *Journal of the Mechanics and Physics of Solids*, 17:201–217, 1969.
- [20] P. Brozzo, B. Deluca, and R. Rendina. A new method for the prediction of formability in metal sheet, sheet metal forming and formability. In *Proceedings of the 7th Biennial Conference of the International Deep Drawing Research Group*, Amsterdam, 1972.
- [21] D. M. Norris, J. E. Reaugh, B. Moran, and D. F. Quinones. A plastic-strain mean-stress criterion for ductile fracture. *Journal of Engineering Materials*, 100:279–286, 1978.

- [22] M.L. Wilkins, R.D. Streit, and J.E. Reaugh. Cumulative-strain-damage model of ductile fracture: Simulation and prediction of engineering fracture tests. Technical Report UCRL-53058, Lawrence Livermore National Laboratory, October 1980.
- [23] G. Le Roy, J. Embury, G. Edwards, and M. F. Ashby. A model of ductile fracture based on the nucleation and growth of voids. *Acta Metallurgica*, 29:1509–1522, 1981.
- [24] A. Needleman and V. Tvergaard. An analysis of ductile rupture in notched bars. *Journal of Mechanics and Physics of Solids*, 32:461–490, 1984.
- [25] R. Chaouadi, P. D. Meester, and W. Vandermeulen. Damage work as ductile fracture criterion. *International Journal of Fracture*, 66(2), 1994.
- [26] Y. Bao and T. Wierzbicki. On fracture locus in the equivalent strain and stress triaxiality space. *International Journal of Mechanical Sciences*, 46:81–98, 2004.
- [27] H. Hooputra, H. Gese, H. Dell, and H. Werner. A comprehensive failure model for crashworthiness simulation of aluminum extrusions. *International Journal of Crashworthiness*, 9(5):449–463, 2004.
- [28] G.R. Johnson, J.M. Hoegfeldt, U.S. Lindholm, and A. Nagy. Response of various metals to large torsional strains over a large range of strain rates - part 2: Less ductile metals. *Journal of Engineering Materials and Technology, Transaction of the ASME*, 105:48–5, 1983.
- [29] H. Ll. D. Pugh. Cold deformation of metals part 2 - cold extrusion. *Metal Treatment and Drop Forging*, pages 231–236, June 1960.
- [30] T. E. Davidson, J. C. Uy, and A. P. Lee. The tensile fracture characteristics of metals under hydrostatic pressures to 23 kilobars. *Acta Metallurgica*, 14:937–948, 1966.
- [31] I. E. French, P. F. Weinrich, and C. W. Weaver. Tensile fracture of free machining brass as a function of hydrostatic pressure. *Acta Metallurgica*, 21:1045–1049, 1973.
- [32] I. E. French and P. F. Weinrich. The effect of hydrostatic pressure on the tensile fracture of α -brass. *Acta Metallurgica*, 21:1533–1537, 1973.

- [33] W. A. Spitzig. Effect of hydrostatic pressure on deformation, damage evolution, and fracture of iron with various initial porosities. *Acta Metall. Mater.*, 38(8):1445–1453, 1990.
- [34] A. S. Kao, H. A. Kuhn, O. Richmond, and W. A. Spitzig. Tensile fracture and fractographic analysis of 1045 spheroidized steel under hydrostatic pressure. *Journal of Materials Research*, 5(1):83–91, 1990.
- [35] J. J. Lewandowski and P. Lowhaphandu. Effect of hydrostatic pressure on mechanical behavior and deformation processing of materials. *International Materials Reviews*, 43(4):145–187, 1998.
- [36] D.M. Goto, D.A. Koss, and V. Jablakov. The influence of tensile stress states on the failure of HY-100 steel. *Metallurgical and Materials Transactions A*, 30A:2835–2842, 1999.
- [37] K. Mogi. Effect of the intermediate principal stress on rock failure. *Journal of Geophysical Research*, 72(20):5117–5131, 1967.
- [38] K. Mogi. Effect of the triaxial stress system on the failure of dolomite and limestone. *Tectonophysics*, 11:111–127, 1971.
- [39] K. Mogi. Effect of the triaxial stress system on fracture and flow of rocks. *Physics of the Earth and Planetary Interiors*, 5:318–324, 1972.
- [40] D. P. Clausing. Effect of plastic strain state on ductility and toughness. *International Journal of Fracture Mechanics*, 6(1):71–85, 1970.
- [41] F. A. McClintock. *Plasticity aspects of fracture*, volume III of *Fracture An Advanced Treatise*, chapter 2, pages 47–307. Academic Press, New York and London, 1971.
- [42] G. R. Halford and JoDean Morrow. *On low-cycle fatigue in torsion*, volume 62 of *American Society for Testing and Materials proceedings*, pages 695–707. American Society for Testing and Materials, 1962.
- [43] J. E. Neimark. The fully plastic, plane-strain tension of a notched bar. *Journal of Applied Mechanics - Trans. of the ASME*, 35(1):111–116, March 1968.

- [44] Y. Li, K.T. Ramesha, and E.S.C. Chin. The mechanical response of an A359/SiCp MMC and the A359 aluminum matrix to dynamic shearing deformations. *Materials Science and Engineering A*, 382:162C170, 2004.
- [45] T. Bøvik, O.S. Hopperstad, T. Berstad, and M. Langseth. A computational model of viscoplasticity and ductile damage for impact and penetration. *European Journal of Mechanics A/Solids*, 20:685–712, 2001.
- [46] G.R. Johnson. Materials characterization for computations involving severe dynamic loading. In *Proceedings of Army Symposium on Solid Mechanics (7th)*, Watertown, Massachusetts, 1980.
- [47] X. Teng and T. Wierzbicki. Numerical study on crack propagation in high velocity perforation. *Computers & Structures*, 83(12-13):989–1004, May 2005.
- [48] V. Tvergaard. Influence of voids on shear band instabilities under plane strain conditions. *International Journal of Fracture*, 17:389–407, 1981.
- [49] V. Tvergaard and A. Needleman. Analysis of the cup-cone fracture in a round tensile bar. *Acta Metallurgica*, 32(1):157–169, 1984.
- [50] C.A. Berg. The motion of cracks in plane viscous deformation. In *The fourth U.S. National Congress of Applied Mechanics*, volume 2, Berkeley, CA, 1962.
- [51] D. Chae and D. A. Koss. Damage accumulation and failure of hsla-100 steel. *Materials Science and Engineering A*, 366(2):299–309, February 2004.
- [52] V. Tvergaard. Influence of void nucleation on ductile shear fracture at a free surface. *Journal of the Mechanics and Physics of Solids*, 30(6):399–425, 1982.
- [53] S.H. Goods and L.M. Brown. The nucleation of cavities by plastic deformation. *Acta Metallurgical*, 27:1–15, 1979.
- [54] A.L. Gurson. Porous rigid-plastic materials containing rigid inclusions - yield function, plastic potential, and void nucleation. In D.M.R. Taplin, editor, *Advances in Research on the Strength and Fracture of Materials*, volume 2A of *Fourth International Conference on Fracture*, pages 357–364, Waterloo, Canada, June 19-24 1977.

- [55] A.S. Argon, J. Im, and R. Safoglu. Cavity formation from inclusions in ductile fracture. *Metallurgical Transactions 6A*, pages 825–837, 1975.
- [56] J. Gurland. Observations on the fracture of cementite particles in a spheroidized 1.05% C steel deformed at room temperature. *Acta Metallurgica*, 20:735–741, 1972.
- [57] A. Needleman and J.R. Rice. Limits to ductility set by plastic flow localization. In N.P. Koistinen and N.M. Wang, editors, *Mechanics of Sheet Metal Forming*, pages 237–265. Plenum Press, New York, 1978.
- [58] C.C. Chu and A. Needleman. Void nucleation effects in biaxially stretched sheets. *Journal of Engineering Materials and Technology*, 102:249–256, 1980.
- [59] Y.N. Rabotnov. On the equations of state for creep. In *Progress in Applied Mechanics - the Prager Anniversary Volume*, pages 307–315. MacMillan, New York, 1963.
- [60] L.M. Kachanov. *Introduction to Continuum Damage Mechanics*. Martinus Nijhoff Publishers, Dordrecht, 1986.
- [61] J. Lemaître and J.L. Chaboche. Aspect Phénoménologique de la Rupture par Endommagement. *Journal de Mécanique Appliquée*, 2:317–365, 1978.
- [62] N. Bonora and G.M. Newaz. Low cycle fatigue life estimation for ductile metals using a non-linear continuum damage mechanics model. *International Journal of Solids and Structures*, 35(16):1881–1894, 1998.
- [63] P. W. Bridgman. Effect of hydrostatic pressure on plastic plasticity and strength. *Research (London)*, 2:550–555, 1949.
- [64] J. Lemaitre and J. Dufailly. Damage measurements. *Engineering Fracture Mechanics*, 28(5-6):643–661, 1987.
- [65] H.L.D. Pugh. *Mechanical behavior of materials under pressure*, chapter 10 The application of hydrostatic pressure to the forming of metals, pages 522–590. Elsevier Publishing Co. Ltd., Amsterdam, 1970.

- [66] H. Ll. D. Pugh, G. Hodgson, and D. A. Gunn. Tensile strain measurement under high hydrostatic pressure using an optical method. *Journal of Scientific Instruments*, 40:221–224, 1963.
- [67] L.C. Towle and R.E. Riecker. Shear strength of grossly deformed solids. *Science*, 163(3862):41–47, 1969.
- [68] W. Szczepiński, editor. *Experimental methods in mechanics of solids*. PWN-Polish Scientific Publishers and Elsevier, 1990.
- [69] J. W. Hancock and A. C. Mackenzie. On the mechanisms of ductile failure in high-strength steels subjected to multi-axial stress-states. *Journal of the Mechanics and Physics of Solids*, 24(2-3):147–160, 1976.
- [70] L. Devillers-Guerville, J. Besson, and A. Pineau. Notch fracture toughness of a cast duplex stainless steel: modelling of experimental scatter and size effect. *Nuclear Engineering and Design*, 168:211–225, 1997.
- [71] H. Ll. D. Pugh. *The mechanical properties and deformation characteristics of metals and alloys under pressure*, page 68. ASTM Special Publication No.374. ASTM International Conference on Materials, Philadelphia, 1964, 1965.
- [72] H. Ll. D. Pugh. Cold deformation of metals part i - cold forging. *Metal Treatment and Drop Forging*, pages 189–195, May 1960.
- [73] H. Ll. D. Pugh. Metalworking using fluid pressure. *Annual Review of Materials Research*, pages 253–290, 1972.
- [74] A.F. Hayes and J.A. Yoblin. Advanced techniques for forging beryllium. In *The metallurgy of beryllium*. the Institute of Metals, 16-18 October 1961.
- [75] R.M. Cogan. Hydrodynamic forming. *Journal of Engineering for Industry*, 93(May):105–109, 1965.
- [76] A. Bobrowski, E.A. Stack, and A. Austen. Extrusion and drawing using high pressure hydraulics. In *American Society of Tool and Manufacturing Engineers conference, Paper No. SP65-33*, 1964.

- [77] S. Mepsted. Cold pressure welding. *Wire Industry*, 69(821):329–332, 2002.
- [78] B. Crossland. *Explosive welding of metals and its application*. Clarendon Press, Oxford, 1982.
- [79] S.J. Paprocki and E.S. Hodge. *Mechanical behavior of materials under pressure*, chapter 11 The compaction of powders by isostatic pressure, pages 591–637. Elsevier Publishing Co. Ltd., Amsterdam, 1970.
- [80] J. Greenspan. In F. Benesovsky, editor, *Metals for the space age*, Plansee Proceedings, pages 163–176, Reutte/Tyrol, 1964. Metallwerk Plansee AG.
- [81] J.W. Hancock and D.K. Brown. On the role of stress and strain state in ductile failure. *Journal of the Mechanics and Physics of Solids*, 31(1):1–24, 1983.
- [82] C. M. Adams Jr. Effective ductility in castings and weldments. In *Ductility*, chapter 6, pages 179–197. American Society for Metals, Metals Park, Ohio, 1967.
- [83] T. Pardoën, Y. Marchal, and F. Delannay. Thickness dependence of cracking resistance in thin aluminium plates. *Journal of the Mechanics and Physics of Solids*, 47:2093–2123, 1999.
- [84] J. W. Rudnicki and J. R. Rice. Conditions for the localization of deformation in pressure-sensitive dilatant materials. *Journal of Mechanics and Physics of Solids*, 23:371–394, 1975.
- [85] S. Stören and J. R. Rice. Localized necking in thin sheets. *Journal of the Mechanics and Physics of Solids*, 23:421–441, 1975.
- [86] R.C. Batra, X. Zhang, and T.W. Wright. Critical strain ranking of 12 materials in deformations involving adiabatic shear bands. *Journal of Applied Mechanics - Transactions of ASME*, 62:252–255, 1995.
- [87] T. Wierzbicki and L. Xue. On the effect of the third invariant of the stress deviator on ductile fracture. Technical Report 136, Impact and Crashworthiness Lab, MIT, March 2005.
- [88] J.C. Simo and T. Hughes. *Computational Inelasticity*. Springer-Verlag, New York, 1998.
- [89] Y. Bao. *Prediction of ductile crack formation in uncracked bodies*. PhD thesis, MIT, 2003.

- [90] J. Mescall, R. Papirno, and J. McClaughlin. Stress and deformation states associated with upset tests in materials. In R. Chait and R. Papirno, editors, *Compression Testing of Homogeneous Materials and Composites*, pages 7–23. American Society for Testing and Materials, 1983.
- [91] N. Loizou and R.B. Sims. The yield stress of pure lead in compression. *Journal of the Mechanics and Physics of Solids*, 1:234–243, 1953.
- [92] W. Johnson. The pressure for the cold extrusion of lubricated rod through square dies of moderate reduction at slow speeds. *Journal of the Institute of Metals*, 85:403–408, 1956.
- [93] S.B. Brown, K.H. Kim, and L. Anand. An internal variable constitutive model for hot working of metals. *International Journal of Plasticity*, 5:95–130, 1989.
- [94] D.M. Parks. private communication.
- [95] H.W. Swift. Plastic instability under plane stress. *Journal of the Mechanics and Physics of Solids*, 1(1):1–18, 1952.
- [96] L. Xue and T. Wierzbicki. Verification of a new fracture criterion using ls-dyna. In *The 9th International LS-DYNA User's Conference, Dearborn, MI, USA, June 4-6, 2006*.
- [97] T.L. Anderson. *Fracture Mechanics: Fundamentals and Applications*. CRC Press, Boca Raton, 1995.
- [98] D.S. Dawicke, M.A. Sutton, Jr. J.C. Newman, and C.A. Bigelow. Measurement and analysis of critical ctoa for an aluminum alloy sheet. Technical Report NASA-TM-109024, NASA Center for AeroSpace Information, 1993.
- [99] S. Mahmoud and K. Lease. The effect of specimen thickness on the experimental characterization of critical crack-tip-opening angle in 2024-t351 aluminum alloy. *Engineering Fracture Mechanics*, 70:443–456, 2003.
- [100] M.A. James and J.C. Newman Jr. The effect of crack tunneling on crack growth: experiments and CTOA analysis. *Engineering Fracture Mechanics*, 70:457–468, 2003.

- [101] D. S. Dugdale. Yielding of steel sheets containing slits. *Journal of the Mechanics and Physics of Solids*, 8(2):100–104, May 1960.
- [102] W.W. Gerberich. Plastic strains and energy density in cracked plates Part I - experimental technique and results. *Experimental Mechanics*, 4:335–344, 1964.
- [103] J.W. Hutchinson. Plastic stress and strain fields at a crack tip. *Journal of the Mechanics and Physics of Solids*, 16:337–347, 1968.
- [104] Craig L. Hom and Robert M. McMeeking. Large crack tip opening in thin elastic-plastic sheets. *International Journal of Fracture*, 45(2):103–122, September 1990.
- [105] D.S. Dawicke and M.A. Sutton. Crack-tip-opening angle measurements and crack tunneling under stable tearing in thin sheet 2024-t3 aluminum alloy. Technical Report NASA-CR-191523, NASA Center for AeroSpace Information, 1993.
- [106] L. Xia, C.F. Shih, and J.W. Hutchinson. A computational approach to ductile crack growth under large scale yielding condition. *Journal of the Mechanics and Physics of Solids*, 43(3):389–413, 1995.
- [107] Jr. J.C. Newman, D.S. Dawicke, and C.A. Bigelow. Finite-element analyses and fracture simulation in thin-sheet aluminum alloy. Technical Report NASA-TM-107662, NASA Center for AeroSpace Information, 1992.
- [108] D.S. Dawicke, J.C. Newman Jr., and C.A. Bigelow. Three-dimensional CTOA and constraint effects during stable tearing in a thin-steel material. *Fracture Mechanics: ASTM STP 1256*, 26:223–242, 1995.
- [109] S. Mahmoud and K. Lease. Two-dimensional and three-dimensional finite element analysis of critical crack-tip-opening angle in 2024-T351 aluminum alloy at four thickness. *Engineering Fracture Mechanics*, 71:1379–1391, 2004.
- [110] T. Pardoen, F. Hachez, B. Marchioni, P.H. Blyth, and A.G. Atkins. Mode I fracture of sheet metal. *Journal of the Mechanics and Physics of Solids*, 52:423–452, 2004.

- [111] V. Tvergaard and A. Needleman. Three dimensional microstructural effects on plane strain ductile crack growth. *International Journal of Solids and Structures*, 43(20):6165–6179, October 2006.
- [112] K.K. Mathur, A. Needleman, and V. Tvergaard. Three dimensional analysis of dynamic ductile crack growth in a thin plate. *Journal of the Mechanics and Physics of Solids*, 44(3):439–464, 1996.
- [113] J. Besson. Ductile tearing of metal sheets. Annual review meeting of the Impact and Crashworthiness Lab at MIT, October 2005.
- [114] M. Gologanu, J.-B. Leblond, G. Perrin, and J. Devaux. *Continuum Micromechanics. CISM Courses and Lectures no. 377.*, chapter Recent extensions of Gurson’s model for porous ductile metals, pages 61–130. Springer, New York, 1997.
- [115] A. Asserin-Lebert, J. Besson, and A.F. Gourgues. Fracture of 6056 aluminum sheet materials: effect of specimen thickness and hardening behavior on strain localization and toughness. *Materials Science and Engineering A*, 395:186–194, 2005.
- [116] A. Pineau and T. Pardoen. *Failure Mechanisms of Metals*. 2006.
- [117] M.A. Sutton, D.S. Dawicke, and J.C.Jr. Newman. Orientation effects on the measurement and analysis of critical CTOA in an aluminum alloy sheet. In W.G. Reuter, J.H. Underwood, and J.C. Newman, editors, *Fracture Mechanics: 26th volume*, volume ASTM STP 1256, pages 243–255. American Society for Testing and Materials, Philadelphia, 1995.
- [118] K.E. Puttick. Ductile fracture in metals. *Philosophical magazine*, 4:964–969, 1959.
- [119] H.C. Rogers. Tensile fracture of ductile metals. *Transactions of Metallurgical Society of AIME*, 218:498–506, 1960.
- [120] J. Besson, D. Steglich, and W. Brocks. Modeling of crack growth in round bars and plane strain specimens. *International Journal of Solids and Structures*, 38(46-47):8259–8284, 2001.
- [121] I. Scheider and W. Brocks. Simulation of cup-cone fracture using the cohesive model. *Engineering Fracture Mechanics*, 70(14):1943–1961, 2003.

- [122] J. Besson, D. Steglich, and W. Brocks. Modeling of plane strain ductile rupture. *International Journal of Plasticity*, 19:1517–1541, 2003.
- [123] R. Hill. On discontinuous plastic states, with special reference to localized necking in thin sheets. *Journal of the Mechanics and Physics of Solids*, 1:19–30, 1952.
- [124] F.A. McClintock and Z.M. Zheng. Ductile fracture in sheets under transverse strain gradients. *International Journal of Fracture*, 64:321–337, 1993.
- [125] J. Chattopadhyay, B.K. Dutta, and H.S. Kushwaha. Experimental and analytical study of three point bend specimen and throughwall circumferentially cracked straight pipe. *International Journal of Pressure Vessels and Piping*, 77:455–471, 2000.
- [126] M. Pedro, A. Areias, and T. Belytschko. Non-linear analysis of shells with arbitrary evolving cracks using XFEM. *International Journal for Numerical Methods in Engineering*, 62(3):384–415, 2005.
- [127] T. Belytschko and T. Black. Elastic crack growth in finite elements with minimal remeshing. *International Journal for Numerical Methods in Engineering*, 45(5):601–620, 1999.
- [128] P.W. Bridgman. Properties of matter under high pressure. *Mechanical Engineering*, 47:161–169, 1925.
- [129] A. Pandolfi, P. Krysl, and M. Ortiz. Finite element simulation of ring expansion and fragmentation: The capturing of length and time scales through cohesive models of fracture. *International Journal of Fracture*, 95(1-4):279 – 297, 1998.
- [130] T. Rabczuk and T. Belytschko. Adaptivity for structured meshfree particle methods in 2D and 3D. *International Journal for Numerical methods in Engineering*, 63:1559–1582, 2005.
- [131] T. Rabczuk and T. Belytschko. Cracking particles: a simplified meshfree method for arbitrary evolving cracks. *International Journal for Numerical Methods in Engineering*, 61(13):2316–2343, 2004.
- [132] F.A. McClintock, S.M. Kaplan, and C.A. Berg. Ductile fracture by hole growth in shear bands. *International Journal of Fracture Mechanics*, 2(4):614–627, 1966.

- [133] L. Xue. Damage accumulation and fracture initiation of uncracked ductile solids subjected to triaxial loading. *International Journal of Solids and Structures (accepted)*, 2006.
- [134] N. Aravas. On the numerical integration of a class of pressure-dependent plasticity models. *International Journal for Numerical Methods in Engineering*, 24:1395–1416, 1987.
- [135] B.C. Simonsen and S. Li. Mesh-free simulation of ductile fracture. *International Journal for Numerical Methods in Engineering*, 60:1425–1450, 2004.
- [136] Z.L. Zhang. *Nonlinear Fracture and Damage Mechanics*, chapter 8: A complete Gurson model, pages 223–248. WIT, Boston, 2001.
- [137] A.A. Benzerga. Micromechanics of coalescence in ductile fracture. *Journal of the Mechanics and Physics of Solids*, 50:1331–1362, 2002.
- [138] T. Pardoen and J.W. Hutchinson. An extended model for void growth and coalescence. *Journal of the Mechanics and Physics of Solids*, 48:2467–2512, 2000.
- [139] L.M. Brown and J.D. Embury. The initiation and growth of voids at second phase particles. In *Proceedings of the Third International Conference of the Strength of Metals and Alloys*, volume 1, pages 164–169, Cambridge, UK, 20-25, Aug., 1973.
- [140] T.B. Cox and J.R. Low. An investigation of the plastic fracture of AISI 4340 and 18 Ni-200 grade maraging steel. *Metallurgical Transactions*, 5:1457–1470, 1974.
- [141] I.G. Palmer and G.C. Smith. *Oxide dispersion strengthening*, page 253. Gordon and Breach, New York, 1968.
- [142] F.A. McClintock. Local criteria for ductile fracture. *International Journal of Fracture Mechanics*, 4(2):101–130, 1968.
- [143] V. Tvergaard. Material failure by void coalescence in localized shear bands. *International Journal of Solids and Structures*, 18(8):659–672, 1982.
- [144] A. Weck, D.S. Wilkinson, E. Maire, , and H. Toda. 3d visualization of ductile fracture. In *Advanced Engineering Materials, Proceedings of the Euromat Conference*, 2006.

- [145] K.S. Zhang, J.B. Bai, and D. François. Numerical analysis of the influence of the Lode parameter on void growth. *International Journal of Solids and Structures*, 38:5847–5856, 2001.
- [146] J. Kim, X. Gao, and T.S. Srivatsan. Modeling of void growth in ductile solids: effects of stress triaxiality and initial porosity. *Engineering Fracture Mechanics*, 71:379–400, 2004.
- [147] W. Brocks, D.Z. Sun, and A. Hömig. Verification of the transferability of micromechanical parameters by cell model calculations with visco-plastic materials. *International Journal of Plasticity*, 11(8):971–989, 1995.
- [148] N.A. Fleck, J.W. Hutchinson, and V. Tvergaard. Softening by void nucleation and growth in tension and shear. *Journal of the Mechanics and Physics of Solids*, 37(4):515–540, 1989.
- [149] K. Siruguet and J.B. Leblond. Effect of void locking by inclusions upon the plastic behavior of porous ductile solids - I: theoretical modeling and numerical study of void growth. *International Journal of Plasticity*, 20:255–268, 2004.
- [150] M.J. Worswick and P. Pelletier. Numerical simulation of ductile fracture during high strain rate deformation. *Eur. Phys. J. AP*, 4:257–267, 1998.
- [151] J.I. Bluhm and R.J. Morrissey. Fracture in a tensile specimen. In *Proceedings of First International Conference on Fracture*, volume 3, pages 1739–1780, Sendai, 1966. Japanese Society for Strength and Fracture of Materials.
- [152] V. Tvergaard. On localization in ductile materials containing spherical voids. *International Journal of Fracture*, 18(4):237–252, 1982.